DISTRIBUTION STATEMENT A
Approved for Public Release
Distribution Unlimited

Development of Thin Film PdMn High Resolution Thermometry for Measurement of the ^{4}He Superfluid Boundary Layer and Other Applications

BY

Raymond C. Nelson

B.S. United States Military Academy, 1983
M.S. University of Maryland, Physics, 1992

DISSERTATION

Submitted in Partial Fulfillment of the
Requirements for the Degree of

Doctor of Philosophy

Physics

The University of New Mexico
Albuquerque, New Mexico

July 2001

20010507 079

© Raymond C. Nelson, 2001

Dedication

This dissertation is dedicated to my family, Reva, Steven, and Peter, without whose patience and understanding it would not have been possible to complete the work.

Acknowledgements

This work is not entirely my own. It would not have been possible to even begin without the significant contributions of a number of important people and organizations.
First, The United States Army, which has provided me opportunities so generous as to be almost unimaginable. This is the third time I have been to school at the expense of the Army and I hope to continue to serve for many years so that I may repay my profound debt to this country and its citizens.

This work was performed under a NASA grant.

All the members of the DYNAMX group at the University of New Mexico have provided support and encouragement, especially T.D. McCarson, Dmitri Sergatskov, Alex Babkin, and Steve Boyd. Mary Jayne Adriaans, and Beverly Klemme, formerly of the group performed the early measurements on PdFe and PdMn which pointed the direction for this work.

The staff of the Physics and Astronomy Department were always as helpful as they could be, most notably Carl Allen, Paul Pickard, and John DeMoss, all thoroughly professional master machinists, who not only made many of the parts for the project, but patiently taught me the skills to make many of them myself.

Colin Green joined the project as an undergraduate assistant in the last six months of data collection. His assistance was of great value in completing the many measurements.

Finally, my advisor and the inspiration behind the project was Professor Robert Duncan, without whose guidance and advice no progress could have been made. He allowed me the freedom and the resources to learn, to design, and to explore.

Lieutenant Colonel Raymond C. Nelson
United States Army
University of New Mexico

Development of Thin Film PdMn High Resolution Thermometry for Measurement of the ^{4}He Superfluid Boundary Layer and Other Applications

BY

Raymond C. Nelson

B.S. United States Military Academy, 1983
M.S. University of Maryland, Physics, 1992
Ph.D. University of New Mexico, Physics, 2001

ABSTRACT OF DISSERTATION

Submitted in Partial Fulfillment of the
Requirements for the Degree of

Doctor of Philosophy
Physics

The University of New Mexico
Albuquerque, New Mexico

July 2001

Development Of Thin Film PdMn High Resolution Thermometry for Measurement Of The ^{4}He Superfluid Boundary Layer and Other Applications

by

Raymond C. Nelson

B.S. United States Military Academy, 1983
M.S, Physics, University of Maryland, 1992
Ph.D, University of New Mexico, 2001

Abstract

This thesis describes the development of PdMn thin films for high resolution thermometry. Measurements of the magnetic sensitivity of sputtered thin films of PdMn alloy suggest that the sputtering technique produces an ordered film with a manganese concentration slightly higher than the nominal value of the sputtering target. Sputtering from a 0.68% manganese target produced films with a concentration of approximately 0.90%, as judged by comparison with results from bulk PdMn sensitivity measurements. The thinnest films show significant domain scale noise below the Curie Temperature, T_c, while thicker films show reliable non-hysteretic behavior throughout the temperature range of interest. These films will serve as the thermometric element in a new class of bolometers for fundamental physics applications. They may also prove useful as a new class of conventional, low-temperature thermometers. Furthermore, measurements made at very low fields suggest that these films may be useful in a new class of biomagnetic measurements.

Table of Contents

List of Figures xi

List of Tables xvi

Chapter One -- Introduction 1

Liquid Helium 1

Superfluid Helium 1

Heat Transport in He II 2

Thermal Boundary Resistance 3

Two Fluid Counterflow 3

Length, Time and Temperature Scales: the Ψ Theory 5

Discovery of the Singular Kapitza Resistance 8

A Simple Model for the Singular Kapitza Resistance 8

Chapter Two – Experiment Design and Construction 24

Cryostat Selection and Modification 25

Cell and Suspension Design 26

Cell Actuation and Positioning 29

Instrumentation 30

Chapter Three -- PdMn Thin Film Thermometry 36

Initial Planning 36

Thermometer Design 37

Film Deposition 38

Sample Testing 43

Preparation of Superconducting Joints 44

Measurement Apparatus 45

Data Analysis 47

Results and Preliminary Conclusions 48

Chapter Four: Continued work on PdMn thin films 58

Experimental Objectives 58

Experiment Design and Preparation 58

Experimental Technique 59

Interpretation of Low Field Data 62

Hysteresis and Other Features 63

Chapter Five – Thinner Films 80

1 Micron Film – Sample Perpendicular to Field 80

Demagnetization 81

1 Micron Film – Sample Parallel to Field 82

Chapter Six – PdMn Screen Testing 93

Experiment Preparation 93

Initial Cooldown 94

Data Collection 95

Chapter Seven –Intentions for Further Study..... 104

Appendices..... 109

Appendix A: Tabular data for Superconducting Joint I-V curve..... 110

Appendix B: Tabular Data for Figures in Chapter Four 112

Appendix C: Tabular Data for Figures in Chapter Five..... 118

Appendix D: Tabular Data for Figures in Chapter Six 120

References..... 123

List of Figures

Figure 1: ^{4}He phase diagram, after London (1954) 16

Figure 2: Proportions of superfluid and normal fluid components, as a function of temperature. 17

Figure 3: Schematic representation of the effect of the Kaptiza resistance at the boundary between a copper end plate and an adjacent He II volume 18

Figure 4: Schematic representation of two fluid counterflow in He II 19

Figure 5: Schematic representation of the effect of incomplete counterflow in the boundary layer between the cell wall and the He II 20

Figure 6: Kapitza resistance vs. reduced temperature; DAS data[8] 21

Figure 7: RG calculations of Frank and Dohm[20] (solid and dotted lines) with the DAS Singular Kapitza Resistance data 22

Figure 8: Logarithm of reduced breakdown temperature vs. heat current, Q, based on Haussmann and Dohm $T_c(Q)$ theory (solid line) and $T_{DAS}(Q)$ data (filled circles).. 23

Figure 9: Idealized cross section of cryostat design and blow up of cell 31

Figure 10: The cell suspension and mounting apparatus. 32

Figure 11: Two piece Vespel cell wall assembly 33

Figure 12: Copper foil sidewall thermometer plane. 34

Figure 13: Linear Stepper Motor (right) and Housing. 35

Figure 14: Design drawing for thermometer substrate 50

Figure 15: PdMn Samples for Magnetic Susceptibility Testing 51

Figure 16: Low temperature cryostat used for susceptibility testing. 52

Figure 17: I-V characteristics of superconducting joints 53

Figure 18: Data collected for a temperature change of 4.5 mK at 2.8 K. 54

Figure 19: Data collected for a temperature change of 2.7 mK at 2.2K 55

Figure 20: Sensitivity of 12.5 μm PdMn film 56

Figure 21: Sensitivity Data from this work, normalized to the peak value of the 0.90% Mn, 50 Gauss test of Klemme, et al. The vertical axis has arbitrary units. 57

Figure 22: Sample and sample holder for susceptibility testing in a variable magnetic field. The sample is potted into a Macor cup inside the brass ring. 66

Figure 23: Assembled apparatus for variable field sensitivity measurements 67

Figure 24: Data taken with a field of 35 gauss at 3.0 K. 68

Figure 25: SQUID Output vs GRT Resistance (temperature) for the data presented in Figure 24. The equation of the best fit line is shown on the graph. 69

Figure 26: Data from the work discussed in chapter three plotted with the data from the 12.5 gauss measurements with the electromagnet.. 70

Figure 27: Sensitivity data for the PdMn film sample, taken with magnetic fields ranging from 6 gauss to 70 gauss. 71

Figure 28: Sensitivity data for the PdMn film sample, taken with magnetic fields ranging from 35 gauss to 250 gauss.. 72

Figure 29: First data taken at 6 gauss. The failure of the two scans to match up at the peak prompted a systematic search for hysteresis effects. 73

Figure 30: Data from Figure 31, plotted versus reduced temperature $t = \frac{T - T_c}{T_c}$, for $t > 0$, with a best fit power law curve. 74

Figure 31: Results of consecutive temperature sweeps at a field of 6 gauss, looking for hysteresis effects. 75

Figure 32: Results of consecutive temperature sweeps at a field of 35 gauss, looking for hysteresis effects. 76

Figure 33: Data taken with a field of 70 gauss below 2.8 K with the best fit line through the data excluding the point at 2.1 K. 77

Figure 34: Data taken at intervals of approximately 0.025 K searching for the dip that appears at approximately 2.050 K.. 78

Figure 35: The data of Figure 34 plotted using the percentage difference between the recorded value and the value of the best fit line at the same temperature. 79

Figure 36: The sample holder for measuring the response of a 1μm thick film with the magnetic field perpendicular to the film surface.. 85

Figure 37: Data for a 0.94 μm thick sample with a field of 12.5 gauss perpendicular to the sample surface. 86

Figure 38: The sample holder for measuring the sensitivity of a 1 μm thick sample with the magnetic field parallel to the film surface 87

Figure 39: Raw data taken at 3.8 K with a magnetic field of 90 gauss..... 88

Figure 40: Data from Figure 39, with SQUID output plotted against the GRT Resistance. 89

Figure 41: Raw data taken at 2.2 K from the same series as the data in Figure 39..... 90

Figure 42: Data taken at a magnetic field of 6 gauss for the 0.94 μm thick film oriented with the film surface parallel to the magnetic field..... 91

Figure 43: Data taken at 35 and 70 gauss for the same sample as in Figure 39, showing the shift in the peak sensitivity versus earlier tests and versus the 6 gauss data depicted in Figure 39..... 92

Figure 44: The Vespel thermometer holder manufactured for use in the thermal boundary measurement apparatus..... 99

Figure 45: Data collected for the 10 μm thick PdMn screen at a magnetic field of 35 gauss..... 100

Figure 46: Data collected for the 10 μm thick PdMn screen at a magnetic field of 70 gauss..... 101

Figure 47: Data for four values of the magnetic field. The data is normalized so that the peak values coincide on the graph. This graph demonstrates the consistent shape of the data as it scales with magnetic field. 102

Figure 48: Data taken over a range of field values using the PdMn screen..... 103

Figure 49: Superconducting Helmholtz coils and sample holder for testing the concept of applying a horizontal field to a sample in the cryostat. 107

Figure 50: Data taken with an unshielded sample at ambient field conditions. 108

List of Tables

Table 1: Tabular data for the measurement of the superconducting joint I-V curve. The data is presented graphically in Figure 17 in the text. 111

Table 2: Tabular data for the measurements with the permanent magnet and the 12.5 gauss measurements with the electromagnet 112

Table 3: Data presented graphically in the text as Figure 27 113

Table 4: Data presented graphically in the text as Figure 28 114

Table 5: Data presented in the text as Figure 29 115

Table 6: Data from 6 gauss hysteresis test presented graphically in the text as Figure 31.. 116

Table 7: Data from 35 gauss hysteresis test presented graphically in the text as Figure 32. 117

Table 8: Data from the 6 gauss test of a 1 μm thick sample with the field parallel to the sample surface depicted in the text in Figure 42. 118

Table 9: Data from the 35 and 70 gauss tests of a 1 μm thick sample with the field parallel to the sample surface depicted in the text in Figure 43.. 119

Table 10: Data from the 35 gauss test of a 10 μm thick PdMn screen with the field perpendicular to the sample surface depicted in the text in Figure 45.. 120

Table 11: Data from the 70 gauss test of a 10 μm thick PdMn screen with the field perpendicular to the sample surface depicted in the text in Figure 46 121

Table 12: Data for the PdMn Screen sensitivity data presented in the text as Figure 48.. 122

Chapter One -- Introduction

Liquid Helium

Helium was the last element to be condensed from the gaseous state, by Heike Kamerlingh Onnes in 1908[1]. Soon afterward, the λ transition was discovered and the subsequent interest in the unusual properties of liquid helium eventually made the phase diagram in Figure 1 one of the best known in physics.[2] This is partly because the phase diagram alone illustrates two aspects of the macroscopic quantum behavior of He. These are the fact that the element does not solidify under its own vapor pressure, even at absolute zero, a fact attributable to its high zero point energy, and the He I – He II phase transition.[3]

Superfluid Helium

Below 2.2 K liquid helium displays some of the most remarkable behavior found in nature. The phase transition from the He I state to the He II state, called the lambda transition because of the shape of the specific heat vs. temperature curve in the vicinity of the transition, is a continuous, non-hysteretic, second order transition from the normal fluid state to a superfluid state. The transition occurs abruptly at 2.1768 K, when, according to the two fluid model (discussed in more detail below), the superfluid fraction of the liquid first becomes non-zero. This fraction, ρ_s / ρ, varies smoothly with temperature, T, going to 1 as $T \rightarrow 0$. The superfluid and normal fluid fractions, as

presented in Figure 2, were first measured as a function of T by Andronikashvili in 1946 and 1948.[4,5] Andronikashvili's first experiment took advantage of the fact that the superfluid fraction in He II has no viscosity. By rotating a set of closely spaced vanes in a volume of He-II and measuring the viscous reaction to the motion as a function of temperature, Andronikashvili produced the data depicted in the graph of Figure 2. He subsequently verified these results with second sound velocity measurements.

Heat Transport in He II

The existence of He II, in which a significant fraction of the fluid exists in a single quantum state describable by a single wave equation, brings the possibility of studying quantum behavior in a macroscopic system into the realm of reality. One of the most fascinating properties of He II is heat transport without a temperature gradient. Investigators at the University of New Mexico, the California Institute of Technology, the University of California, Santa Barbara, Cornell University, Duke University, Penn State University, the University of Delaware, Stanford, and the University of Minnesota, as well as groups overseas, have for nearly two decades focused on the thermal conductivity and heat transport properties of superfluid volumes very close to the λ transition temperature. Much of this work is a continuing investigation of thermal conductivity phenomena first investigated by Kerrisk and Keller[6] in 1967 and Ahlers[7] in 1968, then by Duncan, Ahlers, and Steinberg in the late 1980's,[8,9,10] and by other investigators since then.[11,12,13] The subject has also spurred significant theoretical

interest, most notably culminating in the field-theoretic Renormalization Group (RG) calculations of Haussman and Dohm [14,15,16,17] for heat transport in a nonlinear region very close to the He I - He II interface.

Thermal Boundary Resistance

One physical phenomena of importance to both the experimental and theoretical low temperature physics communities is the role of boundary resistance in the transport of heat into or out of an enclosed He II volume. In the usual theory[18], this boundary resistance is attributed to an acoustic mismatch between the solid endplate and the liquid He II. According to the acoustic mismatch theory, the liquid can only support longitudinal phonon modes and the acoustic impedance, which is the product of the speed of sound and the density of the material, varies by more than a factor of 25 between solids and ^{4}He. Because of this, a discontinuity arises in the temperature at the boundary. The boundary resistance, R_K, gives the temperature drop at the boundary in the usual way:

$$\Delta T_B = R_K Q \ , \tag{1.1}$$

where Q is the heat current applied to the cell.[19] Figure 3 is a schematic representation of the effect of this boundary, or Kapitza, resistance.

Two Fluid Counterflow

The theory of heat transport in He II is very complex. The most rigorous treatments employ field-theoretic RG methods to make predictions of the thermal

conductivity (Haussmann and Dohm)[13] and boundary resistance (Frank and Dohm)[20]. Fortunately, understanding these calculations is not absolutely necessary to understanding the problem that they present for the experimentalist. A less rigorous, but highly instructive, hydrodynamic description provided by Richard Ferrell[21] which is based on dynamic scaling[22] is sufficient to describe our experimental objectives.

He II supports heat transport without a temperature gradient by the mechanism of two fluid counterflow.[23] In the bulk of the fluid, heat is carried by the normal fluid moving in the direction of the heat current. To maintain equilibrium, superfluid moves in the opposite direction so that there is no net mass flow. The process is shown schematically in Figure 4. Under these conditions the superfluid must change to normal fluid at the hot end of the cell and the normal fluid must change to superfluid at the cold end or the counterflow would quickly break down. Landau mentioned this in his landmark 1941 paper on the theory of superfluidity[24], pointing out that the conversion would have to take place within a mean free path of the excitations in the normal fluid (phonons and rotons) from the endplate, and therefore if there was a temperature drop in this region of imperfect counterflow, it would take place entirely within this distance from the wall. The time scale, τ, for this conversion is the important parameter in creating an additional contribution to the Kaptiza resistance. If it is very short, then heat transport is almost entirely by two fluid counterflow. If it grows longer, then there has to be a layer of fluid near the boundary in which diffusive heat flow takes place. When this happens there is a temperature gradient that should, in principle, be measurable as an

additional difference between the endplate temperature and the bulk fluid temperature. This is displayed schematically in Figure 5. Another theoretical speculation by Saslow, in 1971, predicted that in an enclosed volume, there should be a conductive component to the heat transport, resulting in an exponential temperature falloff near a heated surface.[25] Saslow reported that his prediction should be measurable, but also indicated that this temperature difference between the bulk and the edges of the He II should be small compared to the difference between the bulk of the He II and the walls. He also suggested that the difference was within the experimental error of existing measurements, thus making a reinterpretation of boundary resistance values then known unnecessary. In fairness to Saslow, there was no possibility of measuring a temperature gradient in the boundary layer at the time of his speculation.

Length, Time and Temperature Scales: the Ψ Theory

If one intends to probe the boundary layer experimentally, it is essential to understand the length and temperature scales in which the experiment must be conducted. How big is the boundary layer and how does its size vary with temperature close to the λ point? The answers to these questions will determine the spatial and thermal resolution required in our experiment. The question is akin to one of the most fundamental problems of superfluid helium theory: when can the behavior of He II be described by a macroscopic quantum wave function? The Ψ theory of Ginzburg and Sobaynin is the logical place to start.[26] This theory begins with the selection of an order

parameter, the wave equation for which describes the quantum behavior of the system. This order parameter is a complex wave function:

$$\Psi = \eta e^{i\varphi} \tag{1.2}$$

The amplitude and phase of this wave function are related to the density, ρ_s, and velocity, v_s, of the superfluid fraction by:

$$\rho_s = m|\Psi|^2 = m\eta^2 \tag{1.3}$$

$$\text{and} \quad v_s = \frac{h}{m}\nabla\varphi \tag{1.4}$$

where m is the mass of the ^{4}He atom, and h is Planck's constant.

This macroscopic wave function is only useful as a description of the superfluid behavior when the correlation length, ξ, (which can be thought of as the length scale on which the phase of Ψ fluctuates and as a measure of the distance below which low order gradient theories are no longer expected to be valid) is itself a macroscopic quantity near T_λ. That means that the superfluid fraction must be sufficiently small that ξ is much much greater than atomic dimensions. A glance at Figure 2, should be sufficient to convince the reader that this means we must be very close to the λ transition. Ginzburg and Sobaynin have shown that

$$\rho_s = \frac{h}{m\xi}, \quad \text{and}$$

$$\xi(t) = \frac{\xi_0}{t^\upsilon} \tag{1.5}$$

where $t = 1 - \frac{T}{T_\lambda}$ and ν is the critical exponent of the correlation length, which has been experimentally determined to be 0.672.[27] ξ_0 is approximately 1.4×10^{-8} cm. The clear implication is that in order to have a correlation length on the order of 10-100 microns, we must be operating in the temperature range $t < 10^{-7}$.

The next question is about τ, the characteristic time for normal to superfluid transition. Recall that if τ is very short, then we would not expect to find any measurable diffusive heat transport in the boundary layer, but if τ is long, then we would. There has been some disagreement on the exact nature of the scaling law, but Ferrell and others have agreed that τ is proportional to a small power of the inverse of t, in a way similar to the correlation length itself[28]:

$$\tau \sim \frac{\xi^2}{D_\Psi} \quad , \quad D_\Psi \sim \frac{\kappa}{\rho C_p} \sim t^{-\frac{1}{2}}, \tag{1.6}$$

so that

$$\tau \sim t^{-2\nu + 1/2} \ , \tag{1.7}$$

where D_Ψ is the order parameter diffusivity, and κ is the thermal conductivity.

Such a dependence means that as we approach the temperature range of interest, both the correlation length and the time constant are in our favor.

Discovery of the Singular Kapitza Resistance

The first experimental evidence of a contribution to the Kapitza resistance due to imperfect counterflow was obtained in investigations by Duncan, Ahlers and Steinberg (DAS) beginning in 1984. Duncan, et al, were attempting to measure the Kapitza resistance of experimental cells in preparation for a series of measurements on thermal conductivity very near the λ transition. Using high resolution thermometry, they planned to measure thermal conductivity to within a microkelvin of T_λ. In performing these preliminary measurements, Duncan discovered a singularity in the Kapitza resistance between a gold end plate and the He II at T_λ.[8,9,28,29] These experimental findings of an approximate 10 % rise in the Kapitza resistance (Figure 6) between $t = 10^{-3}$ and $t = 10^{-5}$ has spurred some theoretical studies of the topic, most notably those by Frank and Dohm[20], and Frank, Grabinski, Dohm, and Liu.[30] The RG predictions of Frank and Dohm are seen in Figure 7, along with the DAS data. These calculations by Frank and Dohm give a good fit to the DAS data. The objective of this work is to improve the understanding of this singular contribution to the Kapitza resistance and to provide a further test of the theoretical descriptions.

A Simple Model for the Singular Kapitza Resistance

It is instructive to develop at least a simplified equation for the temperature gradient in the boundary layer. The approach here follows that presented in the

dissertation of R.V. Duncan[31] and is based on the Ginzburg-Sobaynin mean field theory[26] and unpublished work by Ferrell. The heat carried by counterflow can be written as

$$Q_s = \left[\left(\rho_s / \rho_n \right) j_n - j_s \right] ST \tag{1.8}$$

Here, ρ_s and ρ_n are the density of the superfluid and normal fluid fractions, respectively. Similarly j_s and j_n are the mass flow densities, $\rho_s v_s$ and $\rho_n v_n$, respectively. At the boundaries, to avoid buildup of either component, both the normal and superfluid currents must vanish and, therefore, the heat current due to counterflow, Q_s, also vanishes, so that all the heat flow in the boundary layer is diffusive heat flow, Q_d. Writing a continuity equation for the superfluid fraction in the boundary region, we have

$$\frac{\partial \rho_s}{\partial t} + \nabla j_s = -\frac{\Delta \rho_s}{\tau} \quad , \tag{1.9}$$

where $\Delta \rho_s$ is defined as the difference between the superfluid density in the bulk and that in the boundary layer. The temperature difference in the boundary layer will be given by

$$\Delta T = \frac{\partial T}{\partial \rho_s} \Delta \rho_s \tag{1.10}$$

and the heat flow equation is, as usual,

$$Q_d = -\lambda \nabla (\Delta T) \tag{1.11}$$

where λ is the thermal conductivity in the boundary layer. For steady state, where there is continuous heat flow and no mass flow, equation 1.9 becomes

$$\nabla j_s = -\frac{\Delta \rho_s}{\tau} \quad . \tag{1.12}$$

If we impose the additional condition of no convection, then $j = j_n + j_s = 0$ and equation 1.11 becomes

$$-\frac{Q_s}{ST}\left(\frac{\rho_s}{\rho}\right) = j_s . \tag{1.13}$$

Combining equations 1.11, 1.12, and 1.13 we get an equation for ΔT,

$$\Delta T = \tau \frac{\partial T}{\partial \rho_s} \nabla \left\{ \frac{Q_s}{ST} \left(\frac{\rho_s}{\rho} \right) \right\} \tag{1.14}$$

To remove Q_s from the equation we substitute $Q_s = Q - Q_d = Q + \lambda \nabla(\Delta T)$, and we obtain a partial differential equation for ΔT, the temperature difference across the boundary:

$$\Delta T = \tau \frac{\partial T}{\partial \rho_s} \nabla \left\{ \frac{Q + \lambda \nabla(\Delta T)}{ST} \left(\frac{\rho_n}{\rho} \right) \right\} . \tag{1.15}$$

If we assume that 1) ρ_n, λ, S, and ρ are all constant, 2) T is equal to the bulk helium temperature T_{He} and 3) $\nabla Q \Rightarrow 0$, then this equation simplifies to

$$\Delta T = \tau \frac{\partial T}{\partial \rho_s} \left(\frac{\lambda \rho_n}{\rho S T_{He}} \right) \left[\nabla^2 (\Delta T) \right] \tag{1.16}$$

If we set

$$\delta^2 = \tau \frac{\partial T}{\partial \rho_s} \left(\frac{\lambda \rho_n}{\rho S T_{He}} \right) \tag{1.17}$$

The equation has a solution

$$\Delta T = \Delta T_0 e^{-z/\delta} \tag{1.18}$$

We can do more analysis of this equation and its solution to try to find an expression for the singular boundary resistance itself (and Duncan, Ferrell, et al have done so)[32], but the essential result is already plain. The boundary layer, under equilibrium heat flow conditions with no mass flow, should have an exponential temperature profile.

The RG calculations of Frank and Dohm, mentioned earlier, predict that the length scale associated with the singular Kapitza resistance should be equal to the bulk correlation length, ξ, of the superfluid.[20] This explains the appearance of measurable effects only very close to T_λ, since ξ (which can be thought of in a crude visualization as proportional to the average distance between atoms occupying the same quantum state – this picture also helps one to understand the importance of fluctuations in ξ), increases as the superfluid fraction of the He II decreases. It is this prediction that makes the direct measurement of the boundary layer temperature so enticing and it is that measurement that is the experimental objective of this ongoing investigation.

We should note that the RG prediction differs from the more complicated length scale, δ, from the Ferrell theory cited above. Additionally, while it is natural to expect single scale-factor universality, similar to the statics, which would result only in the length scale, ξ, Haussmann[33] and Weichman[34], et al, have recently predicted the existence of many characteristic lengths near the interface in the dynamical problem.

The prospect of measuring the thermal profile in the Kapitza resistance and the length scale associated with it is enticing enough to motivate this work, but a second

measurement will also be possible with the same apparatus. It has been shown that for a given value of constant heat flux, Q, there is a temperature $T_c(Q)$, at which counterflow breaks down and an interface forms in the cell between a normal fluid layer (at the heated end) and a superfluid layer. The question of interest is just where this interface first forms, at the end of the cell, or somewhere in the boundary layer itself.

Before summarizing the state of the theoretical and experimental work on this subject, it will be useful to define some of the terminology that has appeared in the recent literature. The terms defined here have been used differently by different authors, creating considerable confusion, but we choose to follow the convention adopted by Harter, et al.[13]:

T_λ is defined to be the lambda transition temperature for zero heat current. T_λ varies with pressure, as can be seen from the slope of the λ line displayed in Figure 1. Under normal gravity, then, there is a hydrostatic pressure variation across a vertical column of helium that leads to a variation of T_λ with height above the bottom of the cell. T_λ varies at a rate of -1.273 μK/cm near the saturated vapor pressure (P_{SVP}) of approximately 0.05 bar.[7] The symbol T_λ should be read as $T_\lambda(P_{SVP})$.

$T_c(Q)$ is defined to be the theoretically predicted temperature at which superfluidity is destroyed within the bulk liquid when a heat current, Q, is passed through a volume of liquid helium. It is lower than T_λ and also depends on the hydrostatic pressure in the presence of gravity in the wame way as $T_\lambda(P)$. The theoretical predictions of Haussmann and Dohm[35] are those most often cited, but there is general

agreement between their predictions and those of Goodstein[36], et al, and Onuki[37], giving the following expression for the reduced breakdown temperature:

$$t_c(Q) = \frac{T_\lambda - T_c(Q)}{T_\lambda} = \left(\frac{Q}{Q_0}\right)^x , \qquad (1.19)$$

where $x = 1/2\nu = 0.746$.

$T_{DAS}(Q)$ is the experimentally determined temperature at which superfluidity is destroyed for a given heat current, Q, based on the data of Duncan, Ahlers, and Steinberg (DAS).[9,28]

The DAS data established the temperatures $T_{DAS}(Q)$ at which counterflow breaks down and superfluidity is destroyed for values of Q below 10 $\mu W/cm^2$. The DAS data give an experimental value for $x = 0.813 \pm .012$, which means that the breakdown temperature is depressed from the $T_c(Q)$ values. The nature of this discrepancy is an active area of investigation for several research groups. $T_{DAS}(Q)$ and $T_c(Q)$ from Haussmann and Dohm are plotted in Figure 8.

Harter, et al,[13] and Duncan[38] have proposed an explanation for the discrepancy between the theoretical and experimental values of x that depends on the details of the singular Kapitza resistance. Andrew Chatto, a co-author on the Harter paper, is responsible for the derivation that follows. They begin, as did DAS, by defining a single boundary temperature, $T_B = (T_{SF} + T_W)/2$, where T_{SF} is the bulk superfluid temperature and T_W is the temperature of the helium next to the wall, at the very edge of the boundary layer. By doing this they find that the Kapitza resistance data from both ends of the cell

collapse onto a single curve. They then plot the logarithm of the singular boundary resistance versus the reduced boundary temperature and find that the data are nearly linear. This means that the temperature drop in the boundary layer, ΔT_b, can be plotted against the heat current with two fitting parameters, β and z:

$$\Delta T_b = Q\beta(t_b)^{-z},$$
$$T_W - T_{SF} = Q\beta\left(1 - \frac{(T_W + T_{SF})}{2T_\lambda}\right)^{-z} \tag{1.20}$$

When the boundary resistance diverges, as it does in the DAS data, this equation implies that T_W blows up, which is precisely the condition for counterflow breakdown. Harter, et al apply this condition by setting $dT_{SF} / d\Delta T_B = 0$, and solving for the exponent x, finding a value very consistent with the DAS data.:

$$\Delta T_b = Q\beta\left(1 - \frac{(T_W + T_{SF})}{2T_\lambda}\right)^{-z} \tag{1.21}$$

$$\left(\frac{\Delta T_b}{Q\beta}\right)^{-1/z} = \left(1 - \frac{(T_W + T_{SF} + T_{SF} - T_{SF})}{2T_\lambda}\right) = \left(1 - \left(\frac{T_{SF}}{T_\lambda}\right) - \frac{\Delta T_B}{2T_\lambda}\right)$$

$$T_{SF} = T_\lambda - T_\lambda\left(\frac{\Delta T_b}{Q\beta}\right)^{-1/z} - \frac{\Delta T_B}{2} \tag{1.22}$$

$$\frac{dT_{SF}}{d\Delta T_B} = \frac{T_\lambda}{Q\beta z}\left(\frac{\Delta T_b}{Q\beta}\right)^{-(1/z+1)} - \frac{1}{2} \tag{1.23}$$

Setting $dT_{SF} / d\Delta T_B = 0$, we get

$$\Delta T_B = \left(\frac{2T_\lambda}{z}\right)^{z/z+1} (Q\beta)^{1/z+1} \tag{1.24}$$

This equation gives the Q dependence of the temperature at breakdown, meaning that the exponent $(1/z+1)$ is the exponent x. Harter, et al[25] found values very consistent with the DAS data, with $x = 0.8163 \pm 0.0023$.

The importance of this explanation is that since the only parameters in the equation are β and z and both are determined entirely from the boundary resistance data, the anomalous value of x is directly attributed to the existence of the singular boundary resistance. One interpretation of this is that the normal to superfluid interface that appears in a cell when T is increased at a given Q evolves directly from the singular boundary resistance.

While this explanation is compelling, there are competing interpretations of the discrepancy between $T_c(Q)$ and $T_{DAS}(Q)$ and one potential way to resolve the issue is to develop thermometry that can probe temperatures in the boundary layer without requiring corrections for the singular Kapitza resistance. By probing the boundary layer directly, it may be possible to determine where dissipation enters the cell, whether it be directly from the heated endplate or somewhere in the boundary layer itself. The experimental apparatus being prepared in this work will be the first to make such a probe possible.

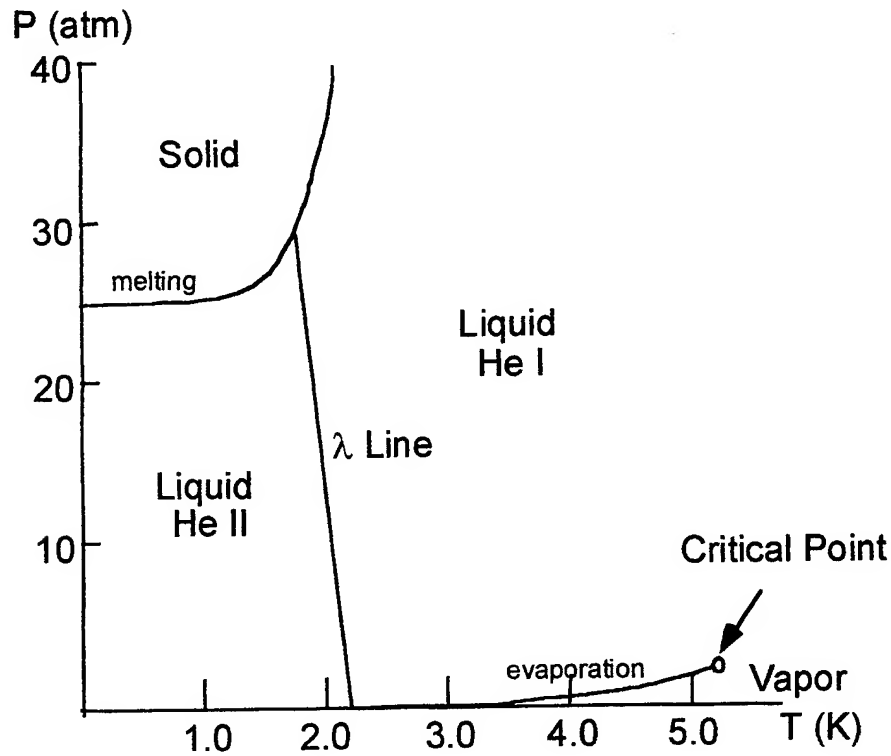

Figure 1: ^{4}He phase diagram, after London (1954)

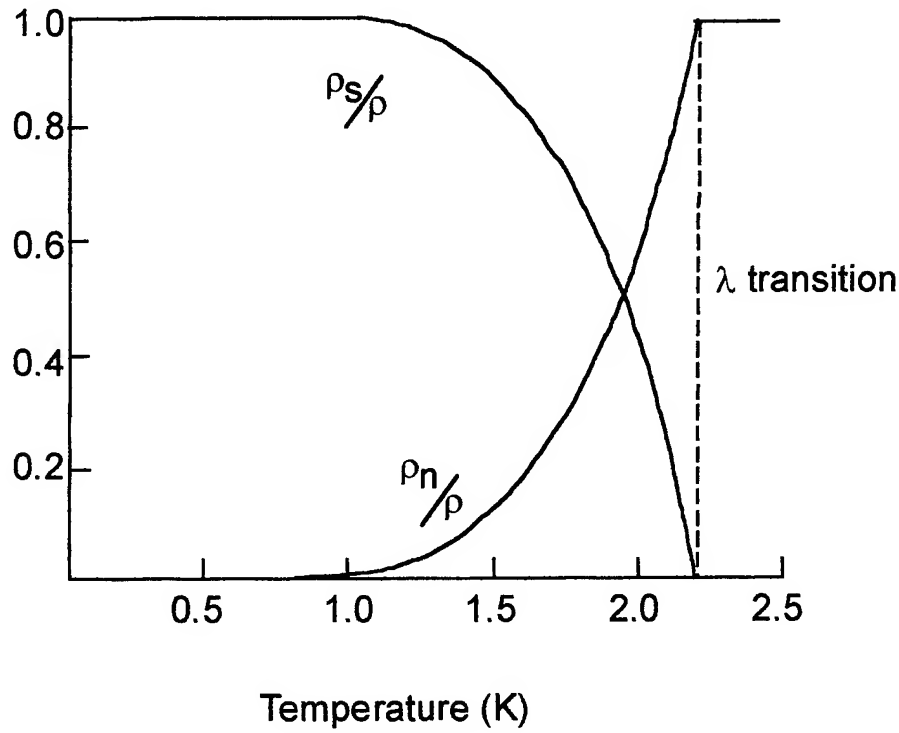

Figure 2 : Proportions of superfluid and normal fluid components, as a function of temperature.

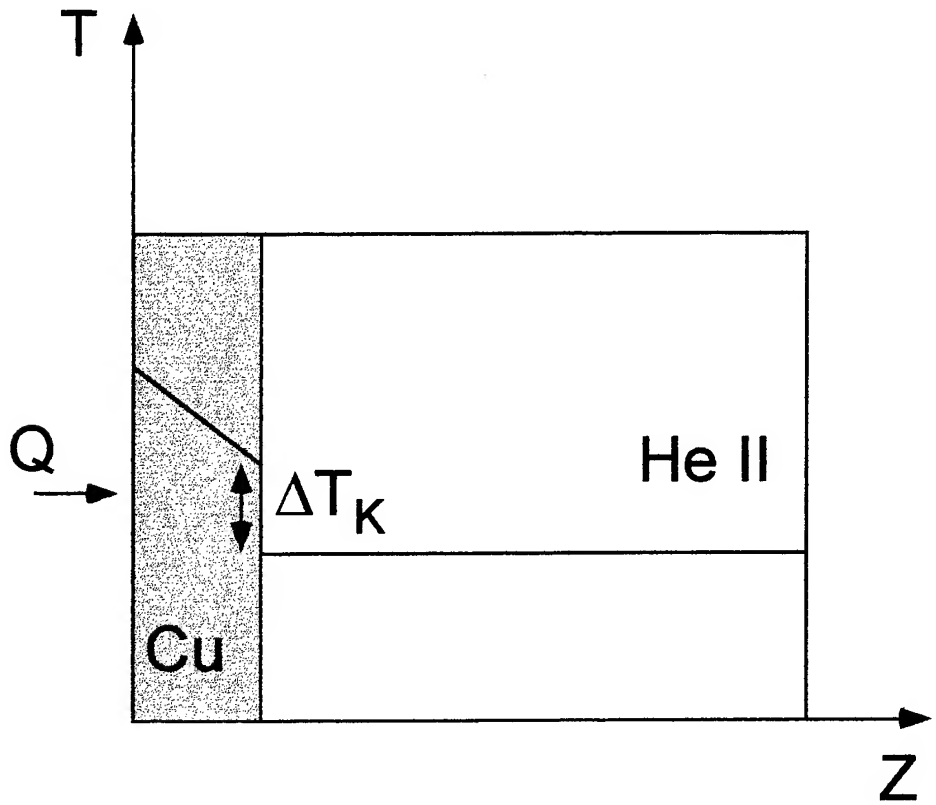

Figure 3: Schematic representation of the effect of the Kaptiza resistance at the boundary between a copper end plate and an adjacent He II volume. With a heat flux applied there is diffusive heat flow and a temperature gradient in the copper, then an abrupt temperature drop, then non diffusive, counterflow heat transport in the He II. There is no helium boundary layer displayed in this figure, consistent with measurements made at $T << T_\lambda$, and hence with $\tau \to 0$.

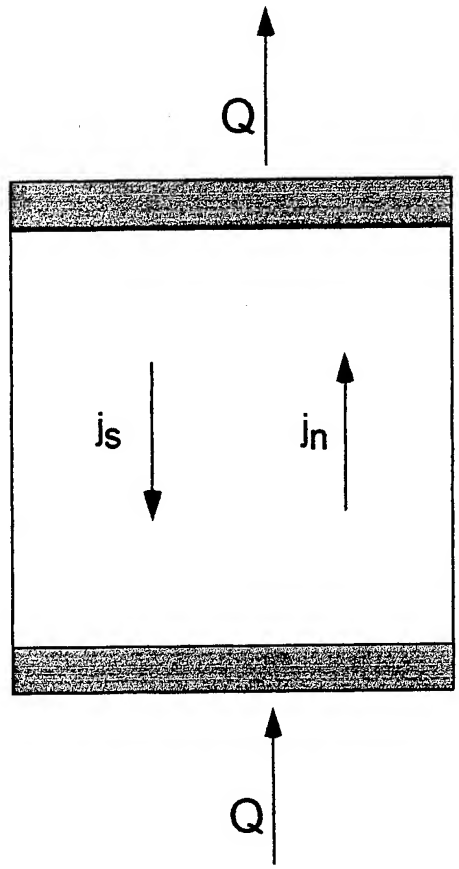

Figure 4: Schematic representation of two fluid counterflow in He II

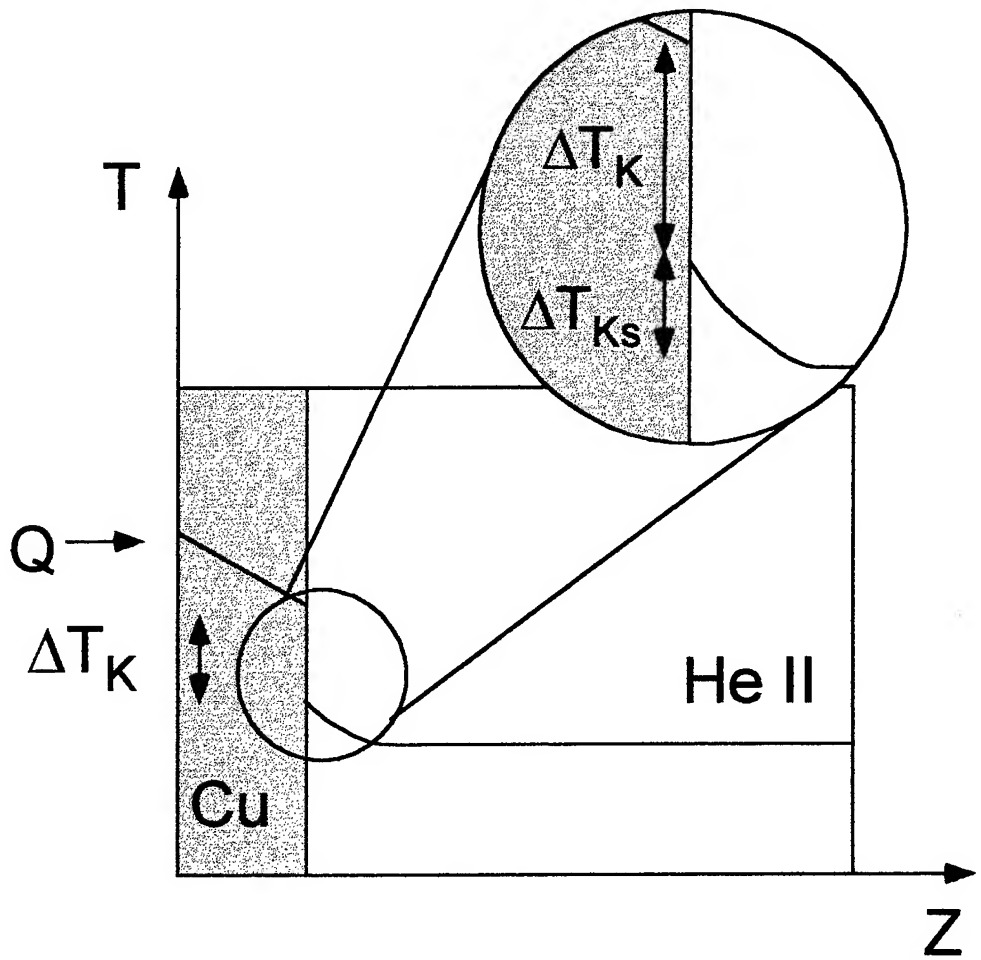

Figure 5: Schematic representation of the effect of incomplete counterflow in the boundary layer between the cell wall and the He II. A thermal gradient results in a thin layer of He in which there is diffusive heat flow, with a corresponding temperature drop. This is the singular contribution to the Kapitza resistance at temperatures very close to T_λ.

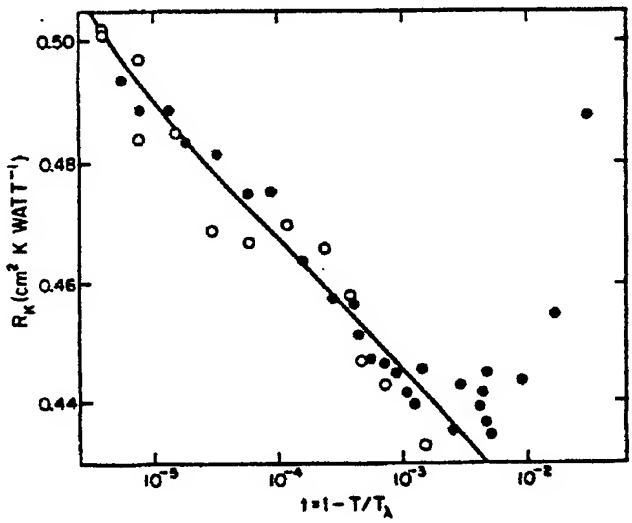

Figure 6: Kapitza resistance vs. reduced temperature; DAS data[8]. The open and closed circles distinguish between data taken in different cells that were constructed using very different technology. The solid line is from hydrodynamic theory, but is adjusted to fit the data.

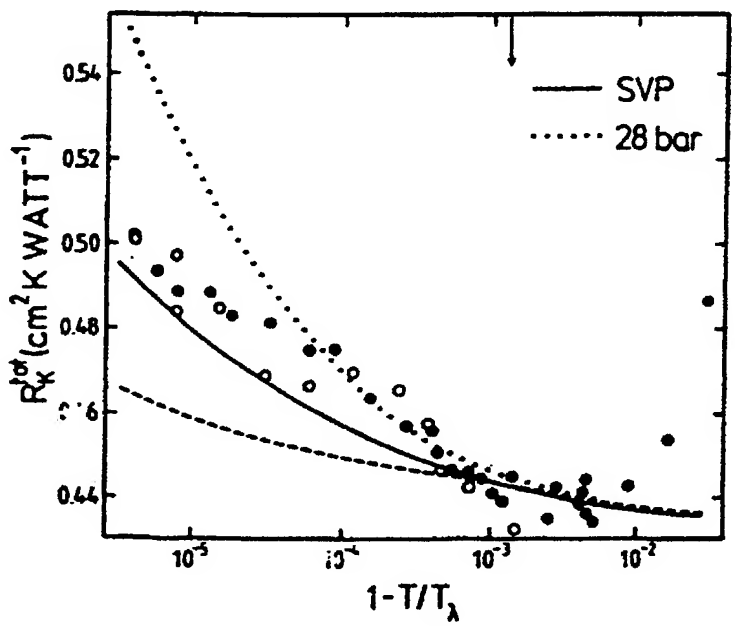

Figure 7: RG calculations of Frank and Dohm[20] (solid and dotted lines) with the DAS Singular Kapitza Resistance data.[8] The solid and dotted lines represent predictions at saturated vapor pressure and at 28 bar, respectively. The dashed line, for comparison, is a renormalized , hydrodynamic approximation, which is much less accurate at modeling physics at length scales less than ξ.

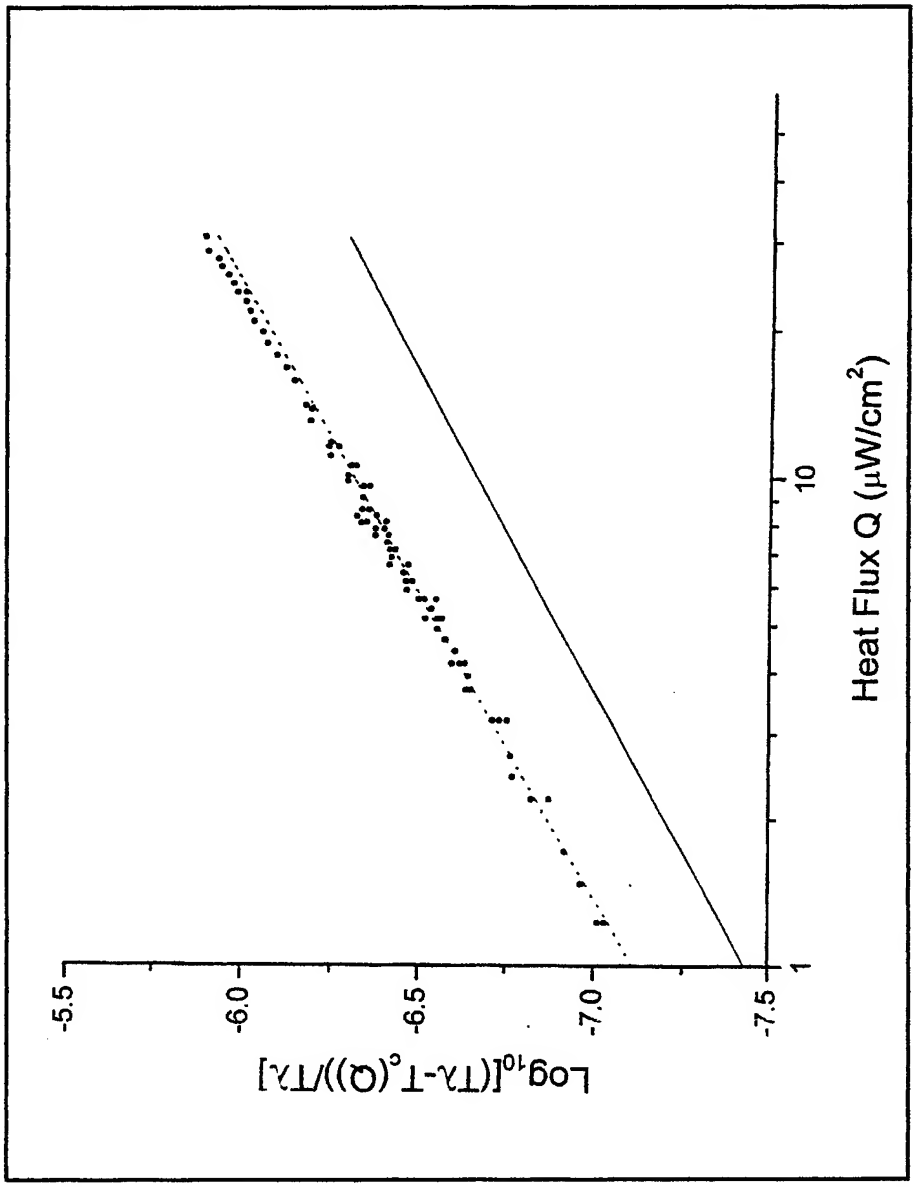

Figure 8: Logarithm of reduced breakdown temperature vs. heat current, Q, based on Haussmann and Dohm $T_c(Q)$ theory (solid line) and $T_{DAS}(Q)$ data (filled circles). The dashed line is a parametric fit by Duncan.

Chapter Two – Experiment Design and Construction

The ultimate objective of this work is to facilitate measurement of the boundary layer temperature profile in a superfluid helium cell with a heat current applied. As described in Chapter One, the theory, though very difficult, yields a surprisingly elegant and, in principle, easily testable result. The temperature in the region very close to the cell wall, where two fluid counterflow is expected to break down, should have an exponential temperature profile with a constant that is equal to the bulk correlation length of the superfluid fraction. This profile should be measurable over a distance of about three times the correlation length.

In order to carry out such an experiment, it is necessary to design, test, and manufacture an in situ, or "wet," thermometer that can measure temperature with high resolution at very precisely controlled positions inside the cell. This requirement carries with it a set of three demanding requirements for the temperature sensing element itself. First, it must be porous enough not to interfere with two fluid counterflow. Second, it must be thin enough, on the order of a correlation length, to measure the temperature at a precise distance from the cell wall. Third, it must be a high resolution sensing element, capable of resolving nanokelvin temperature differences at μm length scales.

This set of requirements immediately calls to mind the recent development of bulk metal high resolution thermometry at the University of New Mexico. The development of high resolution thermometers (HRTs) based on dilute ferromagnetic

alloys of PdMn and PdFe by Klemme, et al[39], lead us to conclude that a sensing element made of PdMn alloy would be the thermometer of choice for this experimental objective. The design, manufacture, and testing of the PdMn sensing element is the subject of subsequent chapters of this dissertation. In this chapter we are primarily concerned with the engineering design of the cryostat, cell, and actuator mechanism intended to put the thermometer in the right place and move it through the boundary layer.

Cryostat Selection and Modification

It was intended from the beginning to mount the experimental apparatus on a previously existing cryostat. This cryostat is an RMC[40], Inc. design with a 4" vacuum can and a 4 mole sorption pumped ^{4}He refrigerator. The cryostat was designed as a dippable probe[41,42] without any usable facility for filling or refilling the dewar after the cryostat was in place. Because we anticipated taking data over long periods, we rebuilt the cryostat with a collar to fit a 4.5" neck Precision Cryogenics[43] dewar, a new set of baffles to fit the dewar neck and a 3/8" Swagelok fitting to facilitate filling and refilling the dewar.

The vacuum space available for the experiment itself was 14" long and 3.8" in diameter and had to include the cell, the suspension system, the cryogenic valve, the SQUIDs, a radiation shield, a flux tube, and a superconducting magnet. In addition, all of the electronic connections would have to pass through a 3/4" central vacuum line.

Cell and Suspension Design

What follows is a description of the experimental apparatus, including the rationale for important design decisions when appropriate. Figure 9 is an assembly view of the design.

The electrical contact array provides a fixed point in the cryostat from which the entire new assembly hangs. The combined radiation shield and flux tube is a brass tube 13.5" long with a step machined into its length, giving it a lower section with a 2.50" OD and an upper section with an OD of 2.75". A set of eight countersunk holes at the top allow for attachment to the lower copper ring of the electrical contact array. The step in the radiation shield allows for a second brass tube with the superconducting magnet solenoid wound around it to slip over the lower portion. The magnet assembly has an OD of 2.75" to match the upper portion of the radiation shield. Two small holes drilled into the step allow the magnet wires to pass through into the experiment space where they connect to wires that run up the central vacuum line.

The entire flux tube is electroplated with a layer of copper and a 1.5 mil thick coating of pure tin. The copper prevents migration of zinc from the brass through the tin coating. The tin coating serves as the flux tube for trapping magnetic field. Tin was chosen because of its Curie Temperature, T_c, of 3.72 K. Since we intend to cool this cryostat by pumping on the bath, using a flux tube with a T_c below 4.2 K allows us to wait until we start pumping on the bath to turn on the magnet and then trap flux during the cooldown to 2 K. Also, the niobium tubes surrounding the HRTs and SQUIDs, and

the niobium capillaries carrying the SQUID pickup wires will be superconducting before the field is applied, providing optimum shielding. At the bottom of the flux tube a threaded brass cap closes the radiation shield and holds the magnet in position.

The experimental assembly (Figure 10) is provided two points of attachment to the radiation shield. Two rows of countersunk screw holes in the shield allow the cell bottom plate and the SQUID mounting plate to be attached via threaded holes drilled radially inward on these two plates. In practice, it has been determined that attachment at the top plate only is optimal, to avoid adding stress to the apparatus during cooldown. Additionally, a nylon ring with a u shaped groove on its inside diameter fits over each of these two plates to provide some insulation between the plate and the radiation shield. A set of three stainless steel rods machined with a shoulder and thread at each end fit between the cell bottom plate and the SQUID mounting plate. The cell top plate is attached to a stainless steel spool that slides along these three stainless rods. Between the cell top plate and the spool there is a Teflon[44] insulating ring. On the top of the spool is a nylon insulating disk with a cylindrical aluminum clamp mounted to its center. This clamp has a hollow setscrew through which a filament passes before being tightly clamped at the bottom of the screw. This filament runs through the central vacuum line to the top of the cryostat where a linear stepper motor pulls on the filament to actuate the cell expansion.

The cell itself is constructed with a two piece Vespel[45] outer wall (Figure 11), a phosphor bronze bellows, and a Vespel inner cylinder that serves as the thermometer

mount. The lower portion of the outer wall has a step at the top with three equispaced tabs extending above its rim. The upper wall rests on the shelf of the lower wall and the two pieces make a flush inner wall. The tabs are gluing surfaces that provide extra shear strength for the cell wall when the cell is placed under tension to expand the integral bellows. The bottom of the phosphor bronze bellows, which is soldered to the cell top plate, fits into a groove machined into the flange in the upper cell wall and is bonded into place with Tra-Bond 2151 epoxy[46]. A sidewall thermometer plane made of 5 mil 99.999% pure copper foil fits over the tabs on the lower cell wall and is glued in place with Tra-Bond 2151 as the cell wall is assembled. The foil was cut by Electron Discharge Machining to fit with very fine tolerance over the tabs (see Figure 12). The cell top and bottom plates are gold plated and as can be seen from the blow up of the assembly drawing in Figure 9, are machined with grooves and steps for fitting the parts of the cell wall together. The Vespel inner cylinder has a step machined into its inner diameter at the lower end and a flange around the outside. The step accommodates the thermometer screen and the flange provides a place for winding the SQUID pickup coil. When the cell is in its relaxed position the thermometer screen rests against the raised step on the bottom plate.

There are two penetrations of the cell top plate. One in the center provides for filling of the cell with liquid helium. A copper-nickel capillary joins this orifice to a vapor pressure pot that mounts on the top of the spool. The pot can be seen in the left side of Figure 10. The second penetration has a niobium capillary inside a copper-nickel

capillary through which the SQUID pickup wires leave the cell and is sealed with epoxy as one of the final steps in assembly. From the vapor pressure pot another capillary runs up into the top of the experiment space where a miniaturized cryogenic valve is suspended above the SQUIDS. The cell bottom plate has two additional threaded holes for mounting the PdMn HRTs that are used to record the temperature at the sidewall plane and on the bottom plate itself. One of the Vespel[45] HRT mounts can be seen in Figure 10.

Cell Actuation and Positioning

Several alternatives were explored for cell actuation and positioning. Early ideas focused on piezoelectric actuators and linear stepper motors. Piezoelectrics were intriguing, but the expense, fragility, and difficulty of cryogenic preparation are significant drawbacks. Additionally, the sub nanometer resolution was not necessary for this work and the high voltage feedthroughs required raised the possibility of additional electrical interference with the experiment. The idea for a filament connected to a motor to pull on the cell top originated with Dr. Steve Boyd of the DYNAMX group. The motor selected was provided by TS Products[47] and has sub-micron resolution and the ability to pull and hold 150 pounds. It is controlled through a simple command library using serial communications through a PC. Our motor was vacuum prepared so that it could be mounted in the top of the cryostat head. An aluminum housing was manufactured to hold the motor and to seal to the top of the cryostat. An O-ring seal at

the bottom and a vacuum electrical feedthrough at the top of the housing seal the motor in the vacuum space. The motor and housing are pictured in Figure 13.

Instrumentation

There are three high resolution thermometers (HRTs) incorporated into the design of this cryostat. One is the screen thermometer for the direct measurement of the boundary layer profile. The other two are to record the temperature of the bulk helium through the copper sidewall thermometer, and the third will directly monitor the temperature of the bottom plate. In addition, a Lake Shore Germanium Resistance Thermometer[48] (GRT) and 1 kOhm heater mounted on the cell bottom plate will be used to monitor the cooldown and to control the temperature of the lower stage. The HRTs are each coupled inductively to individual Quantum Design[49] DC SQUIDS, mounted on the top plate of the apparatus, as seen in Figure 10. The SQUID pigtails run through the central vacuum line to the top of the cryostat, where they connect to the preamplifiers. These preamps are all connected to a Quantum Design QD5000 DC multi-channel SQUID controller. The GRT and heater are controlled and monitored through a Linear Research[50] LR-700 AC Resistance Bridge.

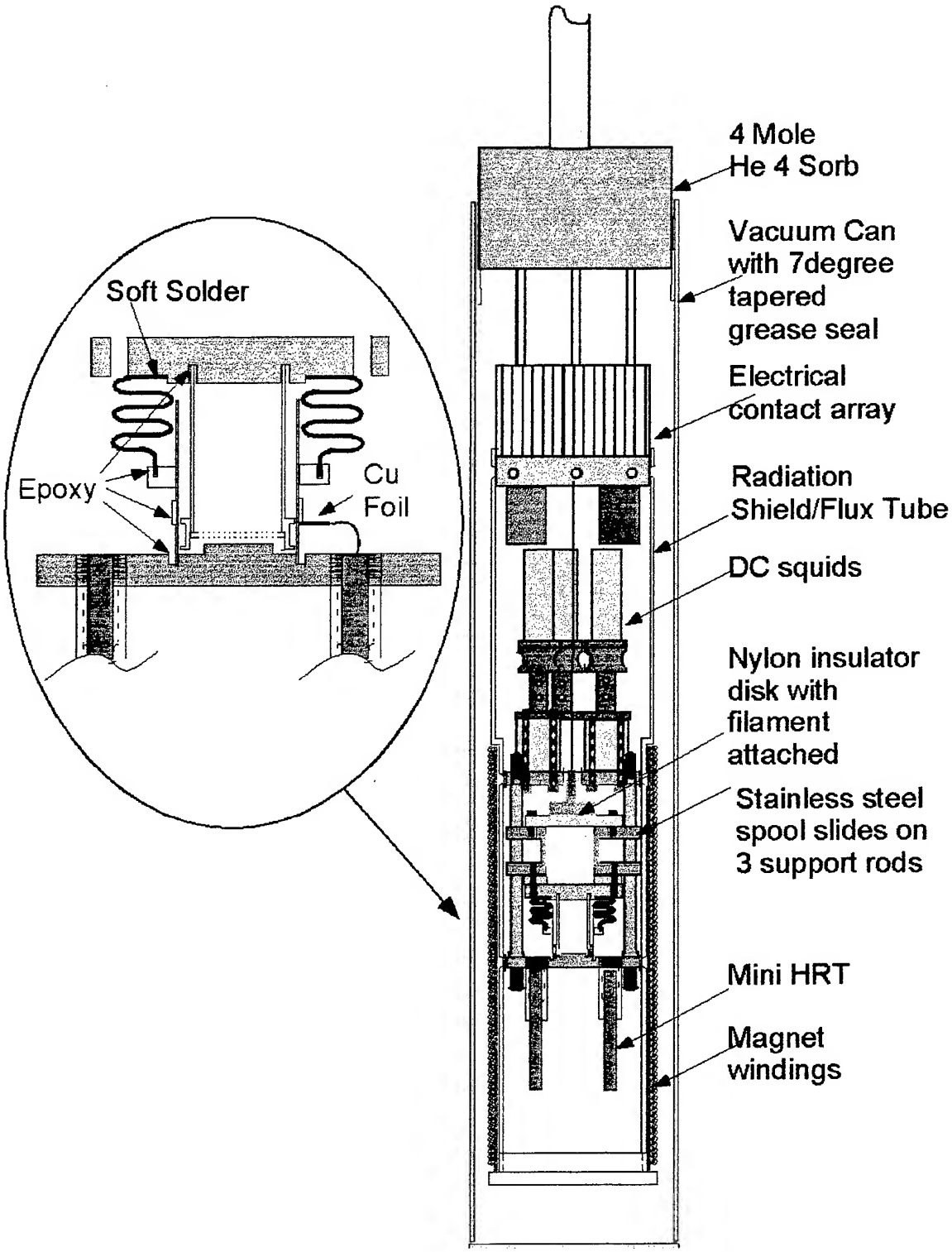

Figure 9: Idealized cross section of cryostat design and blow up of cell

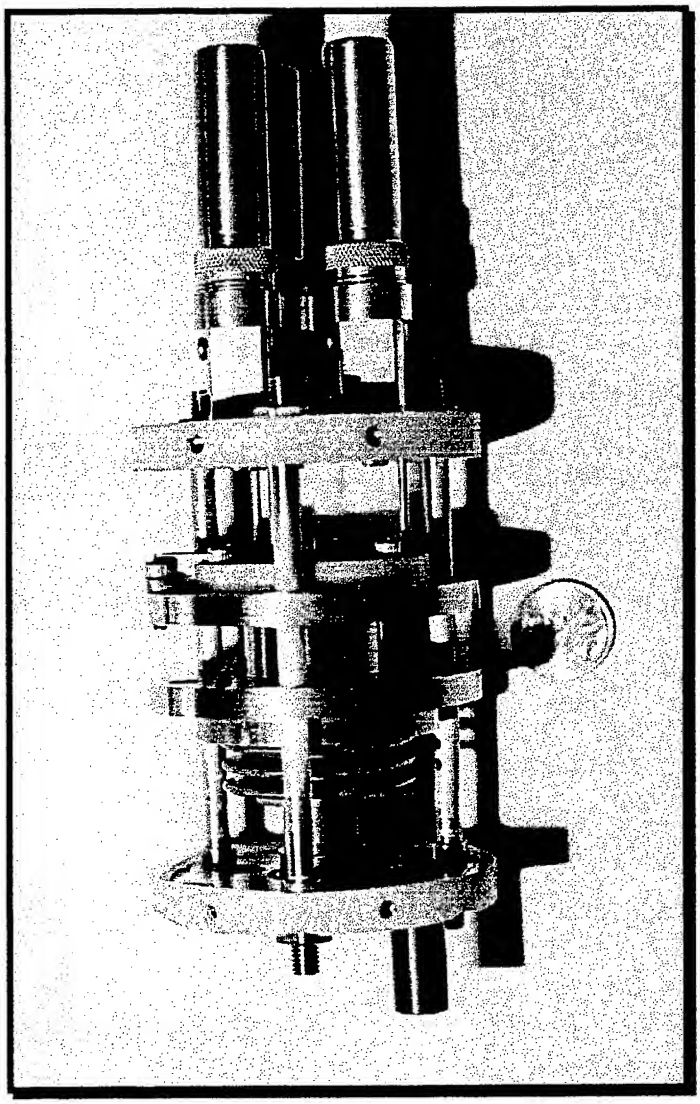

Figure 10: The cell suspension and mounting apparatus. The outer cell wall, SQUID mount extensions and filament clamp are not installed.

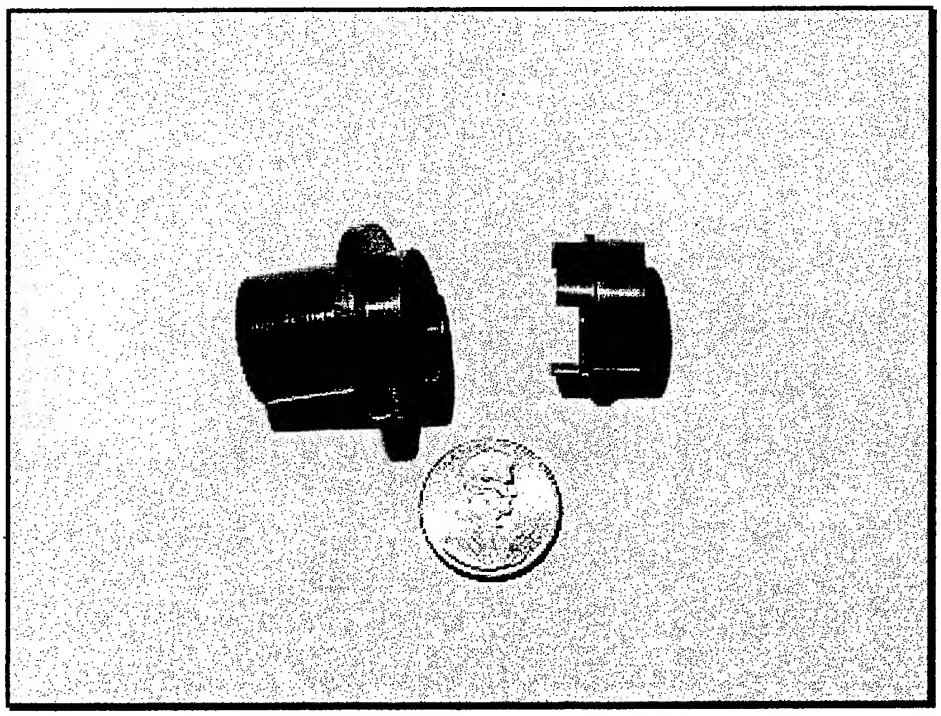

Figure 11: Two piece Vespel[45] cell wall assembly.

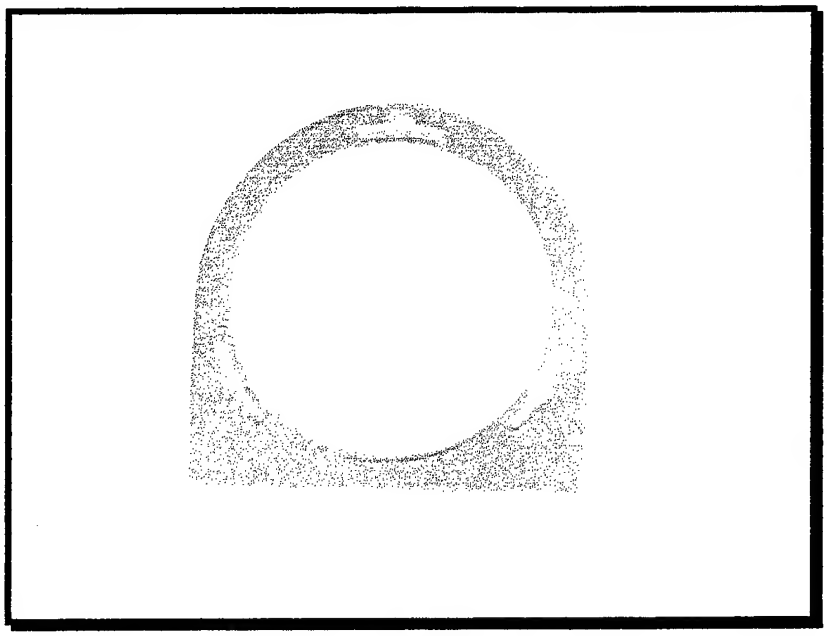

Figure 12: Copper foil sidewall thermometer plane. The foil has been cut by electron discharge machining to fit precisely over the gluing tabs on the Vespel[45] cell wall seen in the previous figure.

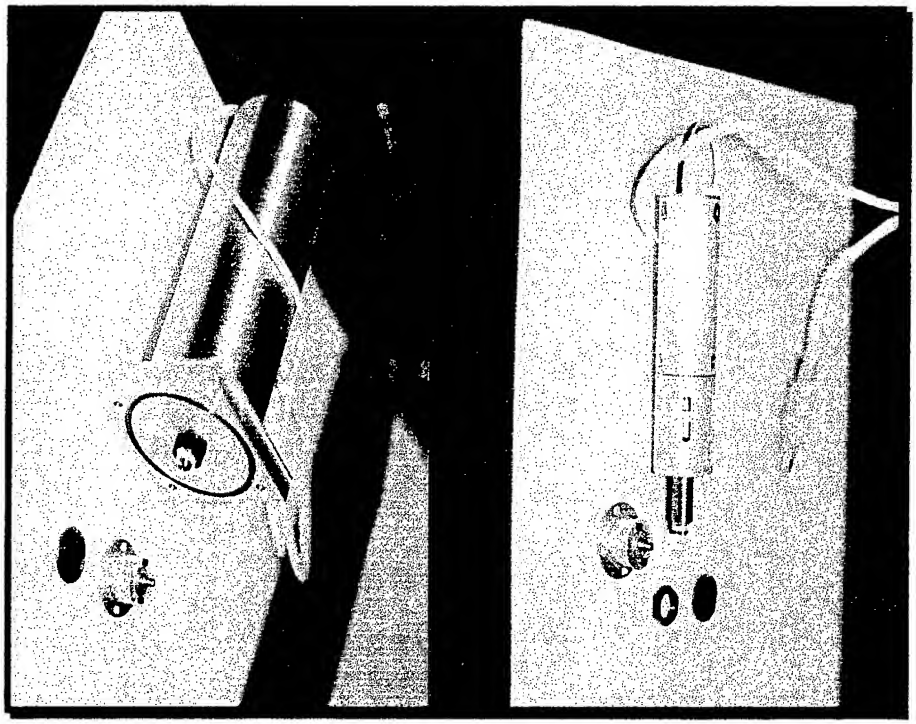

Figure 13: Linear Stepper Motor (right) and Housing.

Chapter Three -- PdMn Thin Film Thermometry

Initial Planning

The original idea for an in situ, or "wet," thermometer was to draw the PdMn alloy into wires of approximately 10 microns diameter and to construct a grid of such wires that would function as the thermometer. To evaluate the possibilities of mounting such a grid of wires in the experimental cell, we consulted with experts at Team Specialty Products[51] of Albuquerque. Their familiarity with ultra fine wires of refractory metals was developed during years of developing and building Z-pinch targets for the large X-ray simulator machines at Sandia National Laboratories. During these initial discussions we also explored the possibility of using a vapor deposition technique to create a film of the desired alloy. The major problems with this approach were identified as 1) achieving the desired film stoichiometry and uniformity, 2) achieving a porosity sufficient to avoid interference with superfluid counterflow, and 3) creating a thermometer sufficiently rigid to avoid the problem of microphonics inherent in using a thin membrane as the thermometer element. We eventually settled on the idea of sputtering onto a perforated substrate of fused silica. Fused silica provides an optimum combination of thermal conductivity (0.00054 ± 15% W/cmK at 2 K)[52] and machinability, and has the added benefit that sputtered Pd sticks without special treatment or underlayers. Low thermal conductivity is desired to provide maximum thermal standoff between the PdMn film, in the boundary layer, and the top of the

substrate, in the bulk He II. Additionally, it has a high softening temperature, significantly higher than other glasses, which would allow annealing of sputtered films to increase their magnetic sensitivity, if necessary.

Thermometer Design

The design of the actual film thermometer required analysis of several parameters. The amount of PdMn material was the first consideration. It became apparent from a preliminary calculation that the amount of material in the proposed wire grid array was far too small to produce a sufficient response in the SQUID pickup loop. A balance had to be drawn, therefore, between the amount of material and the porosity of the film. A porosity of about 60 to 70 percent on a 1 cm diameter substrate with a 10 micron coating of material proved sufficient to give a hypothetical sensitivity of a few hundredths of a flux quanta per microkelvin. Additionally, it was desired that both the hole diameter and the spacing between holes be larger than a correlation length, in order that the screen should be essentially transparent to the superfluid. The diameter and spacing of the holes to be drilled in the fused silica disk were adjusted to achieve machinability and to meet these requirements. The pattern chosen for the grid was a honeycomb array (closed packed) of 182 holes with a hole diameter of 600 microns and a spacing between holes of 125 microns, as seen in Figure 14.

Machining of the fused silica disks to be used as the thermometer substrates was the next challenge. We explored several possible techniques, including laser cutting,

water jet cutting, and sonic milling. The latter process proved to be the technique of choice because it produces clean, repeatable patterns with almost no stress introduced into the workpiece. Essentially the process requires the production of a tool head that is a negative of the pattern to be cut out of the material. This tool head is mounted on a sonic horn and held very close to the workpiece. It is used to vibrate a slurry of abrasive material that does the actual cutting. The tool never touches the work, resulting in almost no residual stress in the piece. This work was performed by Sonic Mill[53] of Albuquerque, NM. Starting with a disk three eighths of an inch in thickness, the pieces were drilled at Sonic Mill, then sent to Valley Design[54] in Boston, MA to be lapped down to a thickness of 125 microns. Unfortunately, Valley Design was also required to reduce the outside diameter to the final dimensions and they experienced a failure during this part of the work. Fortunately, we had asked them to thin two unperforated disks simultaneously. Sonic Mill was able to drill these already thinned disks successfully and we had two thinned, perforated disks that were very close to the specifications.

Film Deposition

With the thermometer substrate designed and the manufacturing process underway, our attention turned to the vapor deposition technique for creating the alloy film. Several options were explored, including two boat sputtering from separate targets, sputtering from a single alloy target, and chemical vapor deposition from thermally isolated reservoirs. Experts in the field, including Chris Krannenberg of the

University of New Mexico's Center for High Technology Materials, and John McKenney of Sandia National Laboratories Materials Processing and Coatings Lab were consulted. McKenney expressed confidence that the material could be deposited from an alloy target, producing a film with approximately the same stoichiometry as that in the sputtering target. There are several alloy materials that are routinely sputtered from alloy targets, including Permalloy (81% Ni and 19% Fe) and Ni-Cr in various concentrations, and which are known to produce films that mirror the concentrations of the constituents in the sputtering target.[55] Despite this, PdMn presents a new challenge, especially since the normal method of producing Mn coatings is through resistively heated evaporation in a tungsten boat and not through sputtering.[56]

The general principal behind sputtering from an alloy target is that if the target, chamber and substrate are allowed to come to thermal equilibrium before the substrate is unshuttered, a surface modification process takes place in the alloy target. If the alloy target is homogeneous, and the constituents occur in concentrations with the same order of magnitude, then the species with the higher sputtering rate will initially be sputtered preferentially. This creates a surface layer in which the concentrations of the two constituents are altered.[57,58] The end result is that the film concentration is approximately equal to that of the target. In the case of a very dilute alloy, however, we can show that surface concentration will change, after which both constituents will sputter at the rate of the more prevalent species. The following mathematical description of the process is

based on Patterson's work.[57] For a binary alloy target with species A and B, the surface concentration of the two species changes with time according to these equations:

$$A(t) = \frac{S_B N_0 A_0}{A_0 S_B + B_0 S_A} + \left[A_0 - \frac{S_B N_0 A_0}{A_0 S_B + B_0 S_A} \right] \exp - \left(\frac{A_0 S_B + B_0 S_A}{N_0^2} Ft \right) \tag{3.1}$$

$$B(t) = \frac{S_A N_0 B_0}{A_0 S_B + B_0 S_A} + \left[B_0 - \frac{S_A N_0 B_0}{A_0 S_B + B_0 S_A} \right] \exp - \left(\frac{A_0 S_B + B_0 S_A}{N_0^2} Ft \right) \tag{3.2}$$

A(t) and *B(t)* are the surface concentrations of the two species at time *t*, while A_0 and B_0 are the initial concentrations. S_A and S_B are the sputtering yields for the two species, in sputtered atoms per ion. *F* is the ion current density at the target and N_0 is the atomic density of the target surface. These equations are valid when the initial sputtering yields are the same for the alloy constituents as they are for pure elemental targets and when the atomic weights of the two materials are close together. In our case, if Mn is species B, then with a density B_0 of only 0.0068 N_0, we can simplify these equations:

$$A(t) = N_0 + [A_0 - N_0] \exp - \left(\frac{S_B}{N_0} Ft \right) \tag{3.3}$$

$$B(t) = \frac{S_A B_0}{S_B} + \left[B_0 \left(1 - \frac{S_A}{S_B} \right) \right] \exp - \left(\frac{S_B}{N_0} Ft \right) \tag{3.4}$$

These equations suggest that for a very dilute alloy of species B in A, the time constant for variation in the surface is given by

$$\left(\frac{S_B}{N_0} F \right)^{-1}$$

such that, as $t \rightarrow \infty$,

$$B(t) \rightarrow \frac{S_A B_0}{S_B} \tag{3.5}$$

Equation 3.5 implies that if the sputtering yield of B is lower than that of A, the concentration of B increases in the surface and vice-versa. Once the surface reaches this state, equation 3.5 shows that both species sputter at the rate of the primary constituent, since the instantaneous film compositions for species A and B are always

$$A_S = \int_0^t S_A A(t) dt \tag{3.6}$$

and

$$B_S = \int_0^t S_B B(t) dt \tag{3.7}$$

Since we shutter the surface during the period which the surface composition in the target changes, the instantaneous film composition is the asymptotic value:

$$A_s = S_A A_0 \tag{3.8}$$

$$B_s = S_A B_0 \tag{3.9}$$

So once the surface has equilibrated, the amount of each constituent deposited in a given time is proportional to its original density in the target and the proportionality constants are the same. By shuttering the substrate until the surface modification has taken place, we should be able to produce a film with characteristics very similar to the target. Available data suggest, however, that this process is far from exact, especially with an alloy as dilute as we are considering. One particular study, for example showed that for a

given range of aluminum alloy target compositions, the sputtered films all turned out basically identical[54], suggesting that repeated attempts to alter the film composition by using differently composed targets may be fruitless, especially when one considers the expense of Pd targets (several thousand dollars each).

Unfortunately, because there is almost no information available about Mn sputtering yields, the first attempt at producing a film involved some guesswork. The linear cascade theory of Sigmund predicts a sputtering yield for Mn that is very close to that of Pd, 1.8 vs. 1.9 atom/ion when sputtered with 400 eV Xe^+ ions.[59] However, the 1958-62 series of experiments by Wehner and his co-workers show that the theory, yields just about its worst results for Mn out of all the elements tested. Tellingly, Wehner never reported results on sputtering of Mn with Ar, Ne, or Hg working gasses. [60,61,62] Based on this somewhat scanty knowledge, but reasonably confident that the more important number was the sputtering yield of Pd, we ordered a sputtering target from Target Materials Inc,[63] with a concentration of Mn in Pd of 0.68 atomic percent. We chose this concentration because, relying on the experience and advice of Dr. John McKenney of Sandia, we expected some enhancement of the Mn concentration. We delivered the sputtering target to Z Supporting Materials and Coatings Laboratory at Sandia National Laboratories so that samples could be delivered for testing prior to sputtering the film onto the finished substrates. Dr. McKenney produced three samples with a 12.5 micron coating of PdMn alloy on Pyrex[64] substrates 23.14 mm by 6.19 mm by 1 mm thick, as shown in Figure 15.

Sample Testing

The testing of the sample film thermometers was the first truly experimental phase of this work. The experiment was carried out using the same cryostat that Klemme, et al used to test cylindrical pills of PdMn and PdFe alloys for magnetic susceptibility.[39] The experimental setup was also similar. Figure 16 is a schematic of the cryostat. The rectangular sample and a permanent cobalt samarium magnet to provide the flux tube magnetic field charge were separately mounted in custom holders. In the case of the magnet, a Macor[65] machinable ceramic disk was drilled so that the magnet could be press fitted into its center. This Macor holder was then surrounded by a split brass ring that was machined to an outside diameter such that it fit tightly into the cylindrical niobium housing provided with a Quantum Design[49] DC SQUID. This combination of Macor[65] and brass, materials that contract less than and more than the niobium tube, respectively, ensured that the sample would remain tightly held inside the niobium tube at low temperatures to minimize the possibility of microphonics. The use of these low electrical conductivity materials and the step of splitting the brass ring on one side ensured that eddy current noise would be held to a minimum. A half size (1 cm long) sample was mounted vertically into a Macor[65] cup and potted with Tra-Bond 2151 epoxy.[46] Then it was clamped in a split brass ring in the same fashion as the magnet. A 2.2 μH coil of 0.004" copper clad niobium - 48% titanium wire was wound tightly and directly around the sample. Copper clad wire was used here because the rectangular sample had sharp corners and the added malleability of the copper made the coil more

durable than those attempted from unclad wire. One of the most difficult parts of this experiment proved to be the mating of this coil with the existing SQUID pickup wire, an unclad 0.003" niobium-titanium wire that already had a hermetic penetration of the vacuum can.

Preparation of Superconducting Joints

Superconducting joints with large critical currents are difficult to produce in practice, although certain techniques were well understood by members of our research group. The procedure that was used to produce sound, persistent superconducting joints was a twist and crimp method. First both wires were stripped and sanded to remove their insulation layers. The copper clad wire was then dipped in nitric acid to remove the copper layer and rinsed in distilled water. A surgical clamp was used to clamp the two wires to be joined so that their ends could be twisted tightly together for a length of about 5 mm. Once the wires were twisted together a small helix of SnPb solder was wound around a 10 mil outside diameter capillary and slipped over the twisted ends. Touching a hot soldering iron to this helix immediately melted away most of the solder, but left a discernible, spotty wetting of solder on the twisted wires. Then a 10 mil ID, 5 mil wall Cu Ni capillary was slipped over the twisted and wetted wires so that the two wire ends barely stuck out of the capillary. This capillary was heated with a soldering iron and the inside of the capillary filled with SnPb solder. Finally, the capillary was flattened with pliers, then crimped repeatedly along its length to ensure a good joint, with the final

crimp cutting off the capillary just before its end. Since two cooldowns of the apparatus were scrapped due to an open SQUID pickup loop, we decided to test the joining procedure. This we did by making a simple dipper probe with two such joints between two lengths of copper clad wire. The wires were stripped and sanded outside these joints and voltage pickoffs were soldered onto them to facilitate a four wire resistance measurement. This probe was dipped directly into a helium storage dewar and the critical current was measured using a metered current supply and a digital multimeter. The I-V characteristics of this loop are depicted in Figure 17 and in tabular form in Table 1, Appendix A. This test was sufficient to convince us we could make a superconducting joint with persistent characteristics that would allow the testing of the samples to continue. The hysteresis evident in Figure 17 is likely due to complicated aspects of the wire structure itself, but in any case is not of concern in determining the utility of the superconducting joint.

Measurement Apparatus

The sample stage was heated and controlled through a 1kΩ metal film resistor and Lake Shore Germanium Resistance Thermometer[48] (GRT) combination mounted to the bottom of the stage just below the thermal filter depicted in the schematic. Both GRT monitoring and temperature control were accomplished with a Linear Research LR-700 AC Resistance Bridge[50]. Due to the poor thermal conductivity of the brass, Macor[65], and Pyrex[64] in the mounting of the sample, there was a long time constant for

equilibration of the sample and the heating stage, measured at 9 minutes. This meant that each data point would take approximately half an hour to collect. Additionally, acoustic interference was a major difficulty early in the testing of the apparatus. Because of these long data collection times, both the LR-700 and the Quantum Design[49] QD5000 DC SQUID controller were connected to the General Purpose Interface Board (GPIB) bus of a PC running the Linux operating system. A program was prepared to acquire the resistance of the GRT and the voltage output of the SQUID every second during a data run. To collect a single data point, the experimentalist would set the starting temperature, typically an excursion of 0.1 K from the previous data point, then allow the apparatus to come to equilibrium for about one hour. Upon returning, the SQUID loop would be fired (normally three to four times) using the heater built into the SQUID circuitry to ensure that each data run had the same flux to voltage transfer ratio. The data collection program would be started and after approximately one minute the experimentalist would manually change the resistance setting of the GRT by the equivalent of a 3 – 10 mK temperature change (10 to 100 ohms, depending on the temperature). The SQUID output would approach its asymptotic value approximately half an hour later and the data run would be terminated. Data taken during the quiet hours of the night with the experimentalist monitoring the data from another room by a second computer showed very low noise and very few transients due to acoustic activity in the building. A sample of a data run at 2.8 K is shown in the Figure 18. The reader should note that the upper line in the figure is the same data corrected for the automatic

reset of the SQUID circuit when the voltage output reaches 5 volts (there are two resets in this data set, for a total correction of 10 volts). For completeness, a sample of data taken during the working day with acoustic transients repeatedly present is also shown in Figure 19. The data was collected over a six day period with the majority coming in a step-wise sweep downward in temperature from 4.0 K to 1.7 K. Some data points were collected in the region below the Curie temperature when the sample was warmed and cooled between data points. These was no evidence of hysteresis in this film, even below the zero field T_c.

Data Analysis

The data took the form of a separate text file for each run. This file, created by the data acquisition program, included the time, GRT resistance, and SQUID output at one second intervals. Each file was imported into a separate sheet of a Microsoft EXCEL workbook and corrected for SQUID resets and obvious flux jumps due to acoustic transients. The majority of the data taken at night required no corrections other than the usual resets when the SQUID output reached the maximum value of 5 volts. To determine the total flux change in the pickup coil, the SQUID output was averaged for the time period before the incremental temperature change was keyed in and for the last minute or so of the data run. The difference between these two mean values was multiplied by the value of 5 flux quanta per volt (based on the range setting of the QD5000) and divided by the incremental temperature change. The temperature change

was calculated from the calibration polynomial provided by Lake Shore[48] with the GRT. In one case (3.3 K) a GPIB communications failure occurred, but the QD5000 continued to function and the final SQUID output value was recorded by hand. In another case (2.4 K) a worker dropped a piece of sheet metal in the shop and the resulting acoustic transient stopped data collection at about 1050 seconds. A correction of 0.16 volts was added to the final recorded value based on analysis of the previous temperature scan.

Results and Preliminary Conclusions

The entire data set is displayed in Figure 20. The fully analyzed data depicted on this graph is presented in tabular form in Appendix A. The curve shown in the figure should be understood as the temperature derivative of the magnetic susceptibility at a given ambient field. The temperature at which the peak occurs approximates the Curie temperature of the ferromagnetic sample. As can be seen from the figure the Curie temperature of our sample film was approximately 2.8 K. The full width at half maximum (FWHM) of the susceptibility curve is approximately 1.2 K. By comparison of these results with the work of Klemme, et al[39], we can draw some further conclusions. Klemme, et al, tested PdMn samples with 0.75% and 0.90% Mn in Pd. The Curie temperature of the 0.90% sample was reported as 2.75 K. From this we infer that our sample has a concentration of manganese of approximately 0.90%, although it was sputtered from a target that contained 0.68% manganese. Second, Klemme, et al tested their 0.90% sample at trapped fields ranging from 12.5 to 50 gauss. The FWHM of their

50 gauss test was approximately 1.2 K. From this we initially inferred that the average magnetic field at the position of our sample, although obviously not uniform, was approximately 50 gauss. Subsequent data presented in Chapters 4 through 7 show that the variation in width of the transition is not consistent between the bulk and film measurements, and indeed among the film measurements for different thicknesses and geometries. Klemme, et al's test of the 0.90% sample with a field of 50 gauss gave a peak sensitivity of 1.6 flux quanta per microkelvin. This is consistent with our result of 26 flux quanta per millikelvin when the difference in filling fraction (the fraction of the pickup coil volume filled with PdMn) is factored in. The data from this experiment is presented in Figure 21, normalized to the peak value of the 0.90% Mn, 50 Gauss test of Klemme, et al. The factor used to normalize the data was 1.18. Other contributions could be signal broadening that might be removed by annealing the film, the non uniform magnetic field at our sample, and the fact that our sample was on the very edge of the volume enclosed by the pickup coil. We can conclude, finally, that the sputtering process yielded an ordered film that displays the same ferromagnetic properties as the bulk samples tested by Klemme, et al. In addition, our film did not require annealing at high temperature to ensure a uniform distribution of the manganese throughout the palladium matrix. This is important because it means that such films can be sputtered on a variety of substrates, including very thin substrates, and used as high resolution thermometers without additional difficult post deposition materials processing.

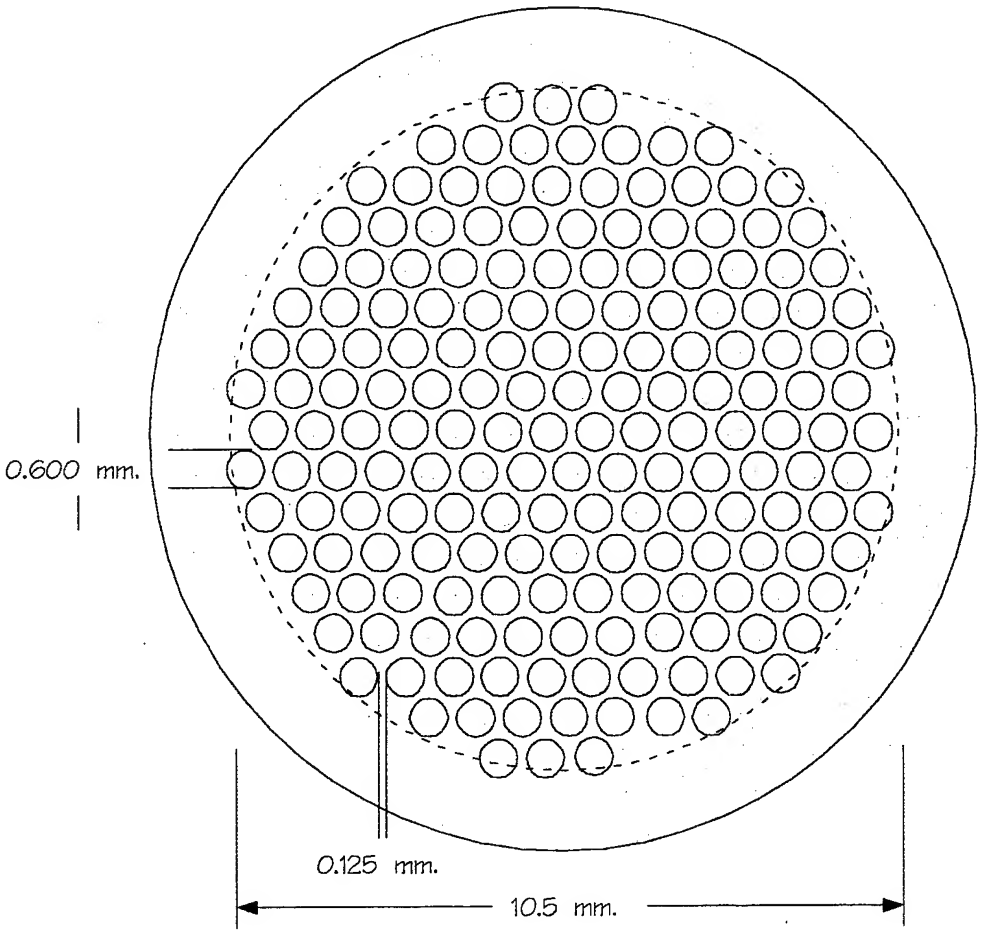

Figure 14: Design drawing for thermometer substrate

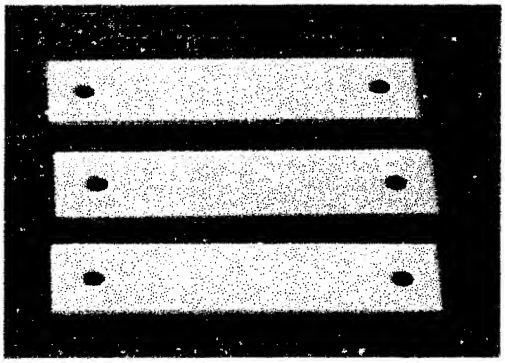

Figure 15: PdMn Samples for Magnetic Susceptibility Testing

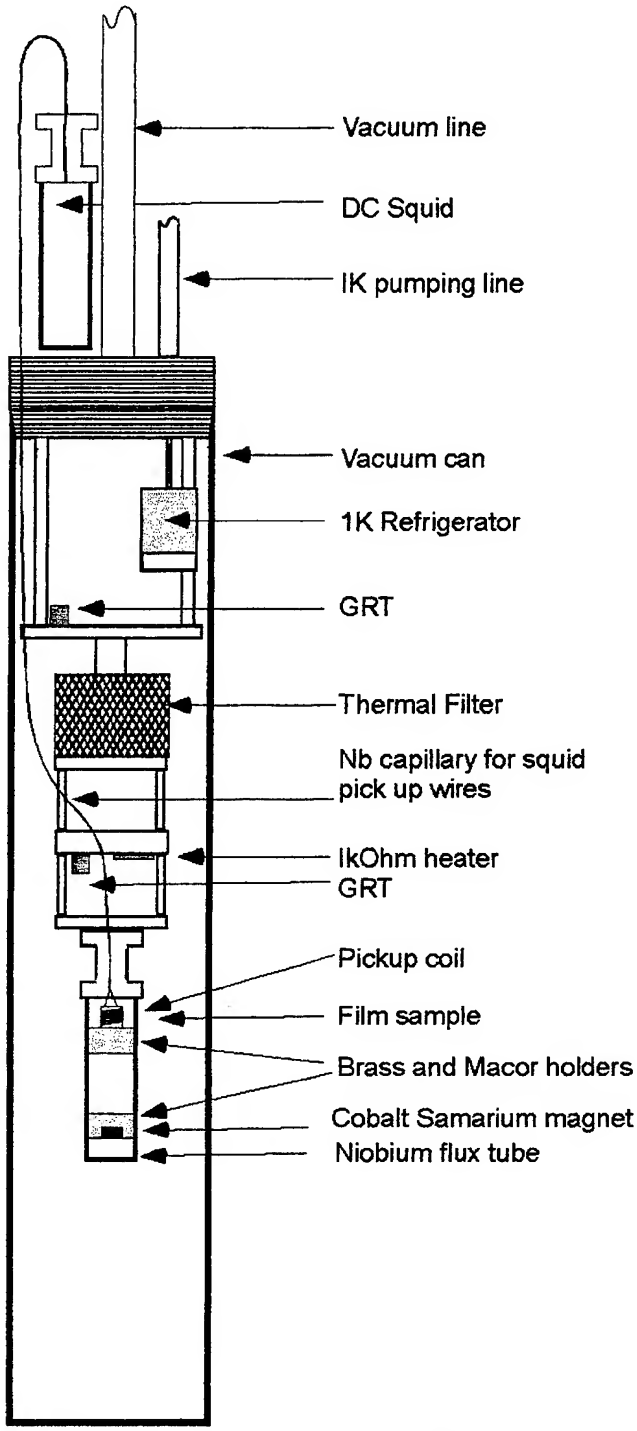

Figure 16: Low temperature cryostat used for susceptibility testing.

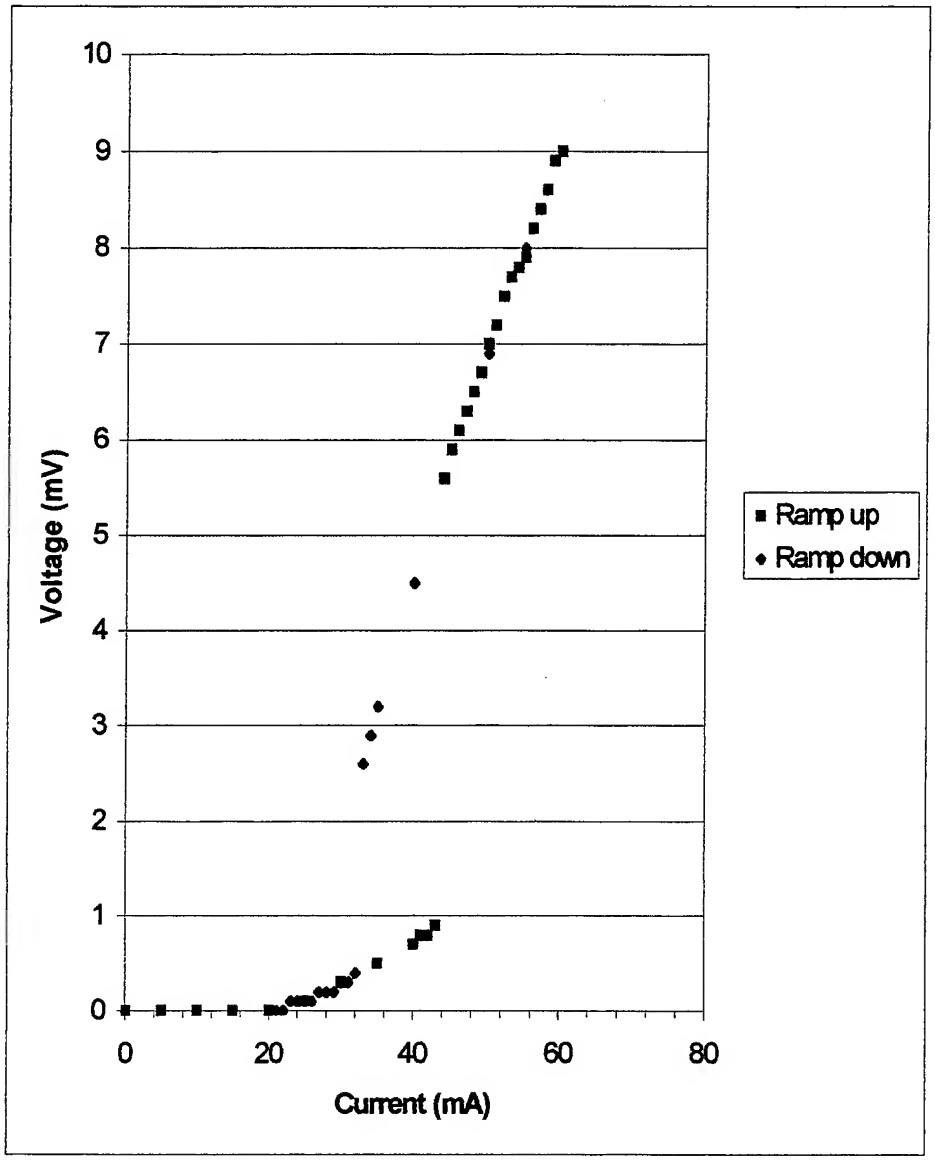

Figure 17: I-V characteristic determined during superconducting joint test. The hysteresis in the curve probably due to some complex characteristics of the wire, but is not important for our purposes.

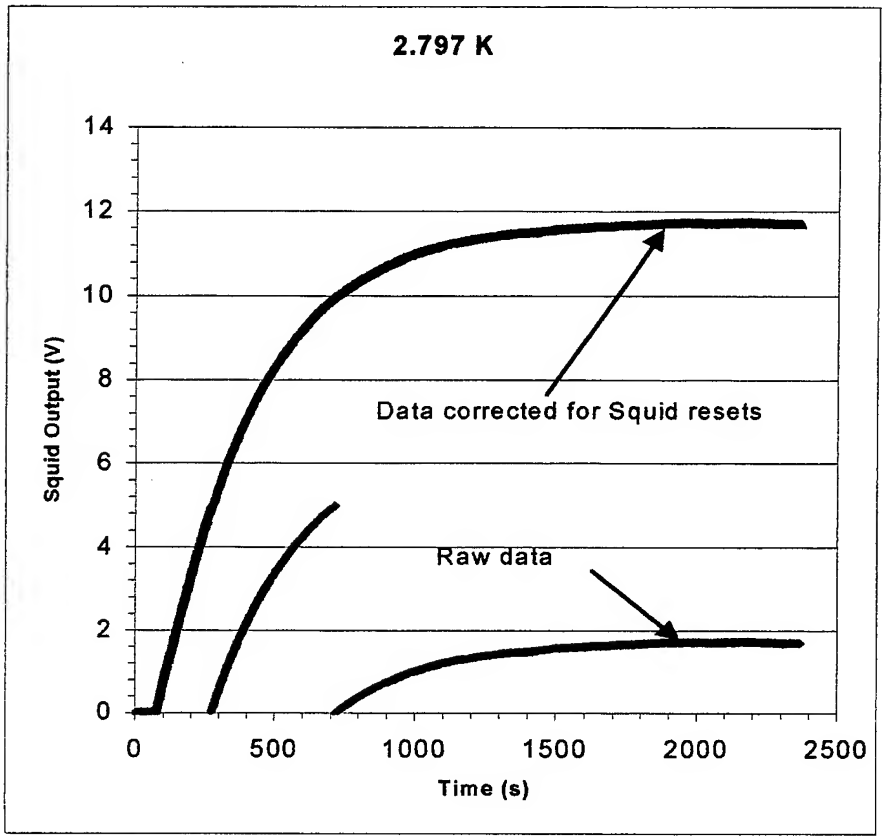

Figure 18: Data collected for a temperature change of 4.5 mK at 2.8 K using the permanent cobalt samarium magnet. The raw and corrected data coincide prior to about 290 seconds.

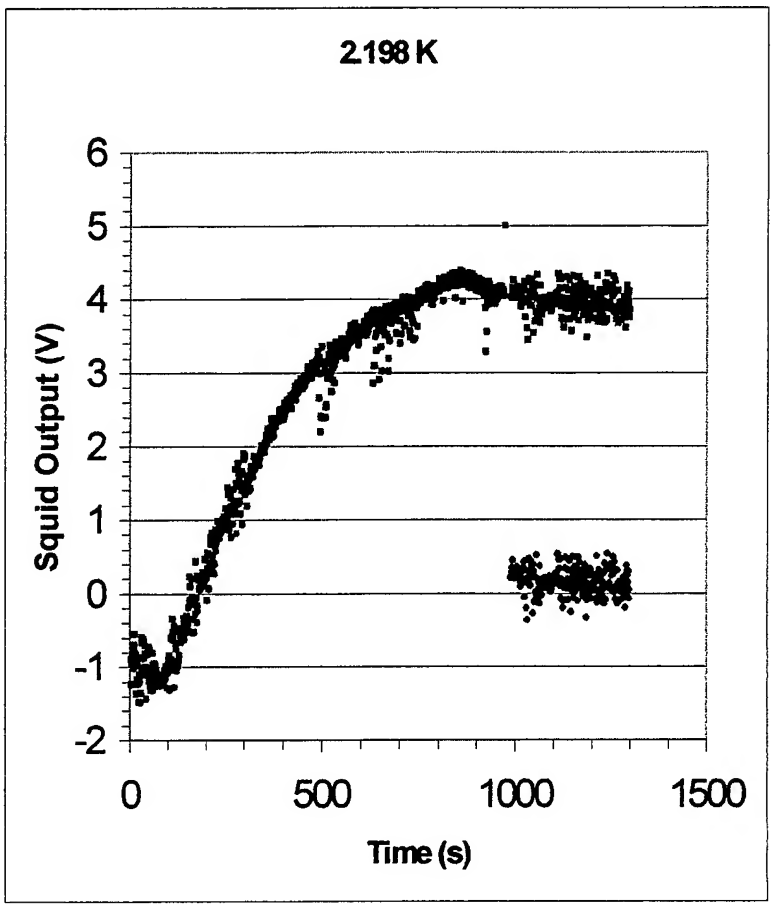

Figure 19: Data collected for a temperature change of 2.7 mK at 2.2K using the permanent cobalt samarium magnet. This data was taken during the day, when acoustic transients greatly complicated data acquisition. The raw and corrected data coincide until about 950 seconds.

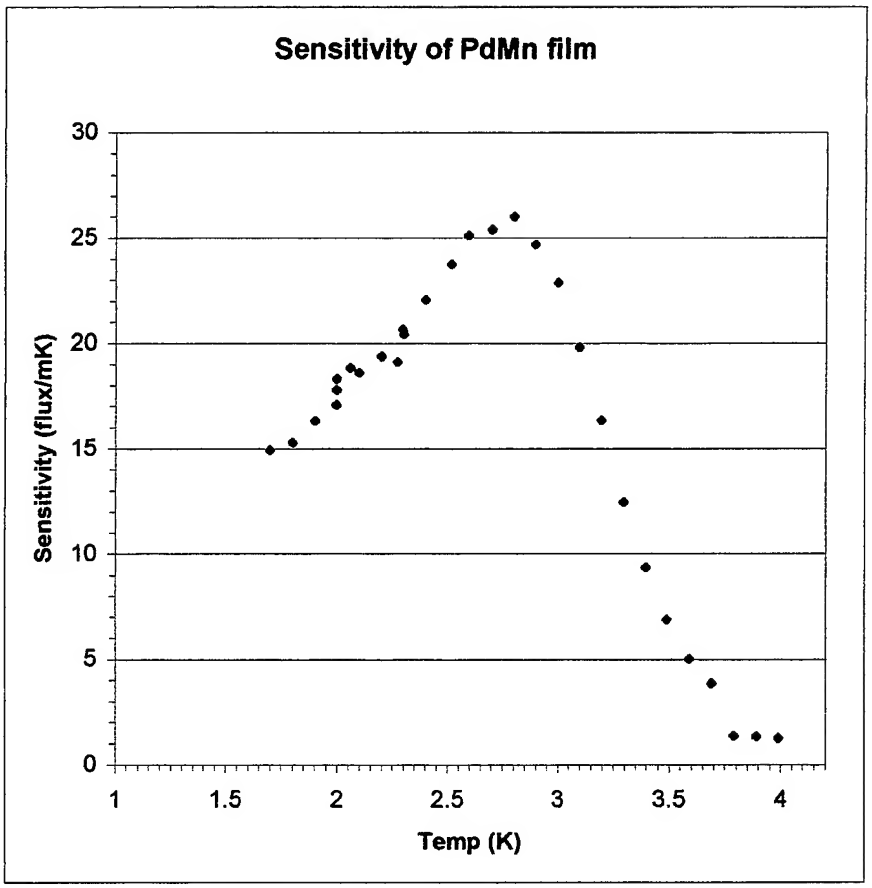

Figure 20: Sensitivity of 12.5 μm PdMn film using the permanent cobalt samarium magnet.

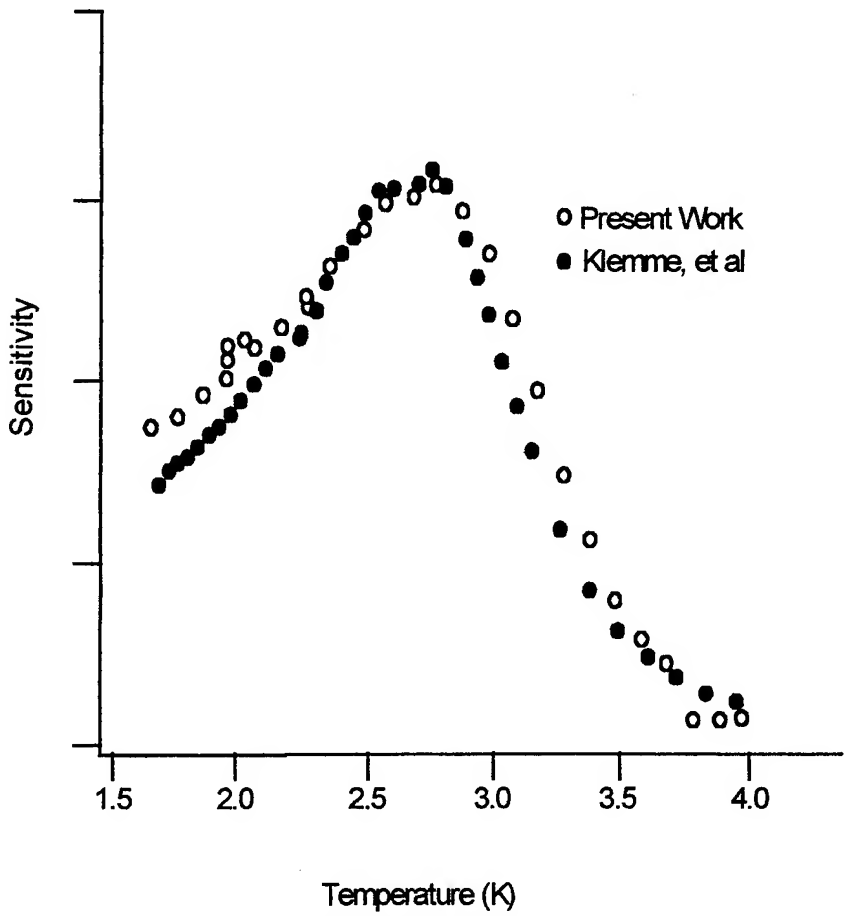

Figure 21: Sensitivity data from our 12.5 μm film, normalized to the peak value of the 0.90% Mn, 50 Gauss bulk test of Klemme, et al. The vertical axis has arbitrary units. This comparison lead us to infer that the average field at the sample location in our test was approximately 50 gauss.

Chapter Four: Continued work on PdMn thin films

Experimental Objectives

The results of the initial test of the thin film PdMn geometry were considered sufficiently promising to order the sputtering of the film onto the perforated substrates. However, since the magnetic field was unknown and peak sensitivity occurred at a temperature considerably above 2.2K, we elected to further explore the properties of the film. The planned series of experiments included 1) testing of a similar sample using a known variable field, 2) testing of samples 1 micron and 10 microns thick with the field perpendicular to the sample surface, 3) annealing of one of the films tested in step 2 with subsequent sensitivity measurements for the annealed film, and 4) testing of a bulk sample cut from the sputtering target after it is no longer useful for its original purpose.

Experiment Design and Preparation

The first series of experiments required some modifications to the cryostat and the experimental conditions. The first step was to move the experiment into an area of the building without a basement to minimize the acoustic noise picked up by the SQUID loop. Second, the experimental sample had to be mounted in a superconducting flux tube so that an external electromagnet could provide a known field. The magnet had been used in previous work and was calibrated to produce 90 gauss per ampere. It used 1000 turns of pure niobium wire and was made to fit on the outside of the same vacuum can used

previously. The modifications to the sample stage can be seen in the photograph at Figure 22. Some of the modifications were designed to improve the thermal response of the system. The copper wicking epoxied to the sample surface is also attached to the same stage as the heater to provide a much faster thermal link between the two. The brass and Macor[65] sample holder was machined to fit inside a ¾" outside diameter, 0.065" wall niobium tube. To reduce its thermal mass the wall thickness of this tube was reduced to 0.035" over most of its length. To support the sample holder halfway up the inside the niobium tube a Teflon[44] tube was machined to fit inside the niobium and attached with screws at the bottom. This Teflon tube was also bored out to a thin wall over most of its length. The assembled apparatus is seen schematically in Figure 23. This apparatus was sealed in the vacuum can and the superconducting electromagnet slipped over the outside of the vacuum can.

Experimental Technique

We began by trapping a field of 12.5 gauss. Once the apparatus was cooled to liquid helium temperature, a secondary 5 kΩ heater was used to heat everything inside the vacuum can to above 10 K. The electromagnet was turned on and the apparatus was allowed to cool through the niobium superconductivity transition at 9.25 K. The power to the magnet was turned off at about 8 K, trapping the field inside the niobium flux tube. The same procedure was used for each subsequent field value.

We immediately saw that our efforts to provide a better thermal link to the sample from the heater stage were successful. A sample graph of GRT resistance and SQUID output is presented in Figure 24. This graph shows that the GRT and the sample respond at virtually the same time to a change induced by the heater current. This made the data analysis process both easier and more accurate than in the previous test. Lake Shore[48] provides an interpolation table with the derivative $\frac{dR}{dT}$ for temperatures at 0.1 K intervals in the region of interest. The derivative can also be calculated for any intermediate temperature using the calibration polynomial. The sensitivity is calculated by plotting the SQUID output vs. GRT resistance for a data run, determining the slope of the best fit line to the data by linear regression, and multiplying this slope by $\frac{dR}{dT}$ and by $\frac{d\Phi}{dV}$ (from the configuration parameters of the QD 5000 SQUID Controller). The data shown in Figure 24 is presented again in Figure 25, with the trend line analysis shown on the figure. A full data run for a given magnetic field consisted of a step wise sweep from 4.0 K downward to 1.7 K. The efficiency of the 1 K refrigerator was inconsistent through the three weeks of the initial cooldown, resulting in some differences in the minimum temperature reached. The data for 12.5 gauss, the first field tested, along with the data from Chapter 3, are seen in Figure 26 and in Table 1 at Appendix B. As mentioned previously, the shape of this data closely matched the data taken with the permanent magnet, calling into question our earlier conclusion that the permanent magnet produced a field at the sample of approximately 50 gauss. This result is really not surprising, since the cause of the

broadening of the sensitivity curve with increasing field is magnetic saturation of the sample and this effect can be expected to vary with different sample geometries.

This discrepancy in the saturation induced behavior of our sample vs. the bulk data of Klemme, et al meant that we needed more complete data on our film. We therefore undertook to complete a systematic examination of the response of the film sample to a variety of field environments. We took data at fields ranging from 6 gauss to 250 gauss. These results are presented in Figures 27 and 28 and in Tables 2 and 3 in Appendix B.

Summarizing the features of this data set, we note first that the shift in peak sensitivity for this film, in this orientation to the magnetic field, is very small, around 0.2 K, and is fully evident between the 6 gauss and 12.5 gauss curves. At higher fields there is no further shift in the peak sensitivity. Second, the saturation of the sample with increasing field is evident from the broadening and flattening of the sensitivity curve as the field increases. If the magnetization is strong, then as the magnetic moments in the sample become increasingly aligned in the ambient field direction, a saturated condition can be reached before the sample reaches the Curie temperature. Even if the field is not strong enough to fully saturate the sample, this has the effect of reducing the peak sensitivity, flattening the curve, and even changing the shape of the data to the right of the peak from concave to convex. As can be seen from the figures, this change becomes evident above an applied field of 150 gauss.

Interpretation of Low Field Data

The data presented in Figure 29 for the 6 gauss field show the low field asymmetry expected for the ferromagnetic transition. For reduced temperatures, $t = \frac{T - T_c}{T_c}$, greater than zero, the critical exponent of the zero field susceptibility is γ, so that

$$\chi_T \propto t^{-\gamma}, t > 0$$

The exponent γ is expected to be 1 in the mean field theory, 1.5 in the Ginzburg-Landau theory and 1.4 in the Renormalization Group (RG) theory for a 3 dimensional Heisenberg ferromagnet.[66,67] Since our graph is the derivative of the magnetization at a small but finite field, closely related to the susceptibility at zero field, we would expect the exponent of our data to be approximately, but not necessarily exactly, $-(\gamma+1)$. As seen in Figure 30, a best fit power law curve gives an exponent of –2.52. This exponent can only be considered an approximate solution since it depends on how much data close to $t = 0$ one chooses to include. Ideally, one would want about 10 data points per decade in the region close to the transition, but such a measurement is not possible in this present apparatus. For $t < 0$, there are competing factors, including domain relaxation, that round off the peak of the sensitivity curve. Nonetheless, the shape of the data depicted in Figure 30 can be taken as support for the theoretical low field behavior.

Hysteresis and Other Features

In the initial run of data at 6 gauss, there was a dip in the sensitivity just to the low temperature side of the peak. This data was taken in two passes, one from 2.8 K downward to 1.7 K, and a second from 2.9 K upward to 4 K. The data is presented in Figure 31 and in Table 4 in Appendix B. The fact that the two sets of data didn't match precisely at the peak caused some concern about the possibility of hysteresis effects below the zero field T_c value. To search for such effects complete scans were conducted downward from 4.0 K to 1.7 K then back to 4.0 K at both 35 gauss and 6 gauss. The results are presented in Figures 31 and 32 and in Tables 5 and 6 in Appendix B. Although there is no evidence of hysteresis throughout the temperature range, the data did show an interesting feature at 2.1K.

In both the 6 and 35 gauss data sets there is a dip that occurs in the sensitivity as the temperature passes through 2.1 K on the way down. As the temperature is ramped back up this feature is not seen again. Although there are other data points that do not match exactly, the largest difference is seen at this temperature. The difference between the sensitivity at 2.1 K between the two measurements is 3.9% for the 6 gauss field and 5.8% for the 35 gauss field. The dip was actually noticed when the data for the 70 and 150 gauss fields was charted later and it can be seen in both data sets. Because of this it was decided to look for the dip again in the data taken at 250 gauss. It appeared in the initial pass through the temperature range of interest. These data points were recorded in the order 1.9 K, 2.0 K, 2.3 K, 2.2 K, 2.1 K, 2.4 K, then increasing from there to 4.0 K.

Additional data points were recorded at 2.3 K, 2.2 K, and 2.1 K after the first sweep was completed. This time the dip appeared at 2.3 K and gives a 4.6% difference in sensitivity between the two measurements at that temperature. Because the dip wasn't discovered until the data at 70 and 150 gauss was analyzed and because the data taken at those field values consisted of only a single downward sweep in each case, the best we can do is compare the sensitivity at 2.1 K with the value obtained from the best fit line through the low temperature side of the data. We calculated the equations of best fit lines through the data below 2.8 K excluding the points at 2.1 K, obtaining R^2 values of 0.9996 and 0.9936. The parameter R^2 is used to evaluate the closeness of fit in a linear regression performed using Microsoft EXCEL. According to the EXCEL help documentation R^2 is the square of the "Pearson product moment correlation coefficient, a dimensionless index that ranges from -1.0 to 1.0 inclusive and reflects the extent of a linear relationship between two data sets. R^2 can be interpreted as the portion of the variance in Y attributable to the variance in X."[68] The 70 and 150 gauss data points at 2.1 K fell 2.7% and 2.8% below the values on these regression lines. The data and the linear regression result at a field of 70 gauss are displayed in Figure 33.

To look for more evidence of a systematic effect that might explain these observations we conducted sweeps at values of magnetic field of 30, 50, 70, 90, and 110 gauss using temperature intervals of approximately 0.025 K between 1.8 and 2.5 K. The data taken at 30 gauss is presented in Figures 34 and 35. These data show a dip at 2.05 K, but no further resolution of any shape associated with the feature. At higher values of the

magnetic field, the data were noisier and it proved impossible to draw any conclusions from this effort. It might be worthwhile to pursue this feature of the data at some future point, but to do so would likely require immersing the film in a liquid helium cell to attain much finer control over the sample temperature and lower noise.

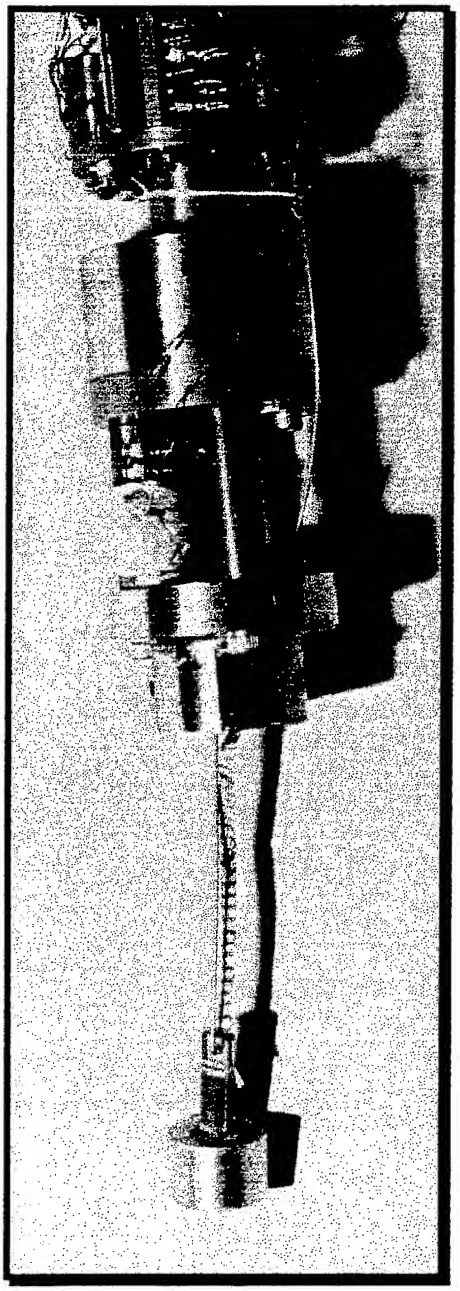

Figure 22: Sample and sample holder for susceptibility testing in a variable magnetic field. The sample is potted into a Macor[65] cup inside the brass ring.

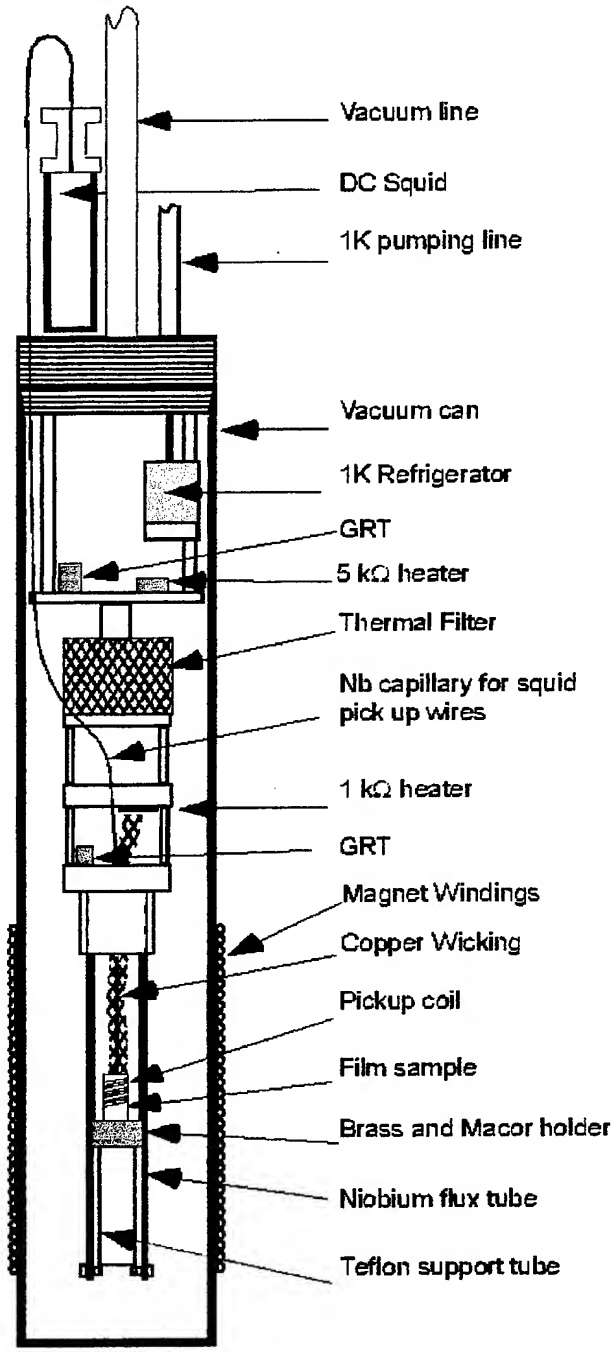

Figure 23: Assembled apparatus for variable field sensitivity measurements. The niobium flux tube is fixed to the GRT stage with two set screws. The screws at the bottom of the flux tube fix a Teflon[44] tube that supports the sample in the center of the flux tube.

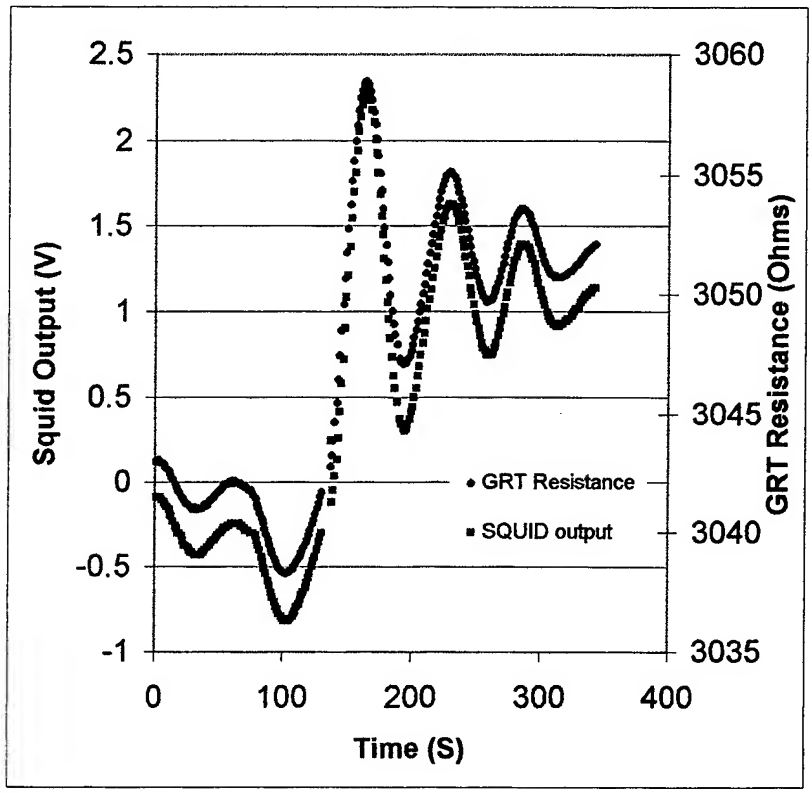

Figure 24: Data taken with a field of 35 gauss at 3.0 K. The chart shows the near simultaneous response of the GRT and the PdMn film sample.

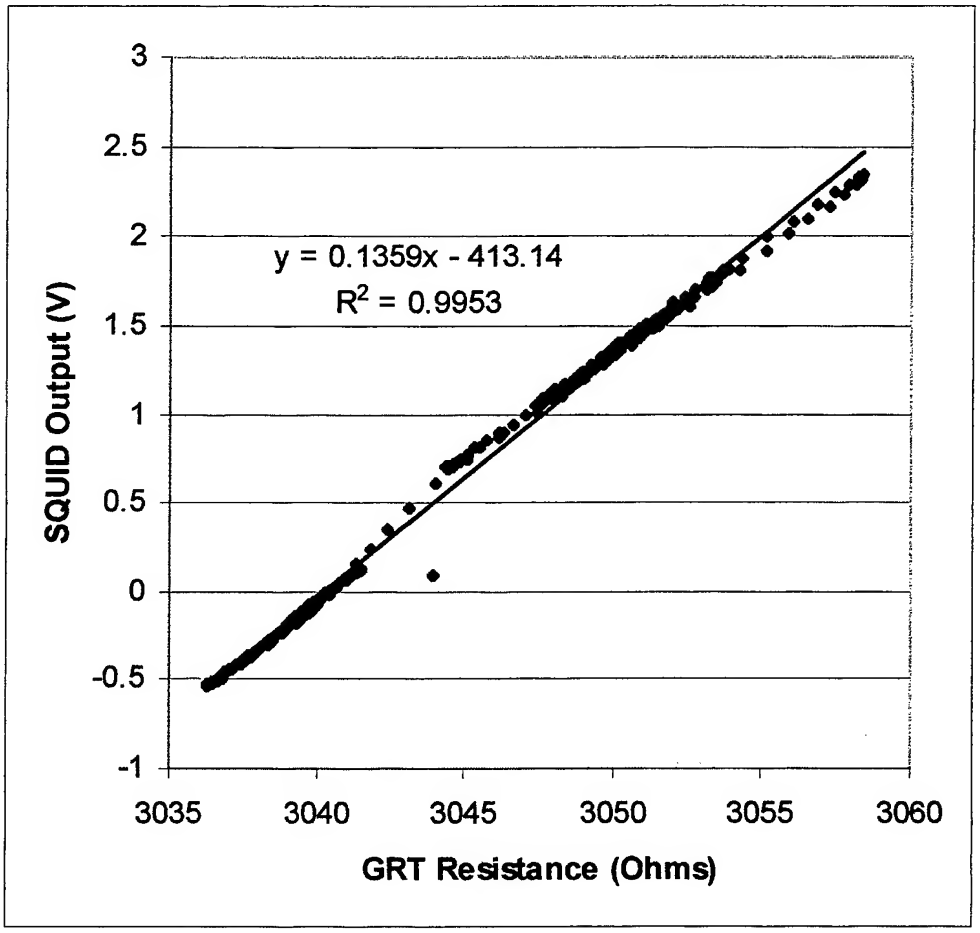

Figure 25: SQUID Output vs. GRT Resistance (temperature) for the data presented in Figure 24. The equation of the best fit line is shown on the graph. The points that appear off of the line are from the time immediately around the step change in temperature at about 130 seconds in Figure 23.

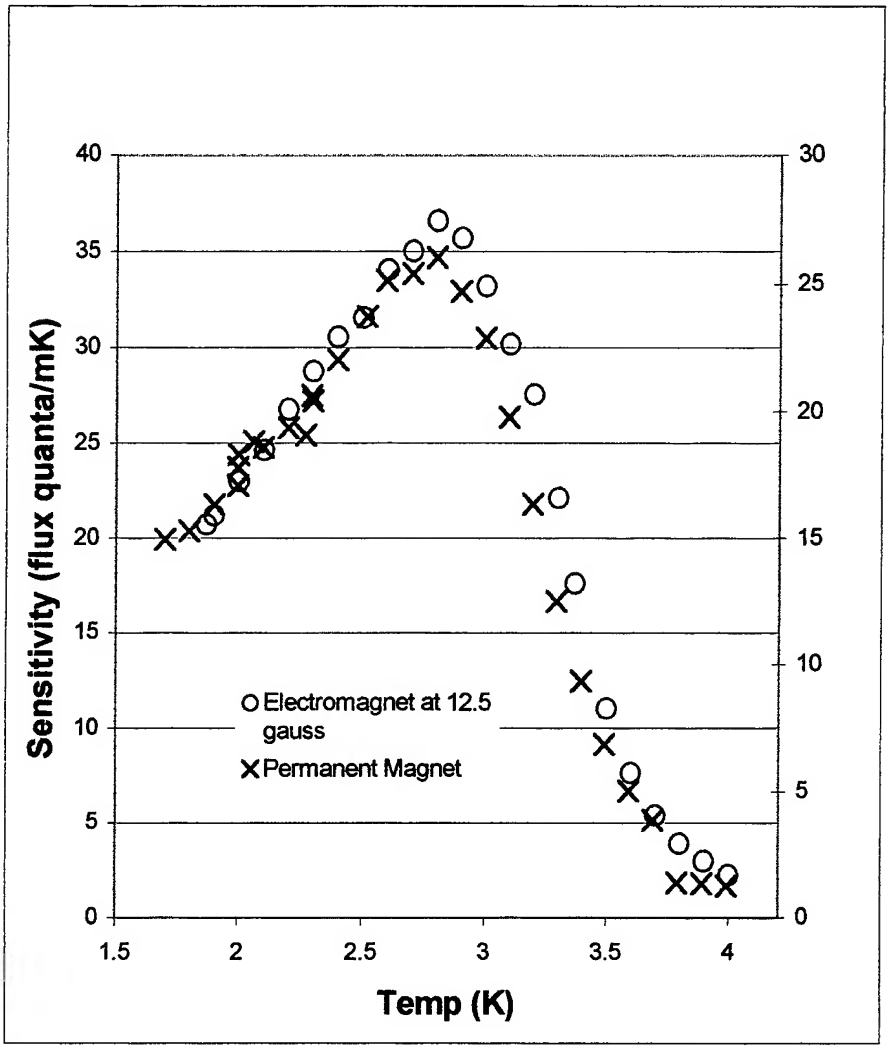

Figure 26: Data from the work discussed in Chapter three (film thickness = 12.5 μm, permanent magnet with field parallel to film) plotted with the data from the 12.5 gauss measurements with the electromagnet. The scale on the right is for the previous data, but the reader should be aware that the sample sizes and pickup loops were different. The similarity in shape is what is significant.

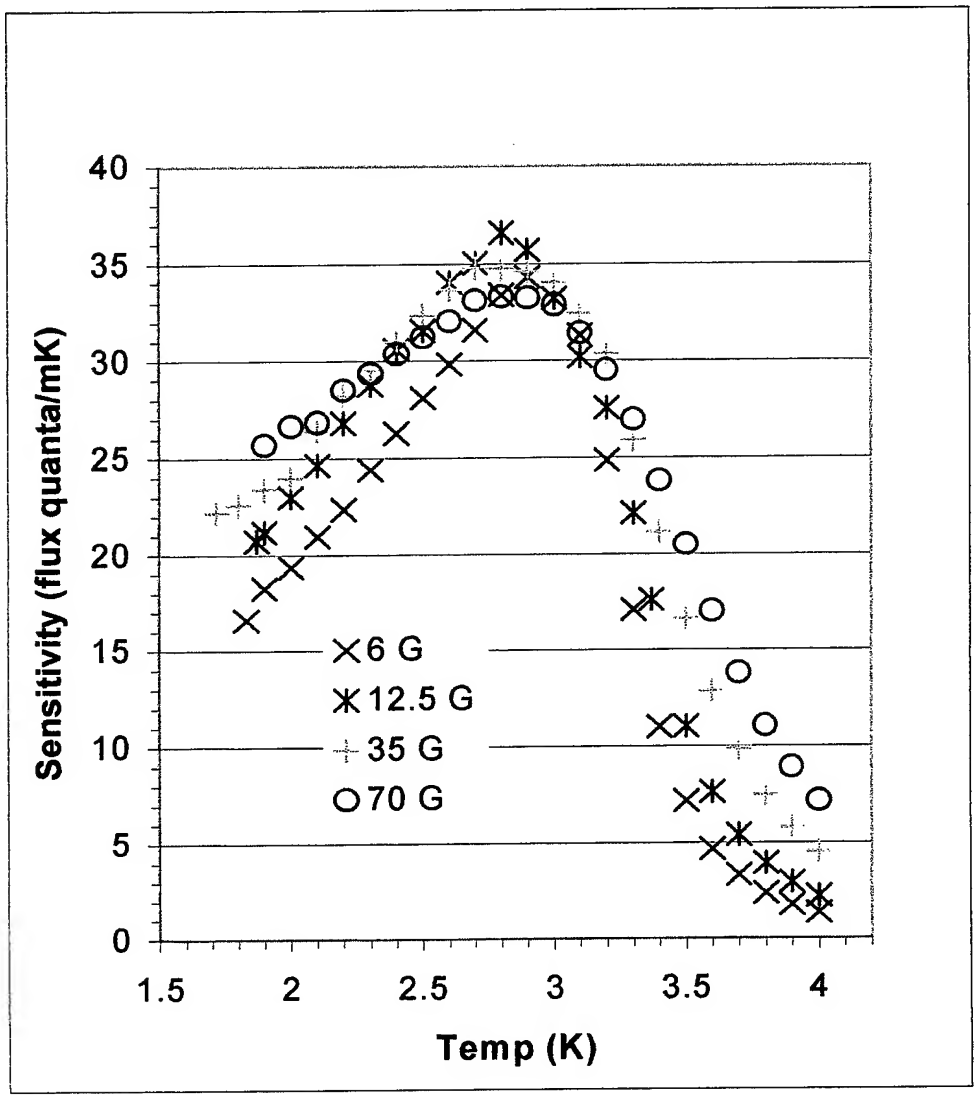

Figure 27: Sensitivity data for the 12.5 μm thick PdMn film sample, taken with magnetic fields ranging from 6 gauss to 70 gauss oriented parallel with the film surface.

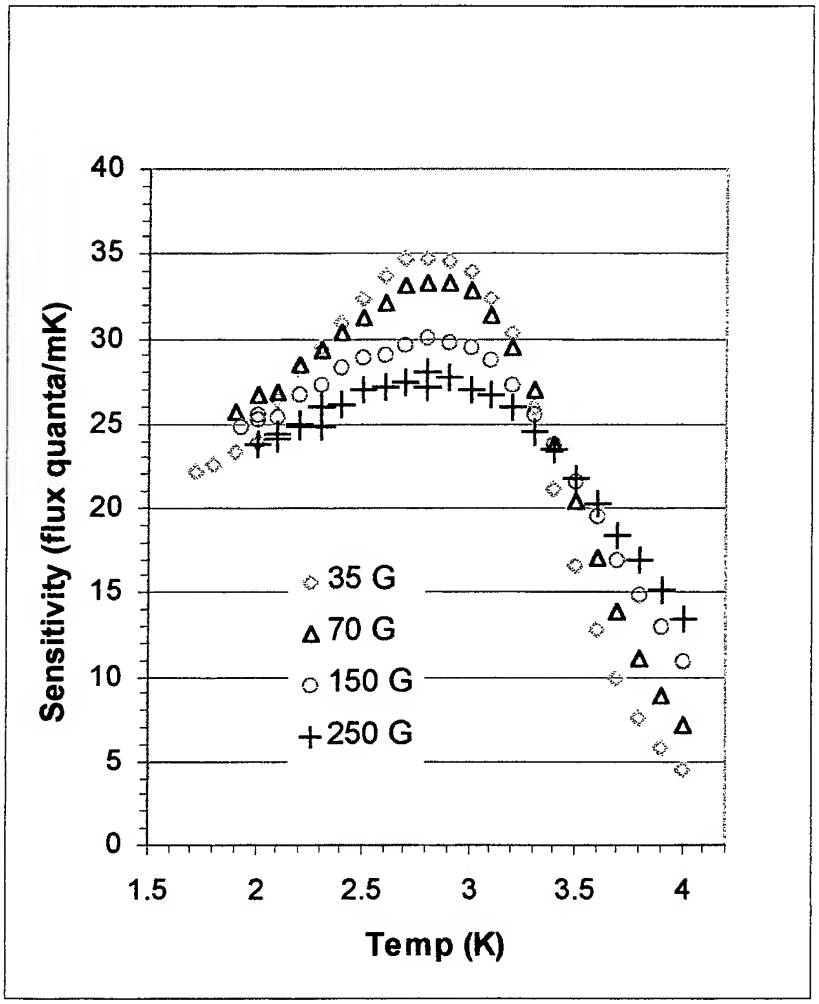

Figure 28: Sensitivity data for the 12.5 μm PdMn film sample, taken with magnetic fields ranging from 35 gauss to 250 gauss, oriented parallel to the film surface. The 35 and 70 gauss data is the same as in Figure 27.

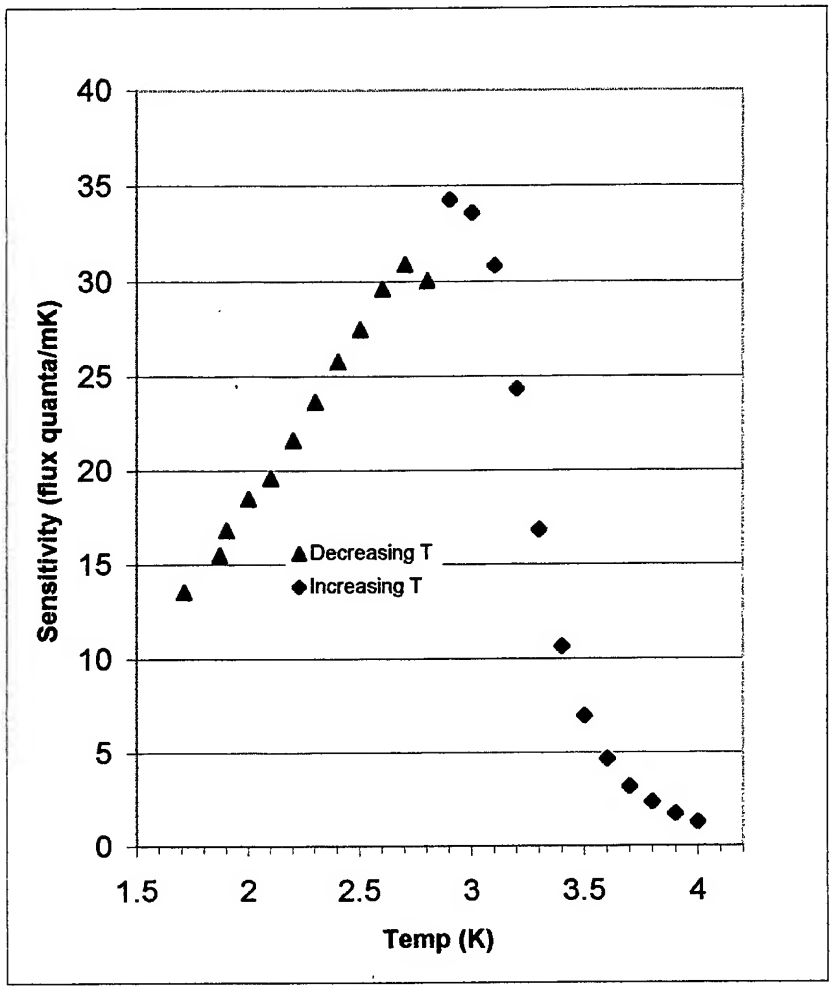

Figure 29: First data taken at 6 gauss. The anamolous data point at 2.8 K prompted a systematic search for hysteresis effects. The data was taken in two passes with an overnight break. As seen in Figures 31 and 32, no conclusive hysteresis was found.

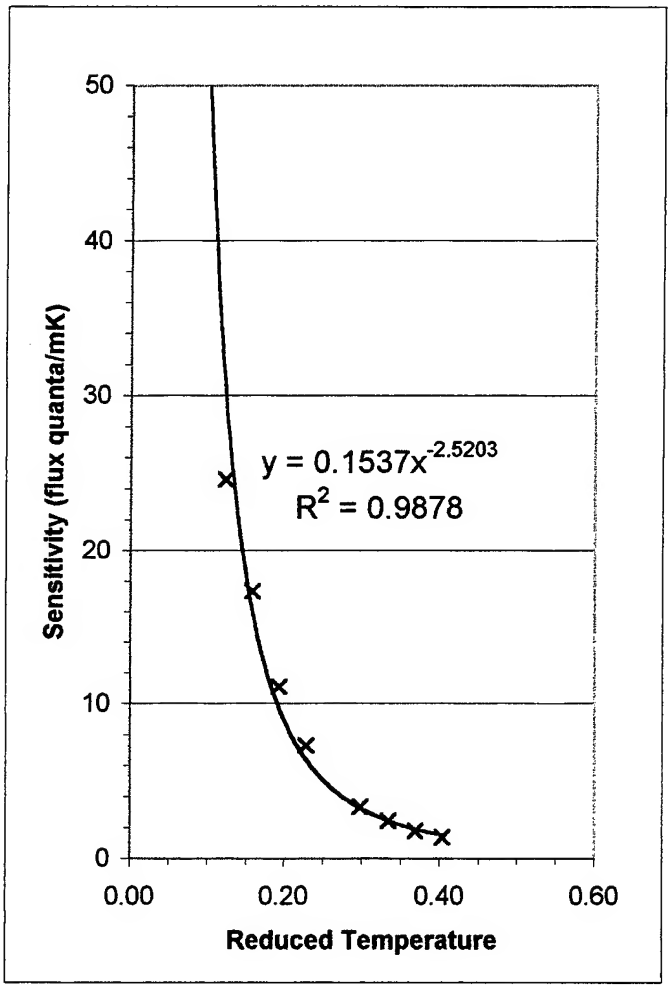

Figure 30: Data from Figure 31, plotted versus reduced temperature $t = \frac{T - T_c}{T_c}$, for $t > 0$, with a best fit power law curve. The exponent is an estimate of $-(\gamma+1)$. The RG value for γ in the case of a Heisenberg ferromagnet is 1.4.

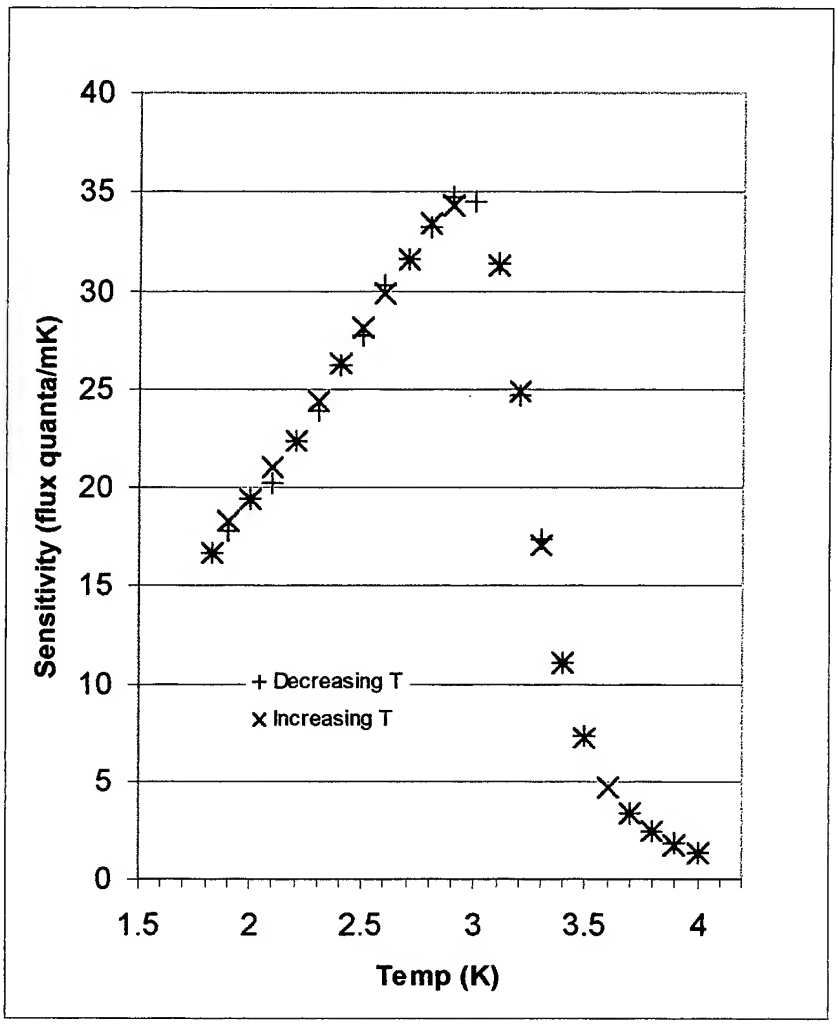

Figure 31: Results of consecutive temperature sweeps at a field of 6 gauss, looking for hysteresis effects. The difference between the two measurements at 2.1 K is 3.9%.

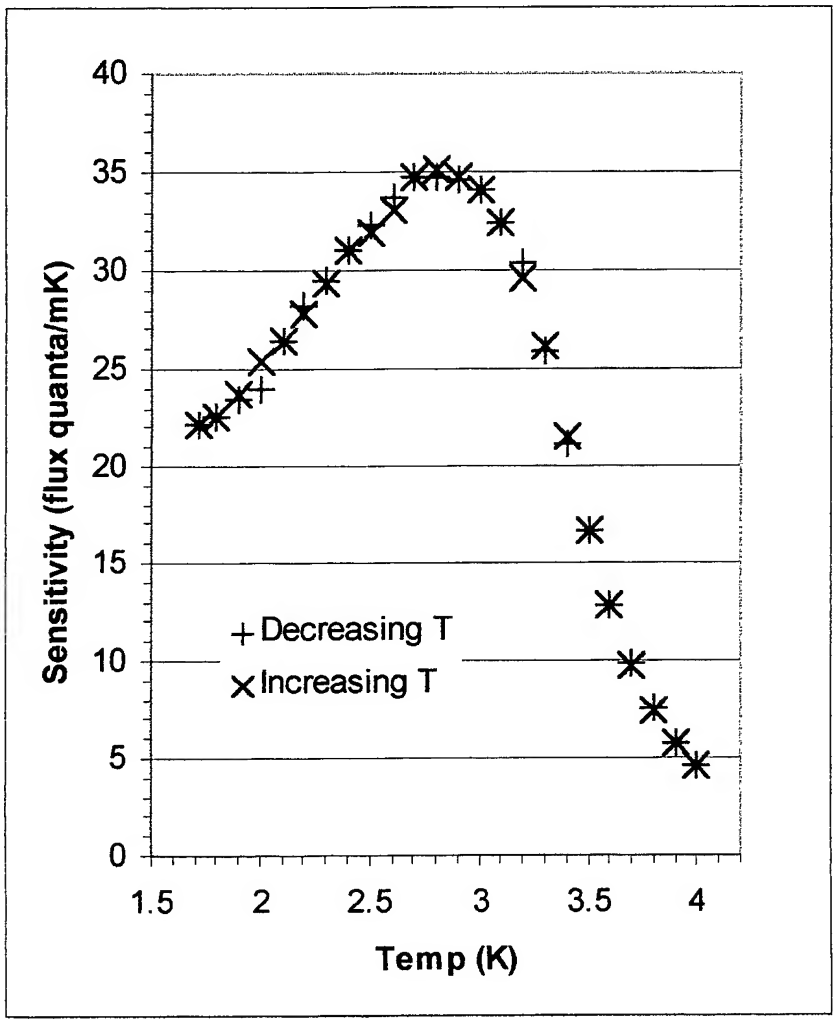

Figure 32: Results of consecutive temperature sweeps at a field of 35 gauss, looking for hysteresis effects. The difference between the two measurements at 2.1 K is 5.8%.

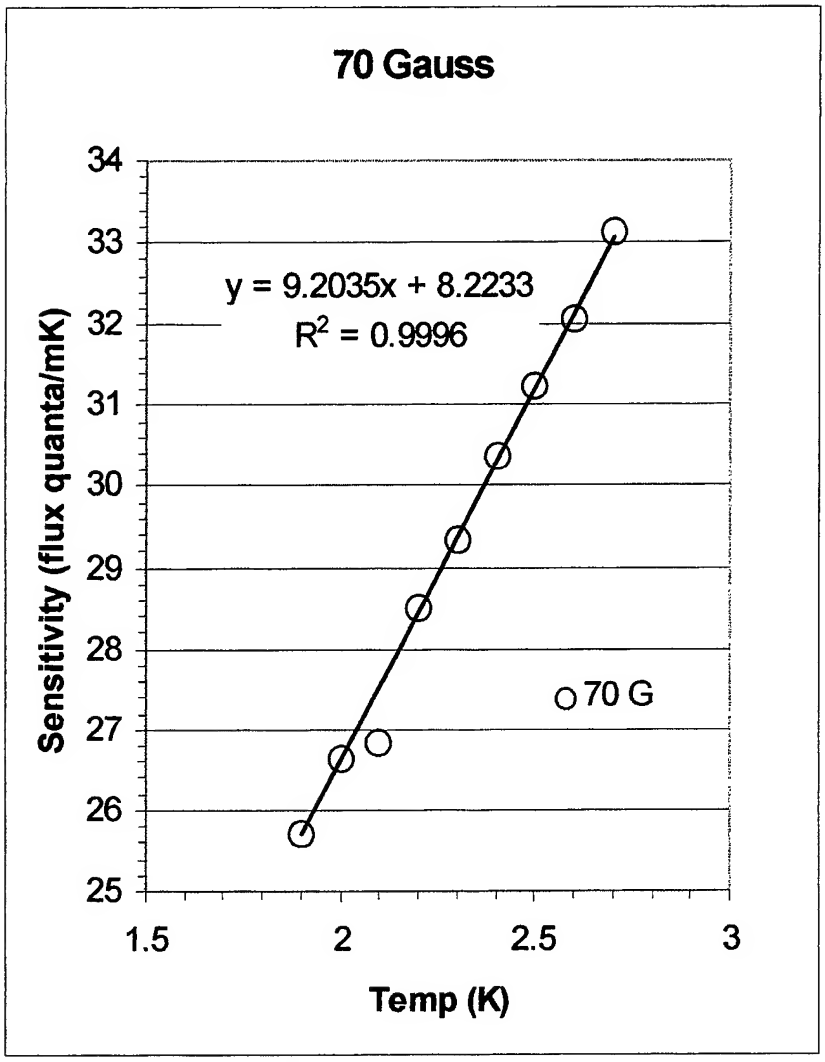

Figure 33: Data taken with a field of 70 gauss below 2.8 K with the best fit line through the data excluding the point at 2.1 K. The point at 2.1 K is 2.7% below the line.

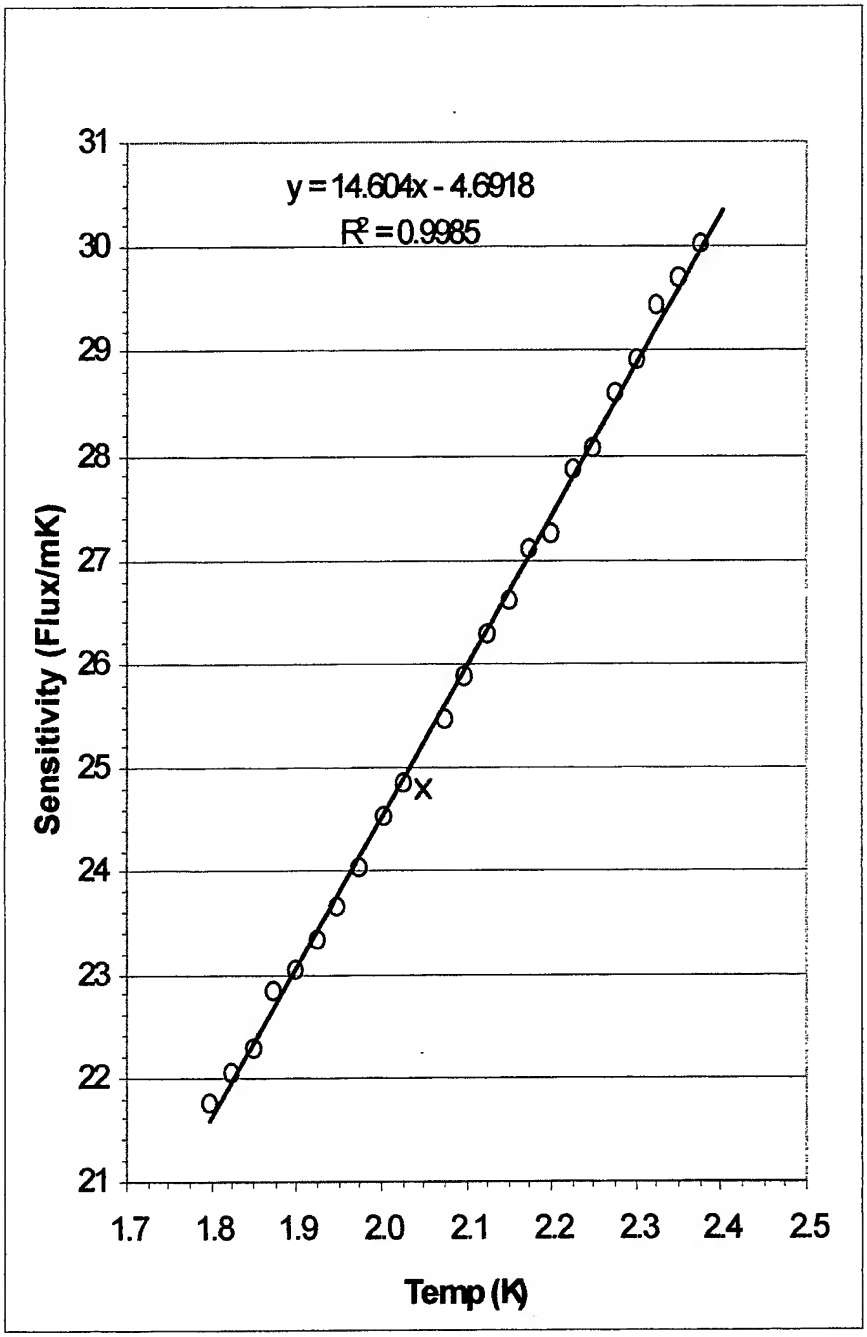

Figure 34: Data taken at intervals of approximately 0.025 K searching for the dip that appears at approximately 2.050 K. The equation of the best fit line and the R^2 value are shown on the graph. The data point shown in red is omitted from the linear regression analysis.

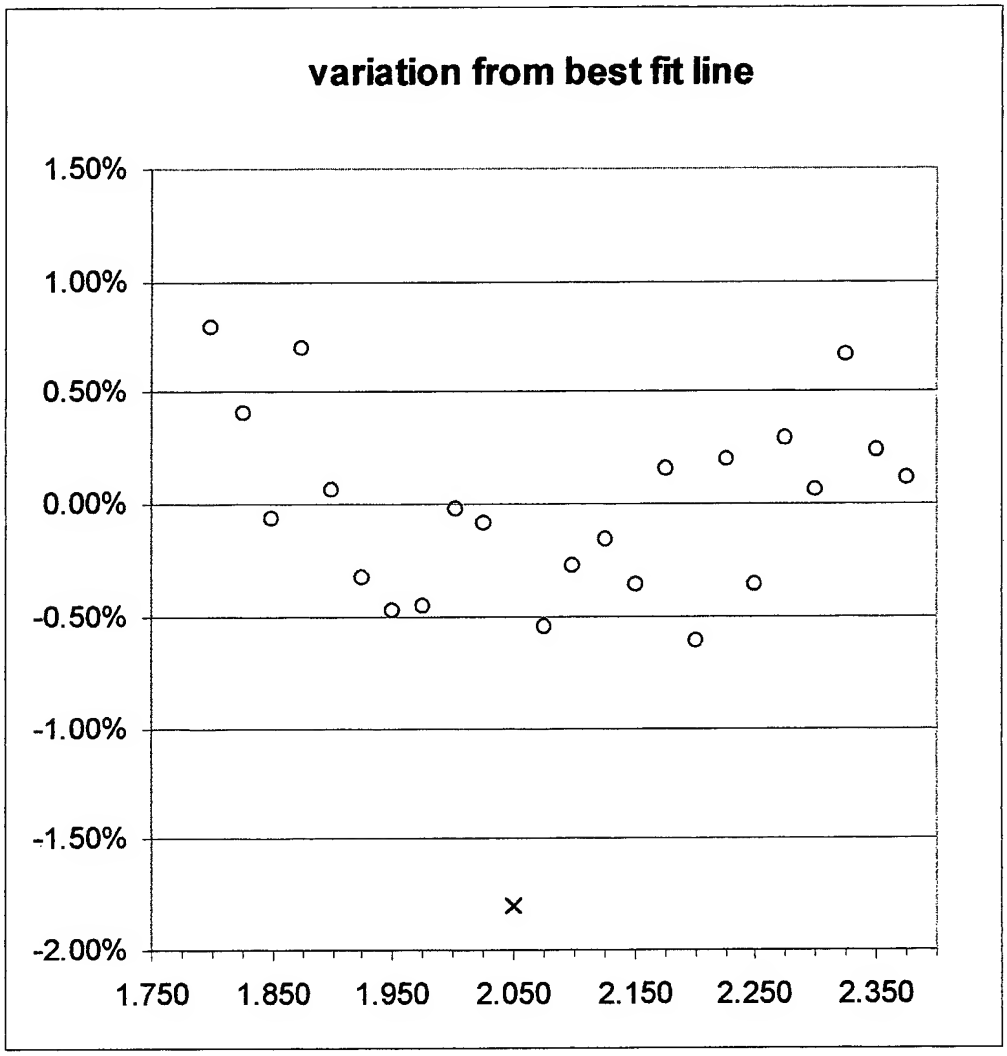

Figure 35: The data of Figure 34 plotted using the percentage difference between the recorded value and the value of the best fit line at the same temperature. The data point shown in red is omitted from the linear regression analysis in Figure 34.

Chapter Five – Thinner Films

At about the same time we completed the search for systematic effects discussed in the previous chapter, we obtained new samples from Sandia National Laboratories. This set consisted of four fused silica disks 0.5 inches in diameter with a nominal coating of 1.0 μm of PdMn (measured value 0.94 μm). Two of the disks were 1/16" thick and two were 1/8" thick.

1 Micron Film – Sample Perpendicular to Field

Since we were anxious to test the concept of a thin film thermometer with the magnetic field perpendicular to the film surface, we began this new series of experiments by mounting a sample in this configuration. We made an annular Teflon[44] holder with a step machined into the inner diameter to receive the sample and a groove machined around the outer diameter for the winding of the SQUID pickup coil. This Teflon piece was mated to a brass ring intended to hold the sample in the niobium flux tube through differential thermal contraction. The sample mount is displayed in Figure 36. Once again, we epoxied a piece of copper braid to the back side of the sample to provide good thermal contact between the heater stage and the sample. We tested this sample at only two values of magnetic field, 35 and 12.5 gauss, because the results were fairly disappointing. The data for the 12.5 gauss field are depicted in Figure 37. The sensitivity is very low to start with and shows a marked drop at 3.6 K. This is consistent with the data taken at 35 gauss, as is the noise level that can be seen in the plot. While it

is tempting to speculate that some deficiency in the apparatus might have resulted in this disappointing data, the shape of the raw data (SQUID voltage and GRT resistance vs. time) is consistent with that presented in Figures 24 and 25. This conclusion was born out by the initial series of measurements on the next sample, as is explained below.

Demagnetization

The explanation for the data depicted in Figure 37 lies in a phenomenon that was not unexpected with a very thin film in this orientation. The requirement that the normal components of the magnetic induction, $\vec{B}$, and the tangential components of the magnetic field, $\vec{H}$, be continuous across the interface between the vacuum space and the film sample lead to a spontaneous demagnetization of the sample when the ambient field is perpendicular to the sample's surface.[69] While the tangential components of $\vec{H}$ are essentially zero both inside and outside the sample, the requirement that $\vec{B}$ be contin uous through the surface perpendicular to the field means that no magnetization can occur in the region close to the surface. In the geometry used previously, with the field parallel to the sample surface, the condition on the surface is that H_t is continuous so that $H_{in} = H_{out}$. In this case, $B_{in} = \mu H_{in}$, and B gets large as χ, and therefore μ, diverges at T_c. However, in the present orientation with the field perpendicular to the sample surface, the condition in effect is that the normal component of B is continuous, meaning that $B_{in} = B_{out}$, and therefore $\mu = 1$ for all T. Now, since $\mu = 1 + 4\pi\chi$, and $\chi_T \propto t^{-\nu}$, as mentioned earlier, the boundary condition restriction on μ overwhelms the expected

divergence in χ, and the sample is unable to magnetize. Unfortunately, in this orientation, with a very thin sample, this requirement effects most of the available magnetic material. With the sample oriented parallel to the field, this problem effects only the tiny fraction of the sample represented by the thin edges at the top and bottom of the sample. We have, in the two configurations, essentially the best and the worst possible conditions. While this result was not unexpected, it was hoped that using a thicker sample and greatly increasing the surface area that is parallel to the field by perforating the sample would raise the sensitivity to manageable levels.

1 Micron Film – Sample Parallel to Field

A second thin film sample was mounted with the sample surface parallel to the magnetic field. This sample was mounted atop a brass annulus with slots machined in its top to receive the edge of the fused silica disk. The SQUID pickup coil was wound directly around the sample and the copper braid and pickup loop were permanently epoxied to the sample. The sample configuration is displayed in Figure 38. The initial test, while not yielding any data, was very informative because it demonstrates what happens when the SQUID pickup loop is not persistently superconducting. Figures 39 and 40 demonstrate the telltale indication of this deficiency. As can be seen in Figure 39, there is a time lag between the response of the GRT and the response of the SQUID. While a poor thermal contact between the heater stage and the sample stage can result in a long time delay, this was not the case here. The phenomenon can be explained as the

effect of resistance in the SQUID loop. If a small resistance , R, exists in the loop, the the voltage, V, around the loop is $V = -\frac{d\Phi}{dt}$, and the SQUID loop current is $\frac{V}{R} = -\frac{1}{R}\frac{d\Phi}{dt}$. Therefore, when $R \neq 0$, the SQUID loop detects the derivative $\frac{d\Phi}{dt}$, not $\Phi(t)$, which it measures when the loop is superconducting. Zassenhaus and Reppy have even reported on the utility of this feature for some measurements.[69] Figure 41 displays the second feature. Here it can be seen that as the GRT records the temperature change, the SQUID, while it oscillates at the same rate as the GRT, returns to its original output value. It appears to respond to the change in the magnetic field rather than to the magnetic field itself. The source of this difficulty is in the preparation of the joints in the SQUID pickup loop, as described in Chapter 3.

After warming up the cryostat and reconnecting the superconducting joints in the SQUID pickup loop, we took a series of measurements at magnetic fields of 35, 70, and 6 gauss. The features common to all of this data are striking and depicted in Figures 41 and 42. First, there is a marked field induced shift in the peak sensitivity. The 6 gauss data peaks at about 2.7 K, while the 35 gauss data peaks at 3.0 K and the 70 gauss data peaks at 3.2 K. This is an expected effect, as can be seen by referring back to the data from Chapter 4, but it is larger here than it was for the thicker film. Second, the data is very repeatable on the paramagnetic side of the peak and very noisy on the ferromagnetic side. Data was taken for both increasing and decreasing temperatures at each value of the field, and results similar to those depicted in Figure 42 were observed at each value.

It is easy to speculate that the noise here is due to finite size domain effects that become quenched in thicker films. Alternatively, this increased noise may be associated with a magnetic domain structure that is incommensurate with the substrate. Regardless of the source, it is apparent that very thin films should only be used in thermometry applications above T_c. The third feature of the data that distinguishes it from the thicker film data is the shape of the curve on the paramagnetic side of the transition. Even at the lowest field value the data is convex to the high temperature side. For the thicker film, this feature only appeared at the highest field values. For lower field values the data was concave in this direction, which is the shape expected from the theory, as depicted in Figure 30.

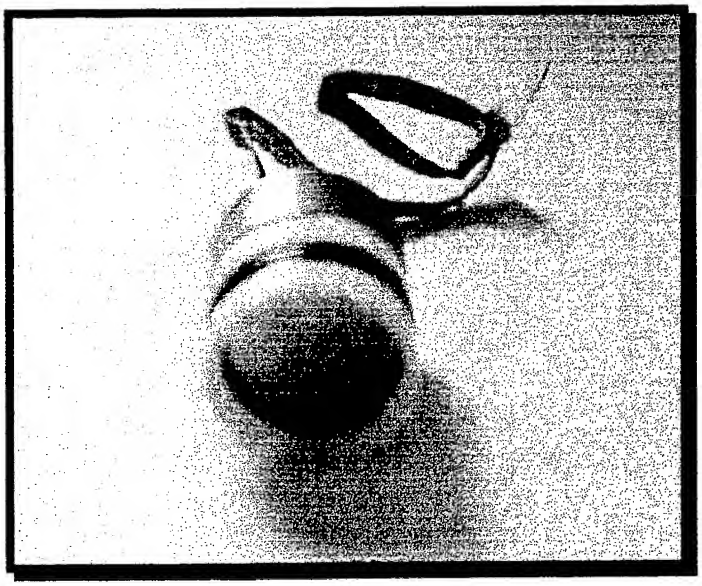

Figure 36: The sample holder for measuring the response of a 1μm thick film with the magnetic field perpendicular to the film surface. The superconducting pickup loop is seen wound on a groove in the Teflon[44] holder. The Teflon is mated to a brass piece to provide differential expansion so that the entire apparatus remains tightly held inside the niobium flux tube. The copper wicking is epoxied to the back of the sample to provide thermal contact with the heater stage.

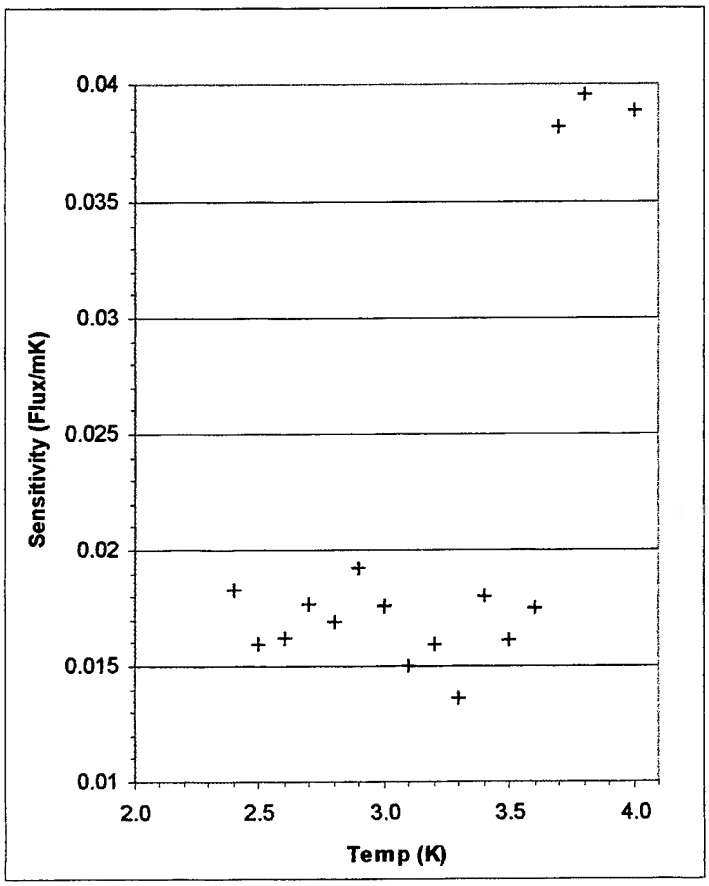

Figure 37: Data for a 0.94 μm thick sample with a field of 12.5 gauss perpendicular to the sample surface.

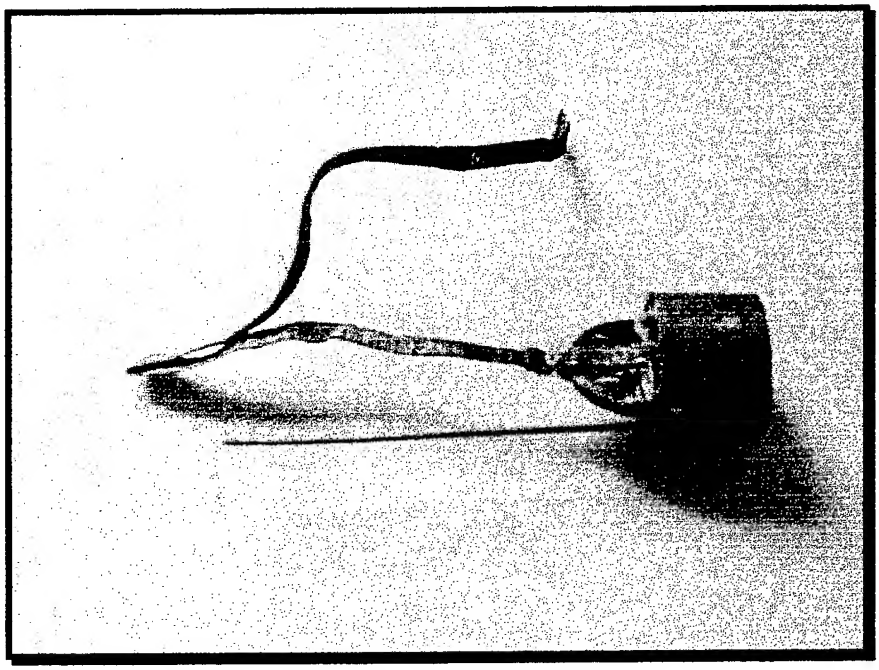

Figure 38: The sample holder for measuring the sensitivity of a 1 μm thick sample with the magnetic field parallel to the film surface. The pickup coil is wound directly on the sample.

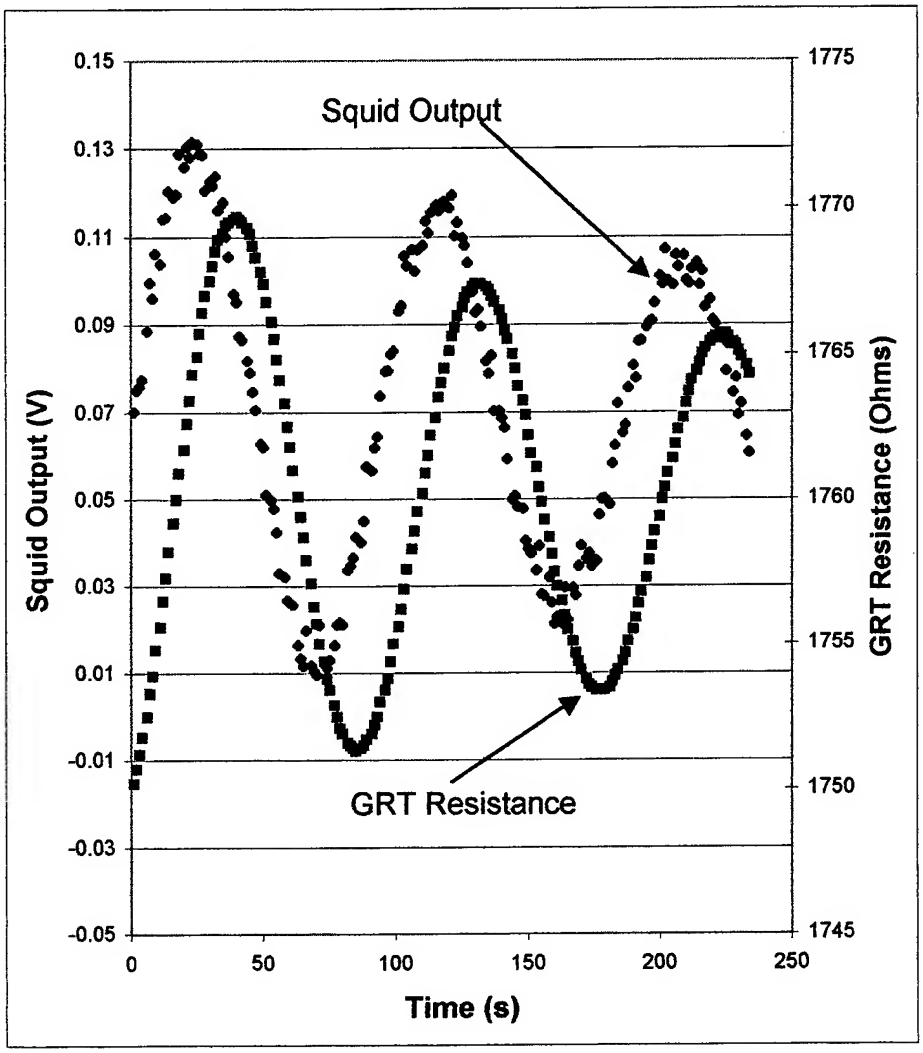

Figure 39: Raw data taken at 3.8 K with a magnetic field of 90 gauss, using the 0.94 μm thick sample with the field parallel to the sample surface. The time lag between the GRT resistance and the SQUID output indicate that the pickup loop is resistive.

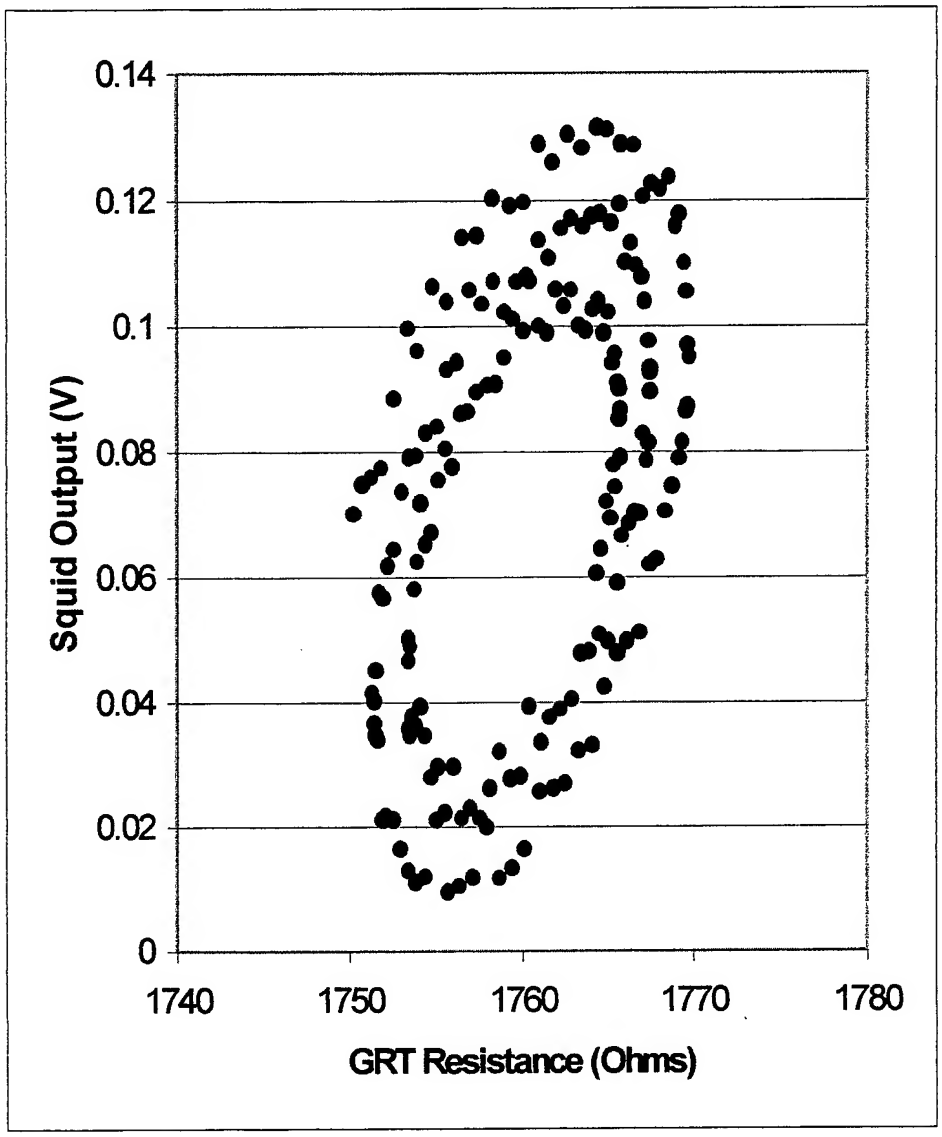

Figure 40: Data from Figure 39, with SQUID output plotted against the GRT Resistance. Normally, this graph would present a straight line, deviating only at the time a temperature change is initiated.

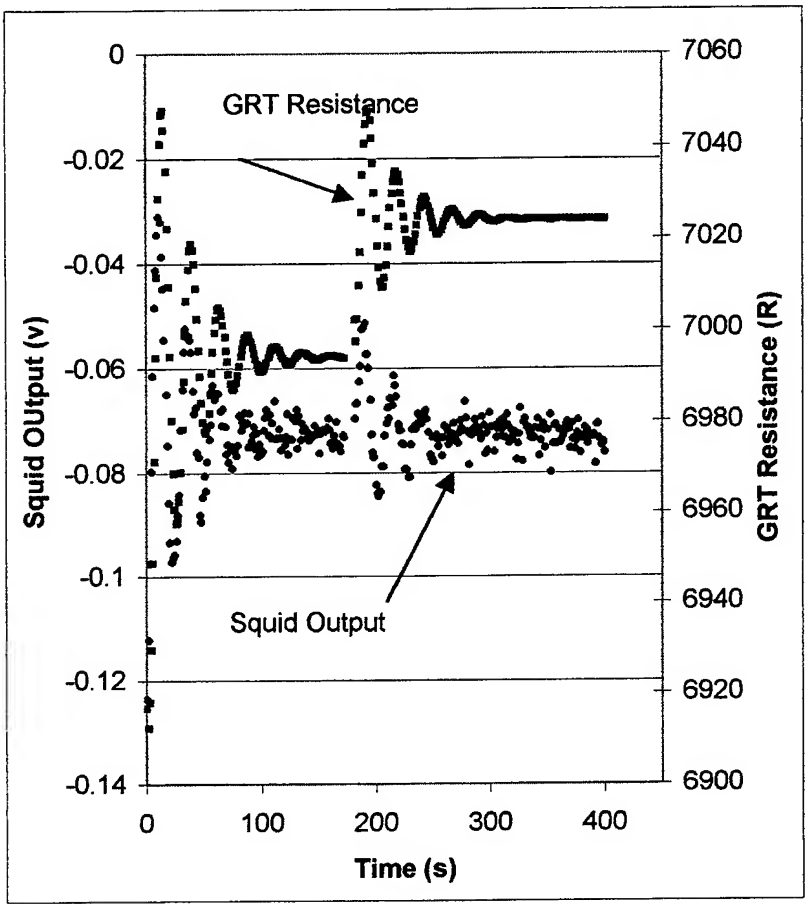

Figure 41: Raw data taken at 2.2 K from the same series as the data in Figure 39. This graph displays the second characteristic of a non persistent SQUID loop: the GRT shows the change in temperature, but the SQUID returns to its initial output after responding to the change in the magnetic field. This results from the lack of a persistent current when the SQUID loop is normal.

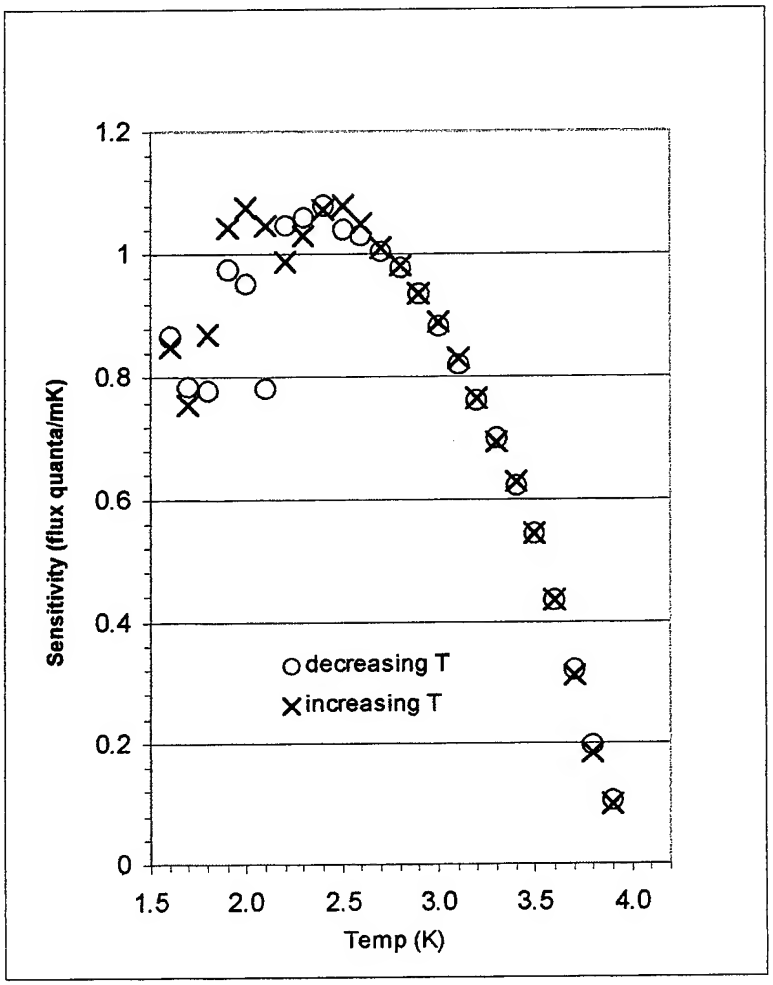

Figure 42: Data taken at a magnetic field of 6 gauss for the 0.94 μm thick film oriented with the film surface parallel to the magnetic field. The features of this data are discussed in the text. The pickup look is superconducting for the data in this figure and the data in Figure 43.

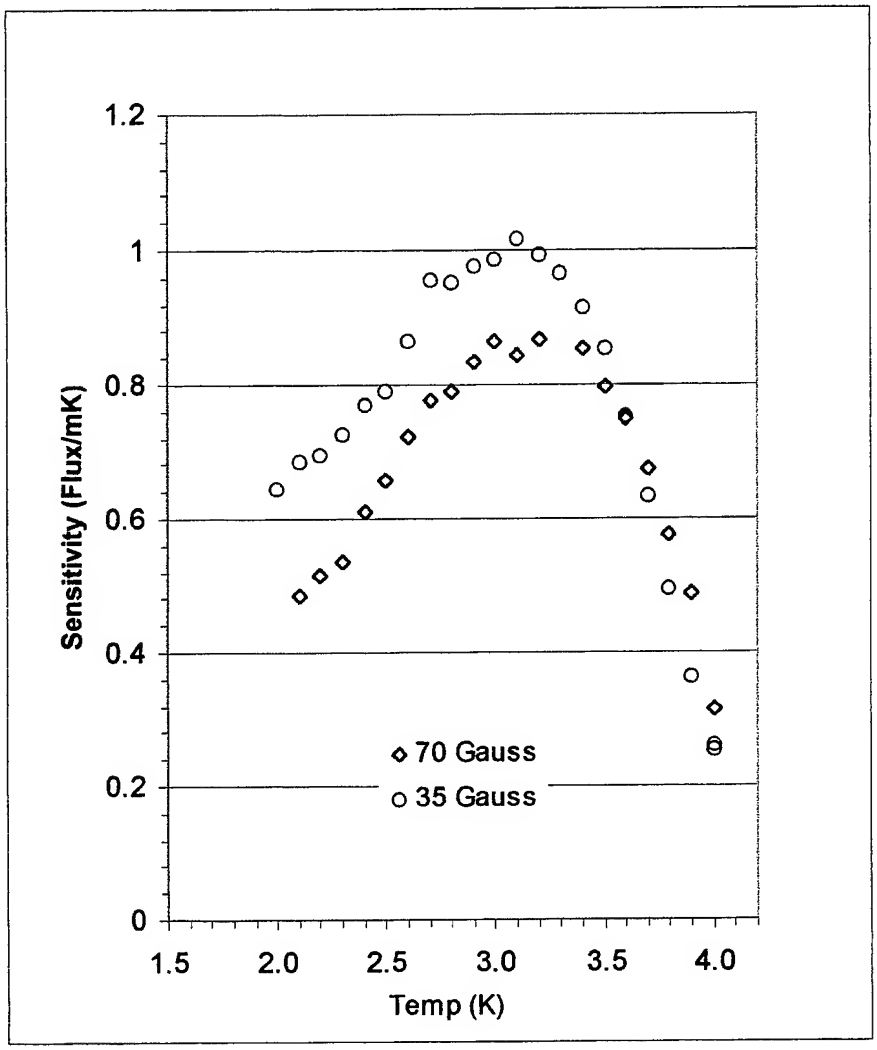

Figure 43: Data taken at 35 and 70 gauss for the same sample as in Figure 39, showing the shift in the peak sensitivity versus earlier tests and versus the 6 gauss data depicted in Figure 39.

Chapter Six – PdMn Screen Testing

Our experience with the 1 μm thick films allowed us to draw some very important conclusions concerning the planning for and conduct of the proposed thermal boundary measurements. The first was that full testing of the actual thermometer element would have to be completed before attempting thermal boundary measurements. Second, while we did not yet know whether the proposed geometry would work for a screen 10 μm thick, we knew it would probably not work for a 1 μm thick screen. Third, we knew that we would probably have to revisit the sputtering process to produce a screen with a T_c below 2.2 K. When the 1 μm samples were sputtered at Sandia National Laboratories, we also had the existing perforated disks of fused silica sputtered with a nominal coating of 10 μm.

Experiment Preparation

The results of this sputtering effort were only marginally satisfactory. There were two perforated disks sputtered to a thickness of 10 μm. They remained mounted with beeswax on the optical flat on which they were lapped to thickness. The PdMn coating was separated from the substrate at the edge of each disk, although it appeared to be adhering in the center. The disks were removed from the flat by heating on a hotplate to just above 373 K. We attempted to remove the wax residue from one disk by cleaning in an ultrasonic bath, resulting in the complete removal of the film from the substrate. We preserved the film for possible future use and cleaned the second disk by soaking it in

ethyl alcohol for a few hours. This procedure successfully removed the wax residue without removing the film from the substrate. We then made a ring of Vespel[45] to clamp the screen into the Vespel holder that had been previously manufactured for the thermal boundary measurement apparatus. This holder is depicted at Figure 44. The screen was mounted and secured in place with this ring, which was epoxied to the annular holder with Tra-Bond 2115 epoxy.[46] The inside diameter of the niobium flux tube was reduced over half of its length to accommodate this holder. This made a shelf to support the screen and holder, thus eliminating the need for the hollow Teflon[44] support tube used in the previous experiments.

Initial Cooldown

When the apparatus was initially cooled down, the SQUID would not tune. After the usual series of troubleshooting procedures, we warmed up the cryostat to inspect the superconducting joints. It had previously been determined that a reliable test for the continuity of these joints existed. I had found that if repeated measurements of the SQUID pickup loop resistance (typically around 130 ohms at room temperature) using a digital multimeter connected across the SQUID terminals, produced consistent readings within 1 ohm, the pickup loop could be expected to function properly when cold. If these measurements varied by a few percent, then the loop frequently displayed non persistent behavior. This test showed no problem in this case, but the procedure of opening the cryostat afforded an opportunity to examine the screen after thermal cycling to 2 K. The

screen was slightly torn and it appeared as if the substrate had completely disintegrated, leaving the screen alone mounted to the holder. We decided to make another attempt to measure the response of the screen, despite this delicate condition. Previously, a copper strap had been loosely stuck to the back of the substrate with conductive grease to improve the thermal contact between the screen and the heater stage. At this point, however, we decided that it was more important to protect the sample screen than to get data quickly, so the cryostat was closed again with the full knowledge that we would be facing a long time constant for our measurements, as we did in the very first series of measurements reported on in Chapter Three.

Data Collection

On closing the cryostat again and cooling down, we found the same problem with the SQUID. It was eventually narrowed down to the SQUID preamplifier and cable, which was replaced. We then began collecting and analyzing data using the procedures discussed in Chapter Three. We collected data at 6, 35, and 70 gauss. The data at 6 gauss was very noisy, but displayed essentially the same features as that at 35 and 70 gauss. The data collected at 35 and 70 gauss is depicted in Figures 45 and 46. The data here peaks very sharply at 3.2 K, with virtually the same shape at each value of the magnetic field. We continued to increase the value of the magnetic field. The shape of the data remained consistent as we increased the field, showing none of the saturation induced broadening we saw with the rectangular film sample previously. The data for

values of the field up to 150 gauss is displayed in Figure 46, with the various curves normalized peak to peak.

The data for all field values up to 250 gauss is displayed in Figure 48. These data have some curious features. First, there is no apparent saturation effect evident from the shape of the data. Second, the peak sensitivity shifts to colder temperatures as the field increases, with a marked shift between 220 and 250 gauss. At 250 gauss, the peak is at 2.7 K, about the same as it was for the first samples sputtered from this target. This is a good indication that the sputtering yields of the two constituent elements remain fairly constant over repeated sputtering runs from the same target. Third, the demagnetization effect is not disabling for a perforated screen of this thickness. This screen contains approximately one third of the material of the rectangular samples. Counting the walls of the holes and the outer diameter, the screen has approximately 2% of the surface area oriented parallel to the ambient field, when compared to the rectangular sample. It fills approximately 30 times as much of the SQUID pickup loop. Taking these factors together, and disregarding demagnetization, one would expect about 20% of the sensitivity of the rectangular sample. Comparing the actual values of the peak sensitivity at 35 gauss from Figure 26 (for the rectangular sample with the field parallel to the surface) to the 35 gauss data for the screen with the field perpendicular to the surface in Figure 44, we find that the screen's sensitivity is 1% that of the rectangular sample. We can conclude that this means that, for a screen of these dimensions in this orientation, there is an approximate one order of magnitude loss of sensitivity due to the

demagnetization effect. It is easy to conclude from this data that a screen of this thickness is a viable thermometer, even in this orientation, but that it would be very desirable to produce one with a T_c below the Curie temperature of the sample. This, of course, means further refinement of the sputtering target composition and process. On a purely practical note, it should be noted here that further sputtering work has been postponed until the primary constituent palladium becomes more affordable. The price as this is being written is over $1000 per troy ounce, making sputtering targets roughly $8000 each. This compares with a per target price of $2700 when we procured the first sputtering target.

One other important technical conclusion can be drawn from this data. The disintegration of the substrate on the initial cooldown was disappointing, as was the separation of the film from the substrate during the sputtering process. The purpose of the fused silica substrate was twofold: to provide a surface for sputtering and to provide mechanical rigidity to avoid microphonic sensitivity of the thermometer. After the substrate disintegrated, the microphonic conditions were as bad as could be anticipated. We had a thin perforated membrane as the sample without active vibration isolation for the dewar. Despite this, we were able to obtain a great amount of data without taking any extraordinary measures to avoid vibrations. In preparing a screen for the thermal boundary measurements it would now seem reasonable to sputter to a thickness of 20 microns or more, ultrasonically remove the screen from the substrate, and simply clamp it into the Vespel[45] holder in much the same way as we did here. This eliminates the

troublesome step of thinning the substrate and the problem of heat flow through a substrate that is roughly as thick as a correlation length.

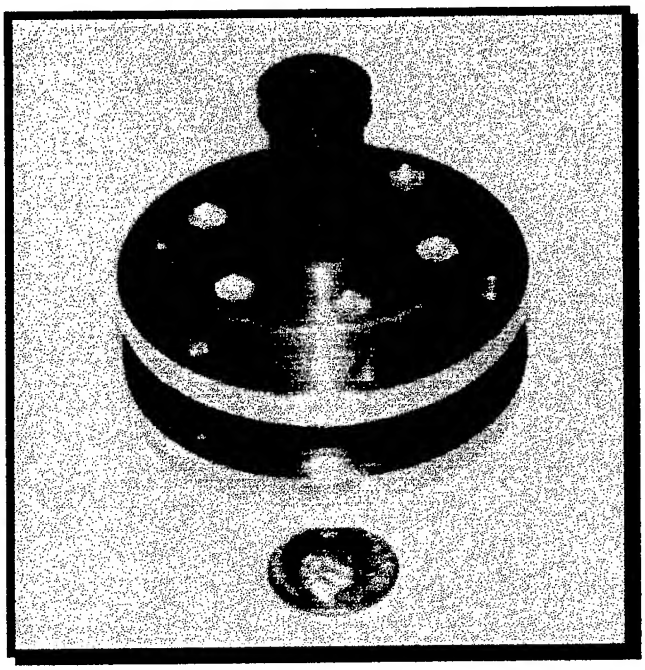

Figure 44: The Vespel[45] thermometer holder manufactured for use in the thermal boundary measurement apparatus. The screen was designed to rest on the recessed shelf inside the annulus and the SQUID pickup coil was wound around the groove machined into the outside diameter.

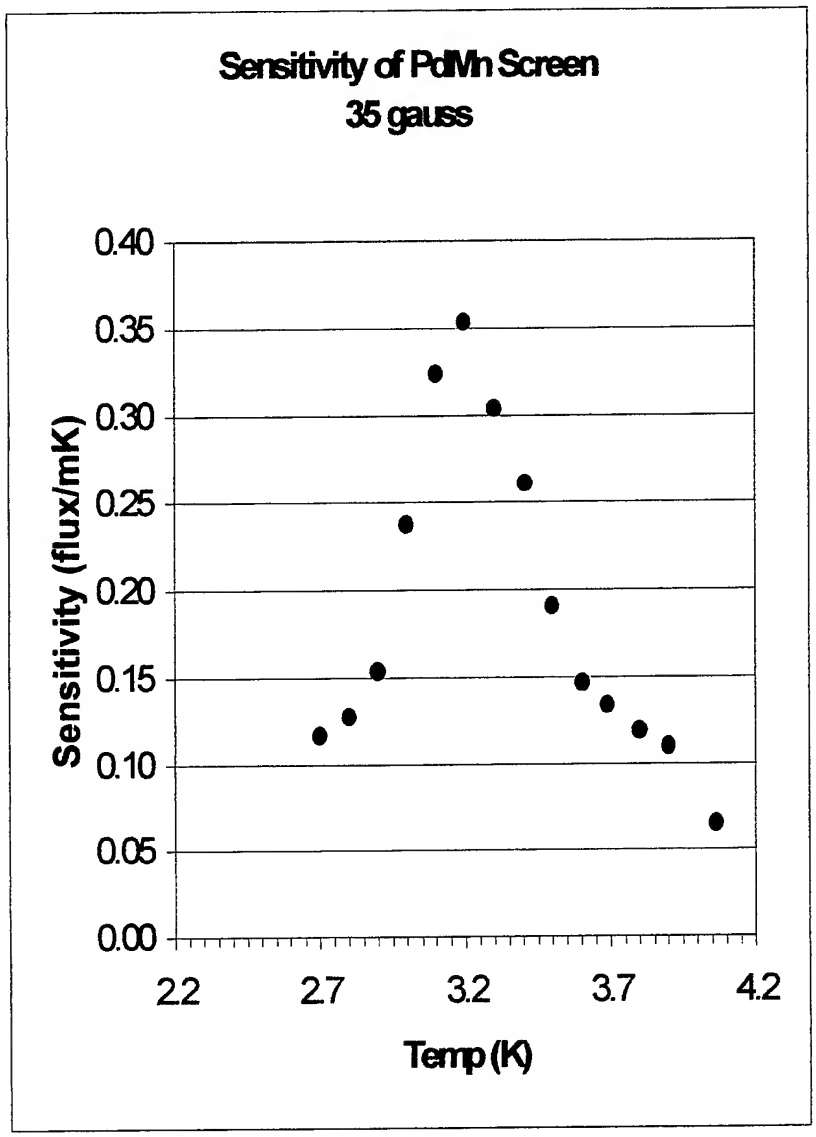

Figure 45: Data collected for the 10 μm thick PdMn screen at a magnetic field of 35 gauss. This data shows the very sharp transition associated only with low fields for the 12.5 μm thick film sample oriented with the surface parallel to the field. The peak is 0.4 K higher, however. The sensitivity is 1% of that of the 12.5 μm thick sample with the same field oriented parallel to the sample surface.

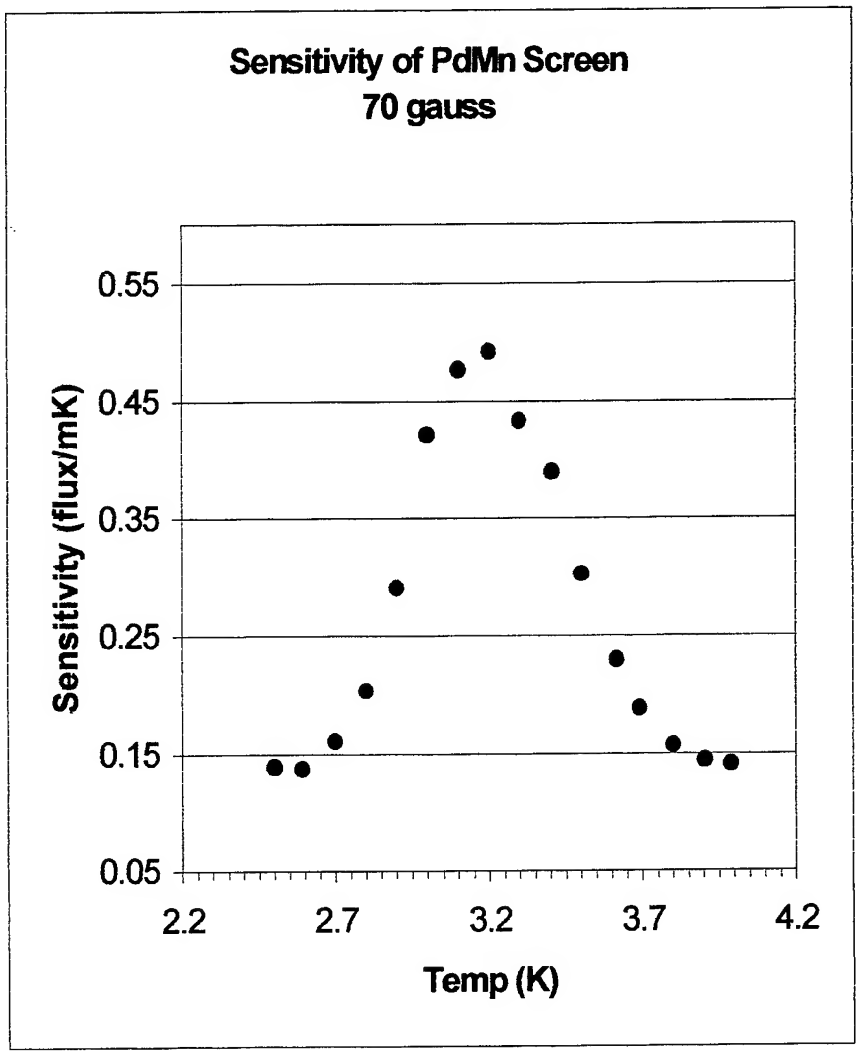

Figure 46: Data collected for the 10 μm thick PdMn screen at a magnetic field of 70 gauss. The shape is virtually identical to that for the data collected at 35 gauss, but the sensitivity is nearly 50% higher.

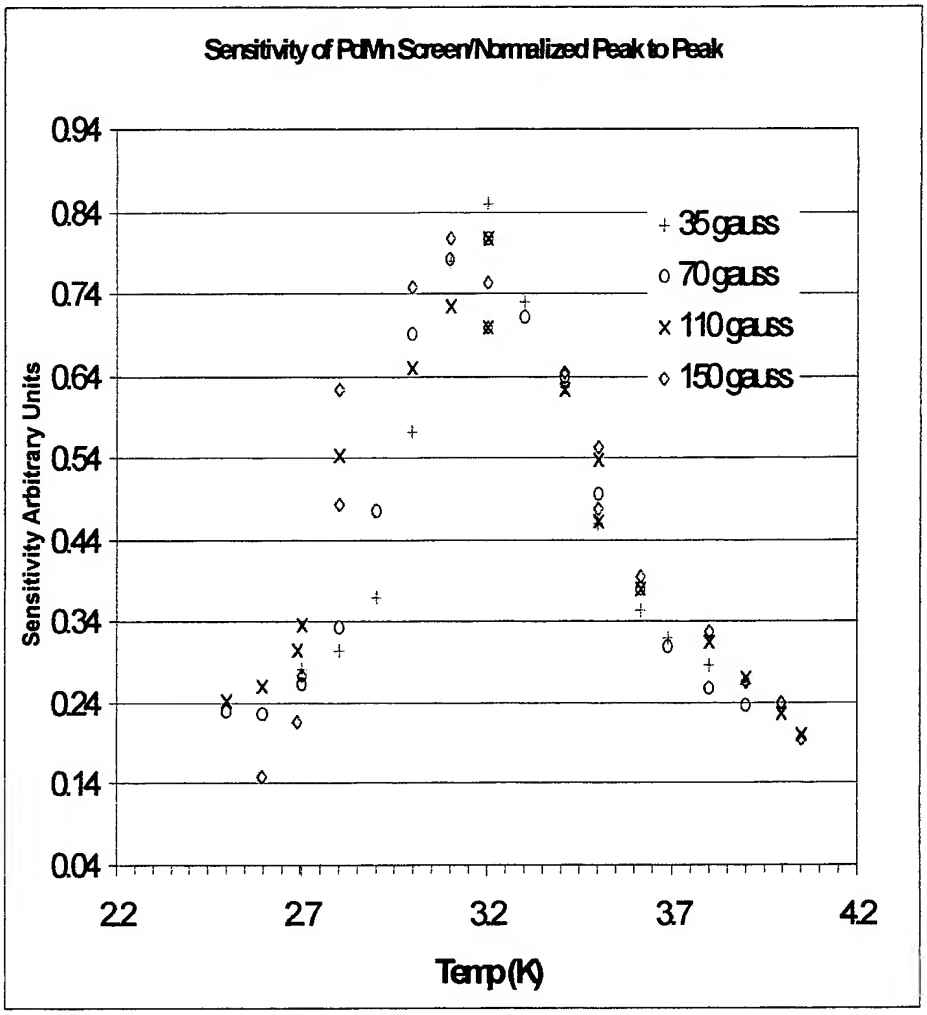

Figure 47: Data for four values of the magnetic field. The data is normalized so that the peak values coincide on the graph. This graph demonstrates the consistent shape of the data as it scales with magnetic field.

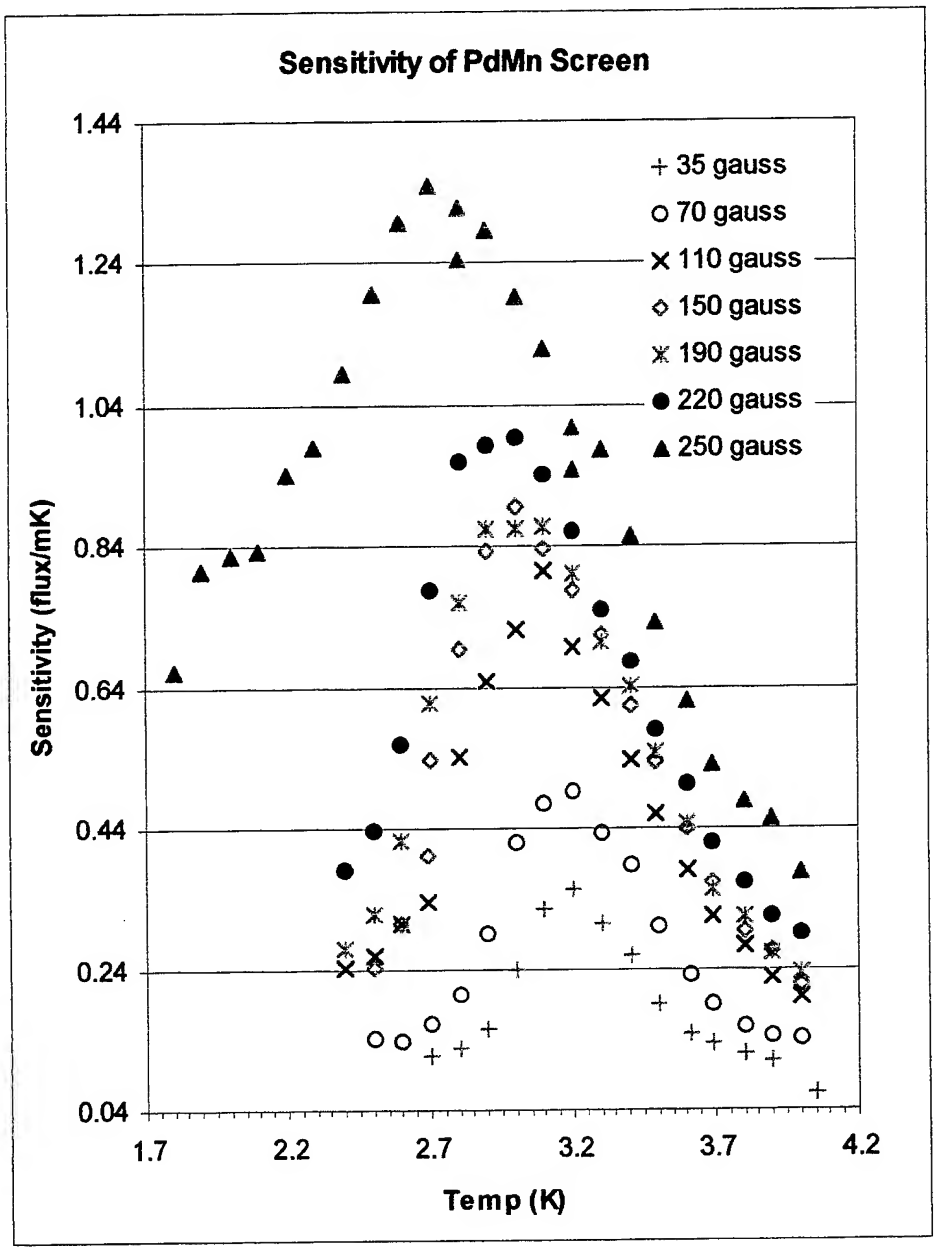

Figure 48: Data taken over a range of field values using the PdMn screen. The essential features are the consistent shape and the shift of the peak sensitivity toward lower temperatures with increasing field

Chapter Seven –Intentions for Further Study

As this dissertation is being written, the essential groundwork for the proposed boundary layer measurements has been completed. In order to complete those measurements several tasks must be accomplished. First, the sputtering process must be refined and a screen thermometer manufactured that will allow data to be taken in the thermometer's paramagnetic regime below T_λ. Second, two PdMn HRTs must be manufactured for the measurement of the bulk He temperature and the lower endplate temperature during the boundary layer measurements. Third, the entire system of actuation and data collection must be tested and refined in preparation for the experiment.

It became clear as the thermometry development process became more and more complex, with each set of measurements seeming to suggest new requirements for data that the ultimate objective would require far more money and time. Because of this, it became possible to devote some time to exploration of other applications of thin film thermometry. In particular, two applications and one technical development are being explored at this time. The technical development involves the use of thin film thermometry in a horizontal configuration with the magnetic field applied parallel to the film surface using a set of small superconducting Helmholtz coils mounted on the sample stage rather than using a conventional superconducting magnet oriented along the vertical axis of the cryostat. To make such a set of coils, aluminum spools were manufactured

with a 1 inch outside diameter, and 200 turns of superconducting wire were wound around each spool. The center bore of each coil was machined to fit a ¾" outside diameter niobium ring, machined from tubular stock. Sample holders were manufactured out of both aluminum and Vespel[45] for holding one of the original rectangular Pyrex[64] samples along the center line of the coils. The parts built for this purpose are displayed in Figure 49.

When the cryostat was reassembled with these parts installed one of the first measurements undertaken was to fill a gap in the previously collected data. All of our focus for two years was on developing the films to measure temperature changes with an applied field, but other researchers interested in our work have suggested that the films could be useful in measuring low level biomagnetic fields for diagnostic purposes. To begin exploring this possibility a temperature scan was performed with the ambient field alone. To do this the Helmholtz coils were left uncharged and data was taken with an unshield, sample mounted between the coils, as depicted in Figure 49. The results of this experiment are presented in Figure 50. The paramagnetic side of the data present just the sort of very steep sensitivity that would be required for the proposed application.

Currently the cryostat is being reassembled for a new experiment in which the sample is held at a fixed field with the Helmholtz coils and driven through very precise temperature changes by using a surface mounted resistor connected to a Josephson Junction array[70,71,72] quantum voltage source. It is hoped that this scheme can provide preliminary data for further study of using a Josephson array in conjunction with a PdMn

cell to achieve stable long term temperature control to within a picoKelvin. These investigations are ongoing.

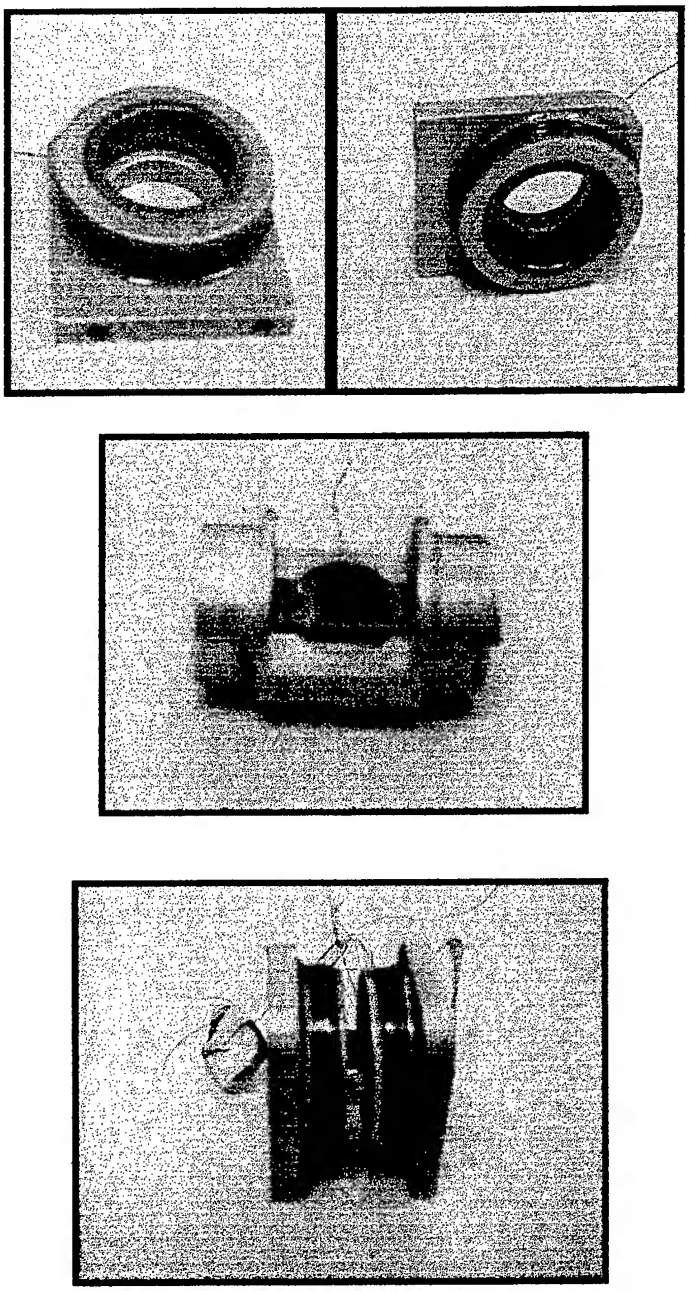

Figure 49: Superconducting Helmholtz coils and sample holder for testing the concept of applying a horizontal field to a sample in the cryostat.

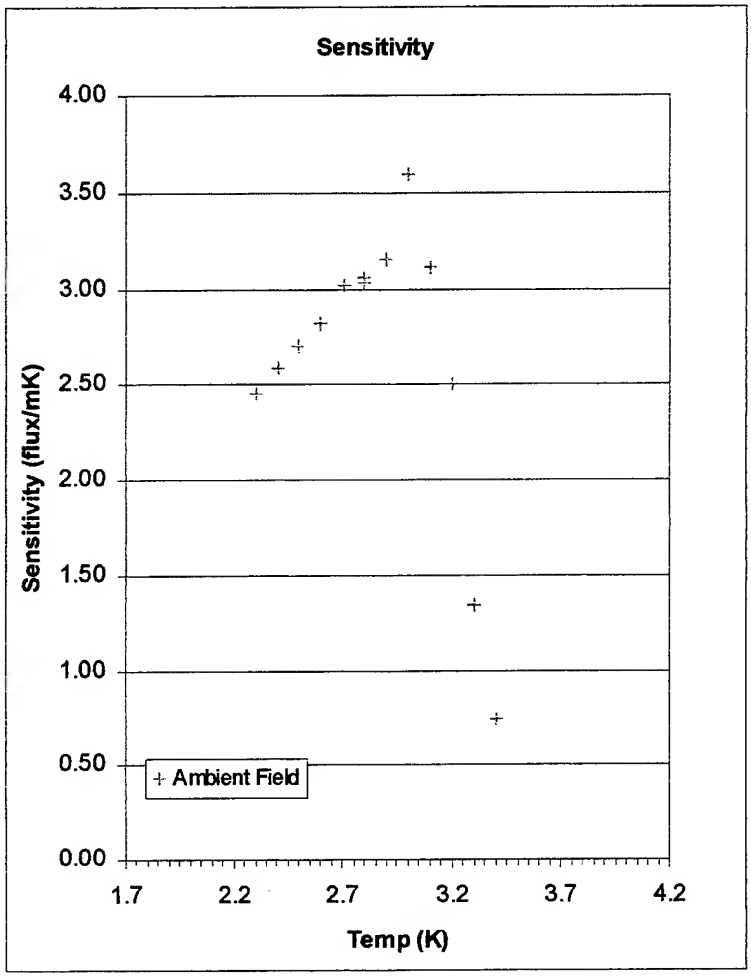

Figure 50: Data taken with an unshielded sample at ambient field conditions. Conditions were far from ideal, with poor thermal contact, and the sample and pickup coil mounted without epoxy to preserve it for further use.

Appendices

Appendix A: Tabular Data for Superconducting Joint I-V curve

Appendix B: Tabular Data for Figures in Chapter Four

Appendix C: Tabular Data for figures in Chapter Five

Appendix D: Tabular Data for Figures in Chapter Six

Appendix A: Tabular data for Superconducting Joint I-V curve

Current	*Ramp up*	*Ramp down*
0	0	
5	0	
10	0	
15	0	
20	0	
25	0.1	
30	0.3	
35	0.5	
40	0.7	
41	0.8	
42	0.8	
43	0.9	
44	5.6	
45	5.9	
46	6.1	
47	6.3	
48	6.5	
49	6.7	
50	7	
51	7.2	
52	7.5	
53	7.7	
54	7.8	
55	7.9	
56	8.2	
57	8.4	
58	8.6	
59	8.9	
60	9	
55		8
50		6.9
45		5.9
40		4.5
35		3.2
34		2.9
33		2.6

Table 1, continued

32		0.4
31		0.3
30		0.3
29		0.2
28		0.2
27		0.2
26		0.1
25		0.1
24		0.1
23		0.1
22		0
21		0

Table 1: Tabular data for the measurement of the superconducting joint I-V curve. The data is presented graphically in Figure 17 in the text.

Appendix B: Tabular Data for Figures in Chapter Four

Temp (K)	Permanent Magnet	Temp (K)	12.5 gauss
4	2.234553	3.99	0.6355
3.9	2.973312	3.89	0.6759
3.8	3.945465	3.79	0.6936
3.7	5.423607	3.69	1.9325
3.6	7.660672	3.59	2.506
3.5	11.04339	3.49	3.4403
3.37	17.60665	3.395	4.6764
3.3	22.14826	3.295	6.2385
3.2	27.57214	3.195	8.1815
3.1	30.21838	3.095	9.9033
3	33.22293	2.998	11.4435
2.9	35.70153	2.896	12.3477
2.8	36.59593	2.797	13.016
2.7	35.02783	2.698	12.7073
2.6	34.0465	2.593	12.5612
2.5	31.56795	2.515	11.8658
2.4	30.57255	2.398	11.0192
2.3	28.7546	2.298	10.2145
		2.294	10.3196
		2.27	9.5506
2.2	26.79428	2.198	9.69
2.1	24.66485	2.096	9.3056
2	22.98724	2.058	9.4159
1.9	21.18296	1.998	9.1632
		1.995	8.9055
		1.994	8.547
1.87	20.71486	1.899	8.169
		1.798	7.6413
		1.698	7.4685

Table 2: Tabular data for the measurements with the permanent magnet and the 12.5 gauss measurements with the electromagnet. This data is presented graphically in Figure 26. The cell entries to the right of the first and third rows are magnetic sensitivity in Flux Quanta per millikelvin.

Temp (K)	12.5 G	35 G	6 Gauss	70 Gauss
4	2.234553	4.57956	1.359424	7.22194
3.9	2.973312	5.825833	1.80257	8.947811
3.8	3.945465	7.534105	2.4468	11.08197
3.7	5.423607	9.870291	3.346242	13.8229
3.6	7.660672	12.87539		17.04717
3.5	11.04339	16.62712	7.279536	20.4737
3.4		21.14613	11.10364	23.82207
3.37	17.60665			
3.3	22.14826	25.92294	17.35665	26.93987
3.2	27.57214	30.34877	24.62076	29.49442
3.1	30.21838	32.46167	31.34003	31.428
3	33.22293	34.04975	34.50074	32.89722
2.9	35.70153	34.60519	34.69134	33.25544
2.8	36.59593	34.75337	33.19626	33.29565
2.7	35.02783	34.78954	31.59536	33.13472
2.6	34.0465	33.68319	30.2158	32.06207
2.5	31.56795	32.34095	27.66771	31.22574
2.4	30.57255	31.00567	26.14327	30.37419
2.3	28.7546	29.4862	23.877	29.3346
2.2	26.79428	28.21698	22.33462	28.49272
2.1	24.66485	26.3835	20.18225	26.8345
2.1				
2	22.98724	23.98788	19.35864	26.6532
1.9	21.18296	23.40492	17.731	25.69409
1.87	20.71486			
1.83			16.60991	
1.8		22.60764		
1.718		22.19967		

Table 3: Data presented graphically in the text as Figure 27. The cell entries to the right of the first row are magnetic sensitivity in Flux Quanta per millikelvin.

Temp (K)	35 G	70 Gauss	150 Gauss	250 Gauss
4	4.57956	7.22194	10.95186	13.39882
3.9	5.825833	8.947811	12.96178	15.21964
3.8	7.534105	11.08197	14.82353	16.88292
3.7	9.870291	13.8229	16.94456	18.46048
3.6	12.87539	17.04717	19.61728	20.33741
3.5	16.62712	20.4737	21.57666	21.76967
3.4	21.14613	23.82207	23.83745	23.46835
3.3	25.92294	26.93987	25.6127	24.47512
3.2	30.34877	29.49442	27.35855	26.01878
3.1	32.46167	31.428	28.78884	26.6995
3	34.04975	32.89722	29.51479	27.0594
2.9	34.60519	33.25544	29.838	27.68415
2.8				27.99485
2.8	34.75337	33.29565	30.01578	27.13347
2.7	34.78954	33.13472	29.5942	27.51606
2.6	33.68319	32.06207	29.09003	27.19872
2.5	32.34095	31.22574	28.94223	26.97734
2.4	31.00567	30.37419	28.2903	26.08012
2.3	29.4862	29.3346	27.288	24.7866
2.3				25.9236
2.2	28.21698	28.49272	26.77397	25.00006
2.2				24.81624
2.1	26.3835	26.8345	25.36875	24.354
2.1				24.1285
2	23.98788	26.6532	25.53096	23.8476
2			25.2504	
1.92			24.8054	
1.9	23.40492	25.69409		
1.8	22.60764			
1.718	22.19967			

Table 4: Data presented graphically in the text as Figure 28. The cell entries to the right of the first row are magnetic sensitivity in Flux Quanta per millikelvin.

Temp (K)	Decreasing T	Increasing T
1.71	13.54905	
1.87	15.52848	
1.9	16.84445	
2	18.51696	
2.1	19.6185	
2.2	21.59932	
2.3	23.6496	
2.4	25.76438	
2.5	27.45529	
2.6	29.58537	
2.7	30.90265	
2.8	30.04891	
2.9		34.26057
3		33.59876
3.1		30.83419
3.2		24.34892
3.3		16.85681
3.4		10.65765
3.5		6.962435
3.6		4.656
3.7		3.200265
3.8		2.36524
3.9		1.746821
4		1.308446

Table 5: Data presented in the text as Figure 29. The cell entries to the right of the first row are magnetic sensitivity in Flux Quanta per millikelvin.

Temp (K)	Decreasing T	Increasing T
1.83	16.60991	16.60991
1.9	17.731	18.26293
2	19.35864	19.35864
2.1	20.18225	20.9715
2.2	22.33462	22.33462
2.3	23.877	24.4076
2.4	26.14327	26.26957
2.5	27.66771	28.09255
2.6	30.2158	29.81052
2.7	31.59536	31.59536
2.8	33.19626	33.39504
2.9	34.69134	34.31801
3	34.50074	
3.1	31.34003	31.31803
3.2	24.62076	24.87318
3.3	17.35665	17.09811
3.4	11.10364	11.02674
3.5	7.279536	7.210601
3.6		4.705664
3.7	3.346242	3.357471
3.8	2.4468	2.395825
3.9	1.80257	1.765404
4	1.359424	1.36792

Table 6: Data from 6 gauss hysteresis test presented graphically in the text as Figure 31. The cell entries to the right of the first row are magnetic sensitivity in Flux Quanta per millikelvin.

Temp (K)	Decreasing T	Increasing T
4	4.57956	
3.9	5.825833	
3.8	7.534105	7.452545
3.7	9.870291	9.791688
3.6	12.87539	12.8009
3.5	16.62712	16.72363
3.4	21.14613	21.51522
3.3	25.92294	26.11254
3.2	30.34877	29.63034
3.1	32.46167	32.39569
3	34.04975	34.14997
2.9	34.60519	34.72006
2.8	34.75337	35.08467
2.7	34.78954	34.71257
2.6	33.68319	33.05275
2.5	32.34095	32.34095
2.4	31.00567	31.06882
2.3	29.4862	29.4104
2.2	28.21698	27.75742
2.1	26.3835	26.3835
2	23.98788	25.39068
1.9	23.40492	23.75954
1.8	22.60764	22.60764
1.718	22.19967	22.19967

Table 7: Data from 35 gauss hysteresis test presented graphically in the text as Figure 32. The cell entries to the right of the first row are magnetic sensitivity in Flux Quanta per millikelvin.

Appendix C: Tabular Data for Figures in Chapter Five

Temp (K)	Decreasing T	Increasing T
1.6	0.86601	0.84914
1.7	0.784671	0.754491
1.8	0.776794	0.86818
1.9	0.973572	1.043657
2	0.951152	1.07704
2.1	0.781275	1.045184
2.2	1.044991	0.988392
2.3	1.058596	1.028353
2.4	1.077613	1.072065
2.5	1.038858	1.080405
2.6	1.029403	1.04832
2.7	1.003644	1.010334
2.8	0.979078	0.980161
2.9	0.935409	0.935409
3	0.882958	0.888495
3.1	0.819296	0.830308
3.2	0.762823	0.766705
3.3	0.699296	0.694116
3.4	0.621557	0.62697
3.5	0.541312	0.544067
3.6	0.434087	0.435678
3.7	0.319999	0.311778
3.8	0.195634	0.18244
3.9	0.105967	0.099403

Table 8: Data from the 6 gauss test of a 1 μm thick sample with the field parallel to the sample surface depicted in the text in Figure 42. The cell entries to the right of the first row are magnetic sensitivity in Flux Quanta per millikelvin.

Temp (K)	35 gauss	70 gauss
2	0.643427	
2.1	0.686194	0.483709
2.2	0.696512	0.513881
2.3	0.725717	0.536859
2.4	0.768826	0.611705
2.5	0.789747	0.658671
2.6	0.863085	0.723086
2.7	0.957126	0.775998
2.8	0.953464	0.791243
2.9	0.976061	0.832523
3	0.986223	0.866074
3.1	1.016349	0.845725
3.2	0.994441	0.866252
3.3	0.966838	
3.4	0.914982	0.855377
3.5	0.852823	0.7963
3.6	0.752196	0.748473
3.7	0.633685	0.674205
3.8	0.495239	0.575858
3.9	0.363852	0.486699
4	0.253465	0.316362

Table 9: Data from the 35 and 70 gauss tests of a 1 μm thick sample with the field parallel to the sample surface depicted in the text in Figure 43. The cell entries to the right of the first row are magnetic sensitivity in Flux Quanta per millikelvin.

Appendix D: Tabular Data for Figures in Chapter Six

Temperature (K)	Sensitivity
2.701	0.0586
2.8	0.0636
2.898	0.1539
2.998	0.2500
3.099	0.3258
3.198	0.3360
3.3	0.2965
3.406	0.2558
3.5	0.1945
3.603	0.1546
3.69	0.1337
3.8	0.1067
3.902	0.0891
4.064	0.0526

Table 10: Data from the 35 gauss test of a 10 μm thick PdMn screen with the field perpendicular to the sample surface depicted in the text in Figure 45. The cell entries to the right of the first row are magnetic sensitivity in Flux Quanta per millikelvin.

Temperature (K)	Sensitivity
2.5	0.0697
2.593	0.0688
2.701	0.0803
2.8	0.2030
2.9	0.2908
2.998	0.4210
3.099	0.4767
3.198	0.4920
3.3	0.4334
3.406	0.3896
3.5	0.3024
3.616	0.2308
3.69	0.1882
3.8	0.1568
3.902	0.1447
3.990	0.1407

Table 11: Data from the 70 gauss test of a 10 μm thick PdMn screen with the field perpendicular to the sample surface depicted in the text in Figure 46. The cell entries to the right of the first row are magnetic sensitivity in Flux Quanta per millikelvin.

Temperature (K)	35 gauss	70 gauss	110 gauss	150 gauss	190 gauss	220 gauss	250 gauss
4.064	0.0658						
4.052	0.0655						
3.998		0.1415	0.202175	0.219656	0.236104	0.292418	0.380207
3.870							
3.902	0.1112	0.1456	0.2280288	0.268492	0.266252	0.316132	0.457851
3.8	0.1205	0.1578	0.2736645	0.296488	0.318526	0.36466	0.481894
3.701	0.1346	0.1895	0.3181784	0.366432	0.35466	0.422109	0.531484
3.616		0.2323					
3.604	0.1483		0.3821478	0.441822	0.449244	0.507878	0.625182
3.5	0.1923	0.3044					
3.497			0.4654054	0.536603	0.55352	0.583631	0.736791
3.406	0.2625	0.3919	0.5386129		0.645308	0.682498	0.858779
3.401			0.541808	0.619352			
3.299	0.3053	0.4356	0.6268285	0.720747	0.708364	0.754541	0.980938
3.2			0.7026741	0.779804	0.806271	0.866863	0.951879
3.198	0.3549	0.4940	0.6999091				1.010418
3.101	0.3253	0.4779	0.8090044	0.839268	0.869803	0.944258	1.120918
2.999	0.2379	0.4212	0.7237983	0.897912	0.865382	0.995652	1.193945
2.898	0.1539	0.2908	0.6476024	0.831651	0.864761	0.98079	1.285426
2.8		0.2903				0.956653	1.238648
2.8	0.1267	0.2030	0.5400164	0.691142	0.756597		1.312646
2.701	0.1159	0.1594		0.533913	0.61365	0.77365	1.349913
2.688			0.3336994				
2.599		0.1363	0.3004017	0.3978	0.4189	0.5533	1.284992
2.5		0.1378	0.2573407	0.3001	0.3162	0.4326	1.182102
2.399			0.2384168	0.2384	0.2658	0.3770	1.070235
2.298							0.965789
2.198							0.931565
2.099							0.8273
2							0.8261
1.9							0.813939
1.8						0.6766	

Table 12: Data for the PdMn Screen sensitivity data presented in the text as Figure 48. The numbers in the body of the table are in units of flux quanta per millikelvin.

References

[1]K. Onnes, Leiden Comm, **108**, 1908.

[2]F. London, Superfluids, II, Wiley, 1954, as cited in Z.M. Galasiewicz, Helium 4, Pergamon, 1971.

[3]S. W. Van Sciver, Helium Cryogenics, Plenum, 1986, pp 53, 77-8.

[4]E.L. Andronikashvili, Zh. Esksp. Theor. Fiz. **16**, 780 (1946)

[5] E.L. Andronikashvili, Zh. Esksp. Theor. Fiz. **18**, 242 (1948)

[6]J. Kerrisk and W.E. Keller, Bull. Am. Phys. Soc. **12**, 550 (1967)

[7]G. Ahlers, Phys. Rev. Lett. **21**, 1159, (1968)

[8]G.Ahlers and R. Duncan, Phys. Rev. Lett. **61**, 846, (1988)

[9]R. Duncan, G. Ahlers, and V. Steinberg, Phys. Rev. Lett,. **60**, 1522 (1988)

[10]R. Duncan and G. Ahlers, Phys. Rev. B **43**, 7707 (1991)

[11]Murphy and Meyer, Czech. Journ. Phys, **46**, 77 (1999 Supplement S1)

[12]W. A. Mouer, et al, Phys. Rev. Lett. **78**, 2421 (1997)

[13]A. W. Harter, et al, Phys. Rev. Lett. **84**, 2195 (2000)

[14]R. Haussmann and V. Dohm, Phys. Rev. Lett. **67**, 2404 (1991)

[15]R. Haussmann and V. Dohm, J. Low Temp. Phys. 89, 429 (1992)

[16]R. Haussmann and V. Dohm, Phys. Rev. B **46**, 6361 (1992)

[17]R. Haussmann and V. Dohm, Z. Phys B **87**, 229 (1992)

[18]See, for example, I.M. Khalatnikov, Introduction to the Theory of Superfluidity, Chap III, W. A. Benjamin, New York, 1965. As cited in Van Sciver, Chap 5.3.

[19]Van Sciver, pp. 173-177.

[20]Frank and Dohm, Phys. Rev. Lett. **62**, 1864 (1989)

[21]Richard Ferrell, unpublished communication.

[22]R.A. Ferrell, N. Menyhard, H. Schmidt, F. Schwabl, and P. Szepfalusy, Phys. Rev. Lett. **18**, 891 (1967)

[23]See, for example, Van Sciver, p. 101.

[24]L. Landau, J. Phys. (U.S.S.R., **5**, 71 (1941), as reprinted in Galasiewicz.

[25]W.M. Saslow, Phys. Lett. **35A**, 241 (1971)

[26] V.L. Ginzburg and A.A.Sobaynin, Sov. Phys. Usp. **19**, 775 (1976)

[27]A. Singsaas and Guenter Ahlers, Phys. Rev. B, **30**, 5103 1(984)

[28]R. Duncan, G. Ahlers, and V. Steinberg, Phys. Rev. Lett. **58**, 377 (1987)

[29]Duncan and Ahlers, Proc LT 18, Jap. Journ. Appl. Phys. **26**, Supplement 26-3, 363 (1987)

[30]Frank, Grabinski, Dohm, and Liu, Phys. Rev. Lett. **60**, 2336 (1988)

[31]R.V. Duncan, unpublished dissertation, University of California, Santa Barbara, 1988.

[32]Unpublished communication cited in Duncan's dissertation.

[33]R. Hausmann, J. Low Temp. Phys. **116**, 1 (1999)

[34]P. B. Weichman, A. Prasad, R. Mukhopadhyay, and J. Miller, Phys. Rev. Lett. **80**, 4923 (1988)

[35]R. Haussmann and V. Dohm, Phys. Rev. B, **46**, 3661 (1992)

[36]D.L. Goodstein, T.C.P. Chui, and A.W. Harter, Phys. Rev. Lett. **77**, 979 (1996)

[37]A. Onuki, J. Low Temp. Phys. **55**, 1984, p. 309.

[38]R.V. Duncan, Bull. Am. Phys. Soc, **44**, (1999) This is the schedule of the 1999 APS March Meeting and the abstract is available online at www.aps.org/meet/CENT99/BAPS/pdf/EC06.pdf

[39]B. J. Klemme, et al, J. Low Temp. Phys. **116**, 133 (1999)

[40]The division of RMC, Inc. that built this cryostat was subsequently purchased by Janis Research Company, Inc., 2 Jewel Drive, P.O. Box 696, Wilmington, MA 01887-0696, Telephone: (978) 657-8750

[41]E.T. Swartz, Rev. Sci. Instrum., **57**, 2848 (1986)

[42]E.T. Swartz, Rev. Sci. Instrum., **58**, 881 (1987)

[43] Precision Cryogenic Systems, Inc., 7804 Rockville Road, Indianapolis, Indiana 46214 Telephone: (317) 273-2800.

[44]Teflon is Dupont's tradename for its fluoropolymer resin.

[45]Vespel polyimide is a trademark of Dupont.

[46]Tra-Bond 2151 is a thermally conductive, electrically insulating epoxy, a product of TRA-CON, Inc., 45 Wiggins Avenue, Bedford, MA 01730. Tra-Bond 2115 is a low viscosity non silica based epoxy made by the same company.

[47]TS Products, Inc. 5550-2 McGuire Rd, Post Falls, Idaho, 83854, Telephone: (208) 222-2771.

[48]The GRT used was a Lake Shore Model GR-200A-1500, Lake Shore Cryotronics, Inc., 64 East Walnut St., Westerville, OH 43081.

[49]Quantum Design, Inc., 11578 Sorrento Valley Road San Diego, CA 92121.

[50]Linear Research, Inc., 5231 Cushman Place, Suite 21, San Diego, CA, 92110.

[51]TEAM Specialty Products Corp 1400 Eubank Blvd. SE, Albuquerque, New Mexico 87123, Telephone: (505)291-0182

[52]Y.S. Touloukian, Series editor, Thermophysical Properties of Matter (Plenum Press, NY, 1970-1979), Vol **2**, p. 183.

[53]Sonic Mill, Inc., 7500 Bluewater Road NW, Albuquerque, NM, both produces the sonic mill processing equipment and has an in house fabrication shop that milled the fused silica hole arrays.

[54]Valley Design Corp., 63 Bedford Rd, Westford, Massachusetts, 01886.

[55]John A. Thornton, "Coating Deposition by Sputtering," In Deposition Technologies for Films and Coatings, 1992, Noyes Publications, Park Ridge, New Jersey, pp 170-237.

[56]K. Wasa and S. Hayakawa, Handbook of Sputter Deposition Technology, Noyes, 1992, pp 30-31.

[57]W.L. Patterson and G.A. Shirn, Jour. Vac. Sci. Tech. **4,** 343 (1967)

[58]R. Wilson and L. Terry, Jour. Vac. Sci. Tech. **13,** 157 (1976)

[59]Peter Sigmund, Physical Review, **184,** 383 (1969)

[60]N. Laegreid, G. K. Wehner, Jour. Appl. Phys. **32,** 365 (1961)

[61]D. Rosenberg and G. K. Wehner, Jour. Appl. Phys. **33,** 1842 (1962)

[62]G.K. Wehner, R.V. Stuart, and D. Rosenberg, General Mills Annual Report of Sputtering Yields Report No. 2243, 1961 (unpublished) referred to in R. Behrisch, Ergeb. Exactk. Naturw. **35**, 295 (1964), as cited in Ref 54

[63]Target Materials, Inc., 1145 Chesapeake Avenue, Columbus, Ohio 43212.

[64]Pyrex is a trade name for Corning's brand of borosilicate glass.

[65]Macor is a trade name for a brand of machinable glass ceramic, produced by Corning.

[66]H. Eugene Stanley, Introduction to Phase Transitions and Critical Phenomena, 1971, New York, Oxford University Press.

[67]J.J. Binney, N.J. Dowrick, A.J. Fisher, and M.E.J. Newman, The Theory of Critical Phenomena, 1992, New York, Oxford University Press

[68]Microsoft EXCEL 97, on-line documentation. Excel is a product of Microsoft Corporation, Redmond, WA.

[69]See for example, J.D. Jackson, Classical Electrodynamics, John Wiley, 1975, pp. 187-191.

[69]G.M. Zassenhaus and J.D. Reppy, Phys. Rev. Lett., **83**, 4800 (1999)

[70]F.L. Lloyd, et al, IEEE Elect. Dev. Lett., **EDL-8**, 449 (1987)

[71]R.L. Stein and B.F. Field, IEEE Inst. and Meas., **IM-38**, 296 (1989)

[72]R. Duncan, Bull. Am. Phys. Soc., **34**, 1535 (1989)